DOI:10.15774/PPKE.ITK.2023.002


PÁZMÁNY PÉTER CATHOLIC UNIVERSITY

FACULTY OF INFORMATION TECHNOLOGY AND BIONICS

DOCTORAL THESIS

# Modeling, control and navigation of aerospace systems

*Thesis Advisor:*

Dr. Gábor SZEDERKÉNYI, DSc

*Thesis Co. Advisor:*

Dr. György CSEREY, PhD

*Author:*

Nawar ALHEMEARY

*A thesis submitted in partial fulfillment of the requirements*

*for the degree of Doctor of Philosophy*

*in the*

Roska Tamás Doctoral School of Sciences and Technology

2022

DOI:10.15774/PPKE.ITK.2023.002

DOI:10.15774/PPKE.ITK.2023.002

## Acknowledgment

This work would not have been possible without the constant support, guidance, and assistance of my major advisors: Dr. Gábor Szederkényi and Dr. György Cserey. Their level of patience, knowledge, and ingenuity is something I will always keep aspiring to. I would also like to thank Dr. Péter Polcz and Dr. János Juhász for their continuous help. I would be amiss if I did not mention Dr. Tamás Zsedrovits and Dr. Sameir A. Aziez, both whom were always ready to help me with any question I had. My gratitude also goes to our university staff for all they have done, which I will never forget. I truly appreciate the time they spent helping me on many occasions.

Finally, I would like to thank my family. Nothing would have been possible without their unconditional love and support.

*Al hemeary Nawar*

DOI:10.15774/PPKE.ITK.2023.002

## Abstract

Recently, there has been a rising interest in small satellites such as CubeSats in the aerospace community due to their small size and cost-effective operation. To support maneuverability, a CubeSat can be equipped with a propulsion system, in our case, utilizing a propellant tank where the fuel must be maintained at a certain temperature range. Simultaneously, the energy production should be maximized so that the other components of the satellite are not overheated. Because of these difficulties, ensuring that operating conditions fulfill different goals and constraints for small satellites with low cost and energy consumption is challenging. To meet the technological requirements, a novel control-oriented lumped thermal model is derived in nonlinear ordinary differential equation form for the studied fuel-tanked satellite. The model is able to simulate the thermal behavior of the surface and fuel tank of the satellite in its orbit. Additionally, we present multi-criteria control designs using the derived nonlinear model of the CubeSat systems. First, a *PID* control scheme with anti-windup compensation is employed to evaluate the minimum heat flux required to keep the propellant tank at a given reference temperature. Then, a linearization-based controller is developed to control the temperature. Finally, the optimization of the solar panel area and constrained temperature control is solved as an integrated nonlinear *MPC* case using the *quasi-LPV* form of the state equations. Several simulation scenarios with different power limits and solar panel coverage cases are shown to illustrate the trade-offs in control design and to show the applicability of the approach.

The *INS* update rate is faster than the one in the *GNSS* receiver. However, the GNSS received data may suffer for a few seconds blocking, for different reasons, impairing the integration architectures for GNSS and INS. Thus, a novel GNSS data prediction procedure employing a KNN predictor algorithm is proposed to treat data synchronization between the INS sensors and GNSS receiver and overcome GNSS data blocking. The experimental work was conducted on a drone that hovered over a minor Hungarian model airfield. The GNSS data is calculated for four different scenarios. One scenario has no blocking, and the other three have incremental blocking periods of data. An ultra-tight architecture is used to perform the GNSS/INS integration to handle the INS sensors' inaccuracies and divergences throughout the operation. The results show that using the GNSS/INS integration system yields more precise Cartesian coordinate data than using a stand-alone INS or GNSS system without a predictor.

DOI:10.15774/PPKE.ITK.2023.002

# Contents

DOI:10.15774/PPKE.ITK.2023.002

DOI:10.15774/PPKE.ITK.2023.002

# Nomenclature

| **Acronyms** | |
|---|---|
| ADCS | Attitude Determination and Control System. |
| CubeSat | Cube-shaped miniaturized satellite. |
| Face | Face of the CubeSat. |
| COTS | Commercial Off-The-Shelf. |
| CDH | Command and Data Handling. |
| LPV | Linear Parameter Varying. |
| MPC | Model Predictive Control. |
| Solar panel | Solar panel forced to CubeSat surface. |
| Tank | Spherical propellant tank. |
| 1U | One unit CubeSat. |
| INS | Inertial Navigation System. |
| GNSS | Global Navigation Satellite System. |
| Galileo | Europian GNSS. |
| BeiDou | China GNSS. |
| KNN | K-Nearest Neighbo. |
| GNSS/INS | Integration between GNSS and INS. |
| I | In-Phase. |
| Q | Quadrature. |
| IMU | Inertial Measurement Unit . |
| AHRS | Attitude Heading Reference System. |
| AMSL | Above Mean Sea Level. |
| Geodetic | Geographic coordinate. |
| LLA | Geodetic coordinate. |
| ECEF | Earth-Centered Earth-Fixed coordinate. |

DOI:10.15774/PPKE.ITK.2023.002

| Symbols | Units | |
|---|---|---|
| $A$ | $[m^2]$ | Area of each face. |
| $AF$ | | Percentage of Albedo factor. |
| $A_P$ | $[m^2]$ | Area of the solar panel. |
| $a$ | | Material's absorptivity . |
| $a_s$ | | Material's solar absorptivity. |
| $a_{IR}$ | | Material's infrared absorptivity. |
| $a_{IR}^{Al}$ | | Aluminum infrared absorptivity. |
| $a_s^{Al}$ | | Aluminum solar absorptivity. |
| $a_s^{sc}$ | | Solar panel solar absorptivity. |
| $a_s^{Al\text{-}sc}$ | | Aluminum and solar panel average absorptivity. |
| $C_p$ | $[J/kg\ K]$ | Aluminum specific heat. |
| $C_p^s$ | $[J/kg\ K]$ | Stainless steel specific heat. |
| $C_p^{sc}$ | $[J/kg\ K]$ | Solar panel specific heat. |
| $C_v$ | $[J/kg\ K]$ | Nitrogen specific heat. |
| $\varepsilon$ | | Material's emissivity. |
| $\varepsilon_{IR}$ | | Aluminum IR emissivity. |
| $\varepsilon_{IR}^{Al}$ | | Aluminum infrared emissivity. |
| $\varepsilon_{IR}^{sc}$ | | Solar panel infrared emissivity. |
| $\varepsilon_{IR}^{Al\text{-}sc}$ | | Aluminum and solar panel average infrared emissivity. |
| $F_{ft}$ | | View factor between a face and the tank. |
| $G_s$ | $[W/m^2]$ | Solar constant. |
| $h$ | [m] | Distance of the tank's surface to the face. |
| $m$ | [kg] | Total mass of CubeSat. |
| $m_{Al}$ | [kg] | Mass of an Aluminum face. |
| $m_g$ | [kg] | Mass of nitrogen in the tank. |
| $m_s$ | [kg] | Mass of the tank (stainless steel). |
| $P$ | [sec] | Orbital period of the CubeSat. |
| $P_1$ | [sec] | First orbit interval (first quartile of the orbital period). |
| $P_2$ | [sec] | Second interval (second and third orbital quartile ). |
| $P_3$ | [sec] | Third interval (fourth quartile of the orbital period). |
| $\dot{Q}$ | [W] | Power dissipated heat rate. |
| $\dot{Q}_c$ | [W] | Heat flux applied to the tank generated by the heater. |
| $\dot{Q}_{F_i}$ | [W] | Radiated heat transfer between the $i$th face and the tank. |

DOI:10.15774/PPKE.ITK.2023.002

| | | |
|---|---|---|
| $r$ | [m] | Tank radius. |
| $T_{\mathrm{E}}$ | [K] | Earth's reference temperature. |
| $T_t$ | [K] | Tank's temperature. |
| $V_r$ | [K] | Tank reference temperature. |
| $\lambda$ | $[=\frac{\mathrm{A_P}}{\mathrm{A}}]$ | Portion of the solar panel area compared to that of the face. |
| $\sigma$ | $[\mathrm{W/m^2K^4}]$ | Stefan-Boltzmann constant. |
| $c$ | [m/sec] | Velocity of the light. |
| $C(t)$ | | Sequence of the code $C/A$. |
| $D(t)$ | | Navigation message. |
| $\omega_j$ | | Weight of the j-neighbor. |
| $w$ | [rad/sec] | Angular frequency. |
| $w'$ | [Hz] | Carrier frequency of the receiver. |
| $\hat{w}$ | [Hz] | Estimated carrier frequency of the receiver. |
| $w_e$ | [Hz] | Error in frequency. |
| $x_u$ | [m] | Measured position. |
| $v_u$ | [m/sec] | Measured velocity. |
| $x_e$ | [m] | Position error. |
| $v_e$ | [m/sec] | Velocity error. |
| $\hat{y}_l$ | | Predicted data. |
| $y_j$ | | Testing data. |
| $\psi'$ | | Phase of the GNSS signal. |
| $\hat{\psi}$ | | Estimated phase of the GNSS. |
| $\psi_e$ | | Error in phase. |
| $\xi$ | | Gaussian Noise. |
| $\xi_I$ | | In-phase Noise. |
| $\xi_Q$ | | Quadrature noise. |

DOI:10.15774/PPKE.ITK.2023.002

# Chapter 1

# Introduction

## 1.1 Background

### 1.1.1 Satellite systems

The successful launch of Sputnik 1 in October 1957 ushered in a period of rapid technological development between the Soviet Union and the United States of America. That spawned new political, military, and scientific headway to cultivate the next 60 years of space technology, so-called the *Space age* [1; 2]. Subsequently, over the last two decades, there has been a surge in interest in and use of much smaller satellites, taking advantage of shrinkage-mutation in a wide range of digital devices and systems. In addition, small satellites' increasing popularity in planning and creating new missions via shorter development time intervals and cheaper orbital delivery costs. A new age in space, termed *Space age 2*, has begun as a consequence of the expanding possibilities for space access via new technologies in space programs, global partnerships, new launch vehicles, and new launch service providers [3; 4].

Small satellites are indeed a novel technology because they can achieve the conventional satellite services incorporated by reducing development time and cost. These small satellites do not exceed the size of a small suitcase, yet they orbit Earth in formations. Advances in minimized research instruments, miniature satellite technologies, and increased access to space have led to a spurt in space studies and business. They have been developed to construct a wide range of applications, such as *in planetary science research, astrophysics, biomedicine, and Earth remote sensing*, by universities, governments, and private aerospace companies. CubeSat technology was produced at the beginning of this century to satisfy the low cost of designing and the lowest price of launching into space. These small satellites have provided an abundant opportunity for scientists and engineers to deal with space, so they have become substantial in space technology. When CubeSat manufacturing and launch are affordable, it is possible to place numerous satellites in orbit. However, each satellite must be positioned at a unique orbital point to arrange this constellation form. It can be done either by using the launcher's capabilities or by performing maneuvers after the launch using onboard propulsion; so far, CubeSats often have very limited or no propulsion systems [3; 5].

DOI:10.15774/PPKE.ITK.2023.002

There is a pragmatic temperature difference of hundreds of degrees in orbit when a satellite faces the Sun or is in the shadow part of the orbit. Objects may become too hot or cold in space, and cooling is only possible by transferring heat to the outside surface of a satellite and then radiating it into deep space. Therefore, thermal control is a critical component in keeping the temperature of a CubeSat within the survival temperature range. The majority of CubeSats practice passive temperature control. This is accomplished by installing thermal blankets comprised of many layers of insulation on the Cubesat, using paint (*black is used to absorb heat, whereas white is used to reflect it*), and using solar panels placed on the outside surface, which acts as an insulating layer as well.

The satellite's power system consists of batteries, solar panels for charging, and a charge regulator. The satellite travels from the full Sun to the Earth's shadow in each cycle of Earth's orbits. For planning operations, the available energy in the batteries must be considered to satisfy the onboard requirements. Because of CubeSat's small surface area constraints, power is precious. Furthermore, the satellite's active thermal management system consumes energy, so it is essential to ensure that CubeSat's active mean control system utilizes the lowest amount of power possible [2; 6].

Many literatures, reports, and books are published concerning illustrating and evaluating small spacecraft,e.g., the State of Art NASA's online SmallSat technology report integrated with CubeSat 101 equips CubeSat concepts and developments' comprehensive and regularly updated attributes [7; 8; 9].

### 1.1.2 Satellite navigation systems

Navigation systems have advanced certainly in territorial coverage and precision during the last 50 years. In particular, navigation and positioning technologies have significantly changed our industries and lifestyles, especially since the invention of the Global Navigation Satellite Systems (GNSS), which incorporated techniques of the Global Position System (GPS) in the United States, the Global Navigation Satellite System (GLO NASS) in Russia, the Galileo system in the European Union, and the (BeiDou) Navigation Satellite System (BDS) in China. Satellite navigation systems are fundamentally based on signals transmitted from the space segments, the ground segments' reception, and the processing of the transmitted signals. Therefore, the design and performance of this signal may limit the overall system performance. Concurrently, technological developments have made significant improvements in wireless communications, aerospace engineering, and satellite navigation. Also, theoretical research has proposed many novelties concerning the design of satellite navigation signals. The construction of a satellite navigation system depends on the specific mission and application conditions; the design constraints of the signal's various elements are mutually related. Thus, it is impossible to develop a new navigation signal with better-integrated performance simply by combining multiple methods or by mimicking different systems [10; 11].

DOI:10.15774/PPKE.ITK.2023.002

The navigation systems of aerospace devices are highly accurate and reliable in different weather conditions, and errors do not accumulate over time. On the other hand, they have a relatively low data update rate and some complications concerning the attitude data. Onboard Inertial Navigation Systems (INS) are the gyroscope and accelerometer that measure the integration of velocity, position, and attitude to the vehicles. The inertial components have a faster data update rate, but the INS navigation errors caused by device errors accumulate as time elapses via the integration principle in navigation computation. The INS exponential error must be rectified to secure the required navigation accuracy for the long-term airborne mission. Thus, to create robust integrated navigation systems, all other navigation syntheses are conducted to aid inertial navigation and make up the integrated navigation systems [10; 12].

The GNSS and INS navigation systems, of course, each have their own strengths and weaknesses, so each system alone is challenging to meet the requirements of high navigation performance for a long time. Therefore, the INS/GNSS integration has complementary advantages and effectively achieves accurate navigation. Therefore, combining INS and GNSS might provide complementing benefits, making it a viable option for attaining high-accuracy and reliable navigation units. In terms of the INS/GNSS integration mechanism, integrated solutions have progressed from the simple initial method to complex approaches. A simple integration model uses satellite tracking signals to reset the inertial navigation system's position and velocity directly. This integration procedure corrects the inertial navigation system's positioning and velocity defects while the attitude or inertial system errors will not be restored. Therefore, the in-depth integration technique has been developed to improve the complementarity of the inertial navigation system and the satellite navigation system. It is a technique of advanced integration in which the inertial navigation system and satellite navigation system may assist and correct one another to achieve superior performance [12; 13].

The theoretical and practical aspects of satellite navigation systems have gained much attention from academic researchers. Therefore, many scientists have published distinguished books and literature on the operating principles, applications of satellite navigation systems, and on the hybrid INS/GNSS navigation systems [14; 15; 16].

DOI:10.15774/PPKE.ITK.2023.002

## 1.2 Aim and motivation

The first research objective of this work was the model-based thermal analysis and control of a small satellite (CubeSat) to study the possibility and conditions of the fuel tank installation. Next, an optimization-based approach considering control inputs was exploited to investigate an optimal solar panel ratio to upgrade a CubeSat power system. Finally, GNSS data prediction and synchronization investigations were conducted between the INS sensors and the GNSS receiver in order to enhance the navigation data. The motivation behind the research is presented in this section.

### 1.2.1 CubeSat functionality

Interest in CubeSats has grown tremendously within the space community from space agencies, industry, and academia. Two factors have influenced this spurt of interest: the low-cost nature of access to space and the utilization of Commercial Off-The-Shelf (COTS) technologies in architectural design. These two factors have led to a significantly lower overall cost of a CubeSat mission. The CubeSat Project was started in 1999 as a collaborative effort of California Polytechnic State University and Stanford University to develop standards for small satellites. Initially, a CubeSat was defined as a ten-centimeter cube weighing one kilogram or one unit (1U). Then specifications have changed over time, and nowadays, it is possible to build even bigger CubeSats up to (12U). In addition, CubeSats are often launched as a secondary payload due to their compact size. Thus, standardizing their designs facilitates their assembly inside launchers and deployment in orbit.

All satellites, including CubeSats, comprise elementary survivability and mission progress subsystems (buses). Some of these buses are custom designed and built, while others can be underlying COTS parts. These buses include the Attitude Determination and Control System (ADCS), Command and Data Handling (CDH), communications, structure, power, propulsion, thermal control, and payload. The Attitude Determination and Control System (ADCS) determines the attitude and orientation of the satellite and can also alter it if needed through active means. The Command and Data Handling subsystem (CDH) serves as the CubeSat's "brains," including the electronics and software required to execute specific orders while in orbit. The communications subsystem includes antennas and radios required for communication between the satellite and the ground station or other satellites. A structure subsystem is a mechanical subsystem that holds all the components in place upon launch and provides structural support. Typically, the bus structure is intended to work with stacks of devices that use a PC/104 hole arrangement. Depending on the bus construction architecture, electronics stacks may be dropped into the bus from the top or slid in from the side. When feasible, sharp corners are avoided, and fillets are included in the structural design to mitigate stress concentrations. The payload is the part that fulfills the mission's overall purpose, for example, an optic for Earth imaging applications [17; 18].

DOI:10.15774/PPKE.ITK.2023.002

Propulsion subsystem engineering is becoming more critical as the number of CubeSats grows. Innovative propulsion systems are needed to provide rotational attitude control, orbit modification, and de-orbiting, depending on the mission requirements. Without a propulsion system, gravity influences the CubeSat and begins an early de-orbit process, shortening its space duration. Thus, the absence of a propulsion bus has restricted CubeSats in orbit to a few weeks, or at most months. Several propulsion methods are being developed for CubeSats, including butane systems, pulsed plasma, and arc thrusters. In addition, the development of new thruster technologies such as monopropellant systems, green monopropellant systems, cold gas systems, and ion propulsion systems is underway. The simplest method uses chemical propellants kept in tanks connected to a pressure reducer and a control valve. Most systems try to increase the total enthalpy of the working fluid before the nozzle, which results in higher kinetic energy and correspondingly higher propulsive forces by speeding the propellant flow out of a diverging nozzle [19; 20; 21].

The purpose of the thermal control system bus is to keep the temperature of the CubeSat components within specified limits, considering power consumption, operations, and other factors in the given orbit. In other words, a thermal control bus is essential to avoid CubeSat freezing or overheating by the extreme thermal conditions in space, securing optimal functionality for mission success. However, due to the crucial space environment *vacuum conditions*, heat transmission is mostly by radiation and conduction, with convection occurring exclusively in manned spacecraft systems. Also, thermal systems are often treated as subsystems of structural systems because of the strict correlation between them. Therefore, a thermal control bus system is constrained by the spatial arrangement of the CubeSat elements and the materials employed to construct them. So, the materials selection and component placement restrict and influence the temperature exchange between the satellite's internal components and its surroundings. When addressing the temperature management of thermal systems, two temperature limits are commonly defined: an operating limit and a survival limit. A thermal control system that is effective will maintain component temperatures within their operational limits [2].

Power generation and optimal photovoltaic panel orientations are essential for small satellites with restricted surface areas for panel mounting. A CubeSat power bus that includes solar panels and batteries is constrained by the small area for solar panels and lacks intricate and heavy deployable boards. Solar flux is the only energy source in a CubeSat that generates the power required for spacecraft operations. It can be a body-mounted or deployable configuration depending on the satellite design and mission. Body-mounted solar panels are fixed to the structure bus itself, while deployable solar panels have hinges that can rotate the panels outward and orient them toward the Sun. Because they orbit in low Earth orbit, small satellites frequently undergo the Earth's shadow and the satellite's direction prospective Sun. However, it encounters a significant variation in the thermal environment during Earth's Sunlit and eclipse periods while a satellite is orbiting Earth. Thus, a thermal analysis of the solar panels to ensure the safe operation of satellites throughout their mission life is of great importance. Also, the precise pointing of CubeSat solar panels toward the Sun is impossible because of the difficulty of carrying out attitude determination and control systems with low mass and low onboard power consumption. As a result, CubeSat has a low amount of electric energy; in particular, the growing community of CubeSat producers is confronted with operational limits and power constraints, necessitating the development of innovative panel configurations [3].

DOI:10.15774/PPKE.ITK.2023.002

### 1.2.2 Navigation systems and related challenges

Currently, three major global navigation satellite systems, including GPS, GLO NASS, and Galileo, have a notional constellation of 75 satellites. If all three systems supply spare satellites besides the BeiDou navigation satellite system, and if space-based augmentation systems (SBAS) satellites are included, then up to 90 satellites will send navigation signals concurrently to perform GNSS ranging measurements [22; 15]. Satellite navigation is used throughout all stages of flight. With local augmentation systems, GNSS may even deliver high-accuracy landing performance. The navigation systems must provide high integrity, continuity, and availability levels besides accuracy.

The Strap-down Inertial Navigation System (SINS) estimates the airborne location, velocity, and attitude, incorporating inertial components' measurement data and initial system parameters. The inertial elements are the core of SINS, and their accuracy directly affects the system's performance. However, even ideal inertial components produce results with errors because of several interferences, which significantly affect the accuracy of SINS. Inertial component errors may be deterministic or random. Determinate error is the primary cause of the inertial component error; hence, building an inertial component error model, testing it, and adjusting it within SINS is essential. Despite just a minor component of inertial component error, a random error has a significant impact on SINS accuracy. Random errors may be statistically regulated or not. In the case of statistically regulated random errors, optimal filtering is typically used for the estimate, and compensation [13].

Integration of the Global Navigation Satellite System and Inertial Navigation System (GNSS/INS) is necessary to precisely navigate from open skies to densely populated areas. GNSS, which includes augmented, assisted, differential, and relative system concepts, needs a direct line of sight between the satellite and the receiver for accurate localization . On the other hand, inertial systems are self-contained and independent, have no visibility issues, and are as accurate as GNSS when used in short time intervals. However, due to the double integration over time, the inaccuracy of an INS increases with time squared. Therefore, both techniques are usually integrated to achieve a high-performance navigation system.

Five levels of system integration are commonly distinguished, separately, loosely, closely, tightly, and deeply coupled (ultra-tightly coupled); the significant property of ultra-tightly coupled is that the INS inertial data is used to assist the GNSS tracking loops. Typically, the design of a deeply coupled system needs synchronization between the INS and the GNSS receivers; thus, an Extended Kalman Filter (EKF) is used to merge the satellite and inertial information. In engineering practice, mathematical models of systems are often nonlinear, for example, the guidance and control system of a drone, the inertial navigation system of an aircraft or cruise ship, and the attitude determination and positioning system of a satellite. Thus, research on nonlinear optimal state estimation has significant technical relevance. While its filter performance is comparable to that of the Kalman filter for linear systems, it clearly outperforms the extended kalman filter for nonlinear systems, as there is no need to calculate the Jacobian matrix or linearize the state or measurement equations; thus, there is no truncation error in higher-order terms. Even though its precision is limited because of the requirement for linearizing nonlinear systems and calculating the "Jacobian" matrix during the application, EKF is commonly used in the navigation fields of guided airborne systems. In addition, the discrete EKF equation can only be executed when the filter and single-step prediction errors are small [13; 23].

DOI:10.15774/PPKE.ITK.2023.002

The advantages of the ultra-tightly coupled approach include accurate GNSS signal prediction, reduced jamming of the GNSS by decreasing the tracking loop bandwidth of the GNSS receiver significantly, and improved satellite signal tracking during high-speed maneuvers. Thus, the ultra-tightly coupled strategy improves accuracy, availability, and continuity at the cost of extensive onboard processing of the airborne [15].

## 1.3 State of the art

At present, a few CubeSats have flown in space with an onboard propulsion system. These thrusters are used for attitude control or performing orbital maneuvers, formation flight, deorbit, drag recovery, and proximity operations. Because of the significant and growing interest in CubeSat mission capabilities, several propulsion systems have been rapidly developed for CubeSats, such as cold gas propulsion systems, solar sails, electric propulsion systems, and chemical propulsion systems [24; 25]. Cold gas propulsion systems are relatively simple solutions for CubeSats. Gas from a high-pressure gas cylinder is simply vented through a valve and nozzle to produce thrust [26; 19]. The investigation of the potential thermal hazards of installing the fuel tank must be considered as an early stage of featuring an engine in the CubeSat. Therefore, an internal thermal control subsystem must be developed to effectively regulate the heat transfer to ensure that the system remains within its thermal operational limits,[24; 27]. To achieve the intended performance of the component, the operational thermal limits must be strictly maintained. For simple tracking control, a PID controller might still be a practical choice, even for certain nonlinear processes[28].

The main task of the thermal modeling is to give a sufficient description of the CubeSat surface and propellant tank material properties and formulate appropriate initial and boundary conditions. The vast majority of control design techniques require models in ordinary differential equations form [29]. For nonlinear models, such as the CubeSat system studied, a low-dimensional model is preferred due to the computational complexity of the control design. This approach is also supported by control theory and practice; in general, such simple models are often sufficient for controller design [30]. As the first step to regulating temperature, a passive control in the form of the appropriate composition of materials covering the surfaces of the satellite is used. During the construction of the model, the standard principles of thermal modeling [31], and their application in aerospace engineering are followed [32; 33].

DOI:10.15774/PPKE.ITK.2023.002

Relevant results can be found in the literature concerning the thermal modeling and analysis of small satellites in the form of ODEs. For example, in [34] a simple thermal dynamical model of a CubeSat containing two differential equations is presented. The two lumped balance volumes are the surface and internal parts of the satellite, respectively. It is shown that the problem is mathematically analogous to the forced vibration of a damped mechanical system. In [30], new theoretical results on the qualitative behavior of spacecraft thermal models are provided that contain several nodes (compartments). It is proven that such models exhibit a unique asymptotically stable equilibrium in the positive orthant with constant external disturbance inputs, which leads to a stable limit cycle during orbital motion. The analysis concerning the frequency domain of a multi-compartmental model of a satellite is conducted in [35]. The ODEs are linearized around the equilibrium points, which permits frequency domain analysis. Feedback linearization aims to apply a suitable nonlinear feedback law to nonlinear systems to obtain a linear closed-loop system in the input-output sense. Therefore, it is a basic but often practically limited technique for controlling nonlinear systems. Many surveys discuss the effects of coordinate changes and feedback transformation for input-output-wise linearization in order to achieve full linearity of both state-space equations and the output map [30; 35].

The Linear Parameter Varying (LPV) paradigm has received a lot of attention in recent decades and has become a standard formalism in systems and control theory. An LPV framework treats linear dynamical systems that have state-space representations depending on time-varying parameters; thus, it can be considered as the natural extension of the Linear Time Invariant (LTI) framework [36; 37]. Furthermore, the LPV framework is a popular approach to rewriting nonlinear systems by involving nonlinearities in the scheduling parameters, and in this way, it is possible to extend some of the linear control techniques for nonlinear systems [38]. The combination of LPV control and feedback linearization has been implemented in [39] to provide a general control method for input-affine nonlinear systems. Nevertheless, instead of linearizing the nonlinear systems, set-valued methods with Quasi-Linear Parameter Varying (quasi-LPV) representations have been developed for nonlinear systems [40]. The LPV models can be employed to describe nonlinear models derived from nonlinear differential equations concerned with physical relations. Often, a nonlinear state-space model can be embedded into the so-called quasi-LPV model class [41; 42; 43], in which the time-varying parameters are typically disturbance signals or functions of the state, input, and/or output. In [44], three different quasi-LPV model formulation techniques are discussed, namely, state transformation, function substitution, and an LPV extension for the well-known Jacobian (linear approximation) method.

Due to the rapid growth of computational power in the last few decades, a new control methodology has emerged in the systems and control community based on prediction and optimization. These concepts are collectively called the *Model Predictive Control* (MPC) framework, which spans a reasonably comprehensive class of system models. Many results are available for general nonlinear systems, for example, in [45; 46]. Other MPC techniques are formulated specifically for nonlinear models in a quasi-LPV form; see e.g. [47; 48; 49 ; 50]. Several useful numerical techniques of [46; 51; 45; 52; 53; 54] were implemented in Matlab's Model Predictive Control Toolbox [55].

DOI:10.15774/PPKE.ITK.2023.002

The GNSS/INS integration is a prominent navigation mechanism in which the short-term accuracy of the INS is processed in real-time using the GNSS long-term accuracy signals [56]. Because the Inertial Measurement Unit (IMU) inherent shifts, the INS navigation error exponentially increases in time, resulting in reduced navigation accuracy [57]. INS continuously calculates position, velocity, and attitude angles during GNSS signal loss for any reason. The GNSS, on the other hand, has a lower update rate than the INS, and the satellite signal can be lost or fragmented due to environmental circumstances, including mountains, high buildings, tunnels, and multi-path reflections [58; 59]. GNSS provides highly accurate guidance information, and INS has a continuously high update rate. However, there are drawbacks, such as the GNSS measurement's low update rate, the possibility of an absence signal, and the IMU's drift characteristics in the INS. These drawbacks of both individual frameworks are addressed, and both systems' advantages are merged via the integration synthesis of GNSS/INS. So far, integration of the GNSS/INS framework has usually been established to determine the vehicle's position and attitude, which can be implemented by using a Kalman filter [60; 13; 61; 62; 63]. The problem in all the integration architectures mentioned above is that the INS data rate is higher than the GNSS data rate. Consequently, a predictor should be used to predict the in-between sampling instants of the GNSS receiver in order to synchronize with INS data before the integration process and overcome the GNSS receiver's stopping time (blocking data) when the signal is lost for a few seconds [64]. Hence, the prediction process benefits two critical solutions: first, it gives a high GNSS data rate, and second, it overcomes the problem of GNSS signal loss.

Different prediction algorithms are used in the output of the GNSS or GPS receivers before integration with the INS data for synchronization purposes. In reference [65], a method proposed to predict GPS data was shown by using a Normalized Least-Mean-Square (NLMS) algorithm. Furthermore, a different blocking time of GPS is taken to indicate the ability of the algorithms for GPS prediction data. In reference [66], a comparison between the performance of Radial Basis Function Neural Networks (RBFNN) and Wavelet Neural Networks (WNNs) for GPS data prediction is presented, and the results show that WNNs are more efficient than RBFNNs. Additionally, a carrier phase prediction method at the baseband signal processing level to solve GNSS blocking signals in challenging environments was proposed in reference [67].

DOI:10.15774/PPKE.ITK.2023.002

# Chapter 2

# Nonlinear thermal modeling of a CubeSat

## 2.1 Background

There has been an increasing interest in small satellites by governments and industry, justified primarily by their low cost, mass, size, short development time, and relative simplicity. The cost of sending vehicles and satellites into space and the related large amount of work involved result in infrequent missions. Therefore, the engineers working on space systems usually do not get many opportunities to practice launch and flight operations. CubeSat is a microsatellite, consistent with the CubeSat Design Specification developed by California State Polytechnic. This standardized type of satellite poses limits on both the size and weight of the space segment. The size of this satellite cannot exceed roughly 10x10x10 $cm^3$ and a mass of 1 kg. At present, very few CubeSats have flown with an onboard propulsion system to provide attitude control or perform orbital maneuvers. Thus, there is a need to investigate the possibility of installing a propellant tank and performing thermal simulations to obtain a starting point for adding a propulsion system to CubeSat.

To modify either the CubeSat surface optical properties or the solar panel ratios attached to specific satellite sides, we need a thermal model for simulations and control design. Thermal Mathematical Model (TMM) is responsible for simulating the transient thermal behavior of the CubeSat's key parts through its orbit. The TMM together with the simulation results are introduced to study the temperature variations and the thermal stability of the CubeSat surface and its propellant tank [P1; 68]. Furthermore, the TMM is reformulated as a unified model concerning the solar panel ratio that partially covers the CubeSat surface [P2]. Finally, depending on this new model, an equivalent quasi-LPV model is composed [P2; 43] as the first step toward applying the Model Predictive Controller (MPC).

In this Chapter, the thermal simulation of the fuel tank is shown for several cases based on different variations of the satellite surface coating. Also, a new model concerning the solar panels' ratios ($\lambda$) is parallelly simulated with the original TMM under the same constraints to ensure its validity. The solar panels are the most critical part of CubeSat due to the power limits. Thus, to make the effect of varying the solar panels' ratios more elaborated, additional simulations with different values of $\lambda$ are also presented.

DOI:10.15774/PPKE.ITK.2023.002

The Chapter is organized as follows: A brief mathematical model description of the CubeSat's dynamical thermal behavior *TMM* is formulated in section 2.3. This TMM is employed to simulate different surface compositions of a CubeSat in section 2.3.5. Then an equivalent model depicting the thermal behavior of CubeSat's specific parts with respect to $\lambda$ is derived in section 2.4. The equivalent model is also employed to simulate the CubeSat thermal behavior with the TMM in section 2.6. Additionally, the range of dynamical behavior of the CubeSat for different values of $\lambda$ is shown in section 2.4.2. Finally, a quasi-LPV model formulation is presented in Section 2.5.

## 2.2 System description

The intended use of the model developed in this thesis is twofold: 1) to study the effect of different surface compositions (including solar panels) on the CubeSat's temperature, and 2) to evaluate the possibility of installing a propellant tank in the CubeSat. Concerning the modeling, the following assumptions are made:

### 2.2.1 Structural

CubeSat is a cubic structural bus with a total mass of 1 kg composed of six faces as walls. The basic structure of these faces is composed of the aluminum alloy 6061-T6 with various optical surface properties. These properties are based on uncoated surfaces for one experiment and coated with a magnesium oxide-aluminum oxide paint for the others. The nitrogen fuel tank, made of stainless steel with a diameter of 5 cm, is planned to be installed in the center of this small satellite and is assumed to contain an internal gas subjected to 100 bar of pressure at 298 K as an initial temperature.

### 2.2.2 Orbital

This satellite is devised for a circular Low Earth Orbit (LEO). The total orbital period ($P$) is 1.5 h. However, its orbital motion is assumed to be identical when exposed to solar radiation and during shadow passage at an altitude of 300 km and an inclination of zero. Face 3 is directed towards the Earth throughout its orbit. Faces 1, 2, and 4 are exposed to the Sun with regard to the orbital motion of the satellite. Finally, faces 5 and 6 are directed toward space along the satellite orbit, as shown in Figure 2.1.

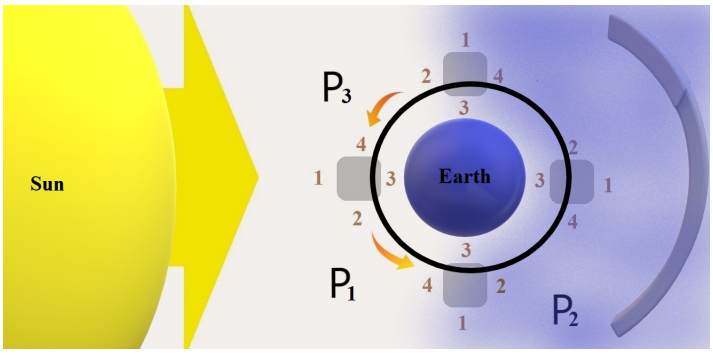


**Figure 2.1:** CubeSat orbital motion includes three time intervals (P1, P2, and P3)

DOI:10.15774/PPKE.ITK.2023.002

### 2.2.3 Thermal

The CubeSat's six faces are considered to have a uniform temperature distribution. The conductive heat transfer between the central fuel tank and the satellite's surfaces is ignored to simplify the thermal modeling calculations. Face 3 is exposed to infrared radiation from the Earth along the orbit and albedo during the luminous orbit intervals [34]. The thermal rate of power dissipation generated from the operation of CubeSat's elements is assumed to be 2 W. The thermal boundary limits for the fuel tank are 228 K and 338 K, and for the surface area of the satellite, they are 173 K and 373 K.

## 2.3 Nonlinear dynamic thermal model

The problem concerns the formulation of the model, which is, on the one hand, simple enough to reduce the expenditure, on the other hand, detailed enough to present an adequate description of the physical surroundings [1]. The primary purpose of these calculations is to divide the periodic motion of the satellite (with period $P$) into three intervals (parts), as shown in Figure 2.1. The first interval ($P_1$) starts with an initial time of $t = 0$ sec when face 1 faces the Sun and ends at a time of $t = 1350$ sec when face 4 faces the Sun. The second interval ($P_2$) is an eclipse interval between $t = 1351$ sec and $t = 4050$ sec. The third interval ($P_3$) starts at $t = 4051$ sec when face 2 faces the Sun and ends at the end of the satellite period at $t = 5399$ sec.

### 2.3.1 First interval equations

$$\text{Interval}\, P_1 : t = 0 \rightarrow t = \frac{P}{4}$$

The CubeSat spends a quarter of its orbital period in this luminous part. During this time interval, the satellite's surface receives direct solar and albedo radiation depending on its orbital motion. In addition, the satellite emits thermal IR radiation into space; however, only face 3 receives infrared radiation from Earth because it is facing this planet along the orbit [69]. The rate of heat transfer between face 1, the external environment, and the spherical fuel tank during the first interval can be represented by

$$(m_{\text{Al}} C_p + m_{\text{sc}} C_p^{\text{sc}}) \frac{dT_1}{dt} = G_{\text{s}} a_{\text{s}}^{\text{Al-sc}} A \cos\left(\frac{2\pi t}{P}\right) + \dot{Q} + \dot{Q}_{F_1} - \varepsilon_{\text{IR}}^{\text{Al-sc}} \sigma A T_1^4 \qquad (2.1)$$

where $m_{\text{Al}}$ denotes the mass of aluminum, $C_p$ stands for the specific heat of aluminum (980 J/(kg·K)), $m_{\text{sc}}$ represents the mass of the solar panel, $C_p^{\text{sc}}$ is the specific heat of the solar panel (1600 J/(kg·K)), $T_1$ denotes the temperature of face 1, $G_{\text{s}}$ stands for the solar constant (1367 W/m$^2$), and $a_{\text{s}}^{\text{Al-sc}}$ represents the average solar absorptance of aluminum and the solar panel which is calculated as (Al %$\cdot a_{\text{s}}^{\text{Al}}$+sc %$\cdot a_{\text{s}}^{\text{sc}}$), where Al % and sc % denote the percentages of aluminum and solar panels in the cover, respectively. $A$ stands for the surface area of the face (0.01 m$^2$), $\dot{Q}$ represents the thermal rate of power dissipation, $\dot{Q}_{F_1}$ denotes the radiative heat transfer between face 1 and the tank, $\varepsilon_{\text{IR}}^{\text{Al-sc}}$ is the average infrared emissivity of Al and sc which is calculated as (Al %$\cdot\varepsilon_{\text{Al}}$+sc %$\cdot\varepsilon_{\text{sc}}$) and $\sigma$ stands for the Stefan-Boltzmann constant ($5.669 \cdot 10^{-8}$W/m$^2$ K$^4$) [26].

DOI:10.15774/PPKE.ITK.2023.002

The rate of heat transfer between face 2, the external environment, and the spherical fuel tank during the first interval can be described as

$$(m_{\mathrm{Al}} C_p + m_{\mathrm{sc}} C_p^{\mathrm{sc}}) \frac{dT_2}{dt} = \dot{Q} + \dot{Q}_{F_2} - \varepsilon_{IR}^{\text{Al-sc}} \sigma A T_2^4 \tag{2.2}$$

where $T_2$ denotes the temperature of face 2 and $\dot{Q}_{F_2}$ stands for the radiative heat transfer between face 2 and the tank.

The rate of heat transfer between face 3, the external environment, and the spherical fuel tank during the first interval can be described as

$$m C_p \frac{dT_3}{dt} = AF G_{\mathrm{s}} a_{\mathrm{s}}^{\mathrm{Al}} F_{\mathrm{sE}} A \cos\left(\frac{2\pi t}{P}\right) + \dot{Q} + \dot{Q}_{F_3} + a_{\mathrm{IR}}^{\mathrm{Al}} \sigma A T_{\mathrm{E}}^4 - \varepsilon_{\mathrm{IR}}^{\mathrm{Al}} \sigma A T_3^4 \tag{2.3}$$

where $m$ denotes the mass of the face (0.04 kg), $F_{\mathrm{sE}}$ stands for the view factor between the face of the satellite and the Earth which is almost one [69], $T_3$ represents the temperature of face 3, $\dot{Q}_{F_3}$ is the radiative heat transfer between face 3 and the tank, $AF$ denotes the factor on the albedo (0.28), $a_{\mathrm{s}}^{\mathrm{Al}}$ stands for the solar absorptivity of aluminum, $a_{\mathrm{IR}}^{\mathrm{Al}}$ represents the infrared absorptivity of aluminum, $T_{\mathrm{E}}$ is the reference temperature of the Earth (255 K) and $\varepsilon_{\mathrm{IR}}^{\mathrm{Al}}$ denotes the infrared emissivity of aluminum.
The rate of heat transfer between face 4, the external environment, and the spherical fuel tank during the first interval can be modeled as

$$\left(m_{\mathrm{Al}} C_p + m_{\mathrm{sc}} C_p^{\mathrm{sc}}\right) \frac{dT_4}{dt} = G_{\mathrm{s}} a_{\mathrm{s}}^{\text{Al-sc}} A \sin\left(\frac{2\pi t}{P}\right) + \dot{Q} + \dot{Q}_{F_4} - \varepsilon_{\mathrm{IR}}^{\text{Al-sc}} \sigma A T_4^4 \tag{2.4}$$

where $T_4$ denotes the temperature of face 4 and $\dot{Q}_{F_4}$ stands for the radiative heat transfer between face 4 and the tank.
The rate of heat transfer between face 5, the external environment, and the spherical fuel tank during the first interval can be described as

$$m C_p \frac{dT_5}{dt} = \dot{Q} + \dot{Q}_{F_5} - \varepsilon_{\mathrm{IR}}^{\mathrm{Al}} \sigma A T_5^4 \tag{2.5}$$

where $T_5$ denotes the temperature of face 5 and $\dot{Q}_{F_5}$ stands for the radiative heat transfer between face 5 and the tank.

The rate of heat transfer between face 6, the external environment, and the spherical fuel tank during the first interval can be described as

$$m C_p \frac{dT_6}{dt} = \dot{Q} + \dot{Q}_{F_6} - \varepsilon_{\mathrm{IR}}^{\mathrm{Al}} \sigma A T_6^4 \tag{2.6}$$

where $T_6$ denotes the temperature of face 6 and $\dot{Q}_{F_6}$ stands for the radiative heat transfer between face 6 and the tank.

DOI:10.15774/PPKE.ITK.2023.002

### 2.3.2 Second interval equations

$$\text{Interval}\, P_2 : t = \frac{P}{4} \rightarrow t = \frac{3}{4}P$$

This interval concerns the duration of an eclipse. The satellite spends half of its orbital period in an eclipse. During this interval, the satellite's surface receives neither direct solar nor albedo radiation, while face 3 still receives IR radiation from Earth because it faces it. The satellite emits thermal IR radiation into space. Therefore, the heat transfer rates of the CubeSat's faces (1, 3, and 4) have slightly changed in their equations compared to the first interval as represented in the following equations:

$$(m_{\text{Al}} C_p + m_{\text{sc}} C_p^{\text{sc}}) \frac{dT_1}{dt} = \dot{Q} + \dot{Q}_{F_1} - \varepsilon_{\text{IR}}^{\text{Al-sc}} \sigma A T_1^4 \tag{2.7}$$

$$m C_p \frac{dT_3}{dt} = \dot{Q} + \dot{Q}_{F_3} + a_{\text{IR}}^{\text{Al}} \sigma A T_{\text{E}}^4 - \varepsilon_{\text{IR}}^{\text{Al}} \sigma A T_3^4 \tag{2.8}$$

$$(m_{\text{Al}} C_p + m_{\text{sc}} C_p^{\text{sc}}) \frac{dT_4}{dt} = \dot{Q} + \dot{Q}_{F_4} - \varepsilon_{\text{IR}}^{\text{Al-sc}} \sigma A T_4^4 \tag{2.9}$$

Moreover, the equation for face 2 is similar to the equations ((2.7) and (2.9)) for faces 1 and 4, respectively. The equations for faces 5 and 6 are the same as they were in the first interval; see equations (2.5) and (2.6).

### 2.3.3 Third interval equations

$$\text{Interval}\, P_3 : t = \frac{3}{4}P \rightarrow t = P$$

The satellite spends the last quarter of its orbital period in this second luminous part. During this time interval, the satellite's surface receives and emits thermal radiation in a similar manner to interval 1, with only a slight change in the equation for face 2. Therefore, the CubeSat's Faces 1, 3, 5, and 6 equations are identical to the first interval equations for these sides; see equations (2.1), (2.3), (2.5), and (2.6). Also, the face 4 equation is the same as the face 4 equation in the second interval; see equation (2.9). Then the rate of heat transfer between the CubeSat face 2, the external environment, and the spherical fuel tank in the third interval can be modeled as

$$(m_{\text{Al}} C_p + m_{\text{sc}} C_p^{\text{sc}}) \frac{dT_2}{dt} = G_{\text{s}} a_{\text{s}}^{\text{Al-sc}} A \left| \sin\left(\frac{2\pi t}{P}\right) \right| + \dot{Q} + \dot{Q}_{F_2} - \varepsilon_{IR}^{Al\text{-}sc} \sigma A T_2^4 \tag{2.10}$$

### 2.3.4 The transient heat transfer of the spherical propellant tank

The rate of radiative heat transfer between the faces of the satellite and the fuel tank can be described as the following equation:

$$(m_{\text{s}} C_p^{\text{s}} + m_{\text{g}} C_v) \frac{dT_{\text{t}}}{dt} = -\sum_{1}^{6} \dot{Q}_{F_n} \tag{2.11}$$

where $m_{\text{s}}$ denotes the mass of stainless steel, $C_p^{\text{s}}$ stands for the specific heat of stainless steel (504 J/(kg·K)), $m_{\text{g}}$ represents the mass and $C_V$ the specific heat of nitrogen (743 J/(kg·K)), and $T_{\text{t}}$ is the temperature of the tank.

DOI:10.15774/PPKE.ITK.2023.002

The radiative heat transfer between each face and the tank $\dot{Q}_{F_n}$, depending on which face it applies to, can be described as

$$\dot{Q}_{F_n} = F_{\text{ft}}\varepsilon\sigma A(T_{\text{t}}^4 - T_n^4) \tag{2.12}$$

The view factor between the face in question and the fuel tank is given by $F_{\text{ft}} = \frac{1}{(1+H)^2}$ (see, e.g. [31]), where $H$ denotes the ratio of the distance between the spherical surface of the tank to the surface of the internal face ($h = 0.025$ m) in terms of the radius ($r = 0.025$ m), which is expressed as $H = \frac{h}{r}$.

The mass of the solar panel $m_{\text{sc}}$ per unit area is on average 850 g/m$^2$; thus, the mass of the solar panel as a proportion of the total face mass is determined by the equation ($m_{\text{sc}} = 850$ g/m$^2 \cdot A \cdot$ sc %). The total mass of the tank $m_{\text{t}}$ is assumed to be 0.1 kg, so the mass of nitrogen gas was calculated by considering the initial temperature and total pressure of the tank.

The optical surface properties are shown in Table 2.1, and the masses of both nitrogen gas and the tank are shown in Table 2.2. Hence, it is necessary to calculate the properties of the average materials to conduct a thermal analysis.

In addition to these faces' radiation absorptivity, radiation emissivity can be calculated as the average emissivity of aluminum and the solar panel, as shown in Table 2.3.

**Table 2.1:** CubeSate surface characteristics.

| | Aluminum uncoated | Aluminum coated | solar panels |
|---|---|---|---|
| Specific Heat [J/(kg·K)] | 980 | 980 | 1600 |
| Emissivity (thermal) | 0.08 | 0.92 | 0.85 |
| Absorptivity (solar) | 0.379 | 0.09 | 0.92 |

**Table 2.2:** CubeSat tank specification.

| | Stainless Steel | Nitrogen |
|---|---|---|
| Specific Heat [J/(kg·K)] | 504 | 743 |
| Mass [kg] | 0.0926 | 0.0074 |

**Table 2.3:** Optical surface properties of CubeSat.

| Cube Face | Coverage | $\varepsilon$ | a |
|---|---|---|---|
| 1,2 and 4 | 70% Al, 30% sc | 0.89 | 0.33 |
| | 30% Al, 70% sc | 0.87 | 0.67 |
| 3,5 and 6 | Al painted | 0.92 | 0.09 |

DOI:10.15774/PPKE.ITK.2023.002

### 2.3.5 Analysis of different surface compositions

The thermal behavior investigations of CubeSat faces and central propellant tank are presented for several cases based on:

- Uncoated surfaces.
- Surfaces coated with magnesium oxide-aluminum oxide paint.
- Different feasible options of solar panel ratios.

The Matlab ODE45 solver has been exploited to simulate CubeSat temperatures with specific optical properties of the surface materials and different solar panel ratios. The default relative error tolerance of 1e-3 and the default absolute tolerance of 1e-6 for each component, and plotting the first component of the solution with the simulation time step of 1 sec. Furthermore, all the initial conditions were centered around the room temperature, which is skewed beyond the constraint for special calculations, as shown in Figure 2.2.

#### CubeSat surface is composed of unpolished aluminum

In this case, the thermal simulations of the faces and fuel tank were conducted according to the assumption that the satellite faces are composed of the aluminum alloy 6061-T6. The CubeSat thermal behavior was simulated along the orbit by solving the model's intervals equations with the ODE45 solver in Matlab.

1 - The thermal simulation of the faces and spherical fuel tank during one orbital period (time span from 0 sec to 5399 sec) is shown in Figure 2.2, A. The simulation of the temperature of the tank during this orbital period is shown in Figure 2.2, B. It can be seen that the predefined temperature limits are not fulfilled in this case since the minimum temperatures of the CubeSat surface and fuel tank exceed 460 K during its orbital period.

2 - The thermal simulation of the faces and spherical fuel tank during several orbits (8 orbital periods with a time span of 12 h to illustrate long-term operations) is shown in Figure 2.2, C, and the simulation of the temperature of the tank during these orbital periods is shown in Figure 2.2, D.

#### CubeSat surface is composed of polished aluminum

The CubeSat surface and fuel tank thermal simulations were conducted according to the assumption that the satellite's surface was composed of aluminum coated with magnesium oxide-aluminum paint. By using the assumed time span of each interval, the results are shown below:

1 - The thermal simulations of the faces and spherical fuel tank during one orbital period (time span from 0 sec to 5399 sec) are shown in Figure 2.3, A. The simulation of the temperature of the tank during this orbital period is shown in Figure 2.3, B. It can be seen that all the defined temperature limits are adhered to in this case. In addition, it would be worthwhile to mention that the CubeSat face (3, 5, and 6) temperatures also dropped because the satellite surface has a thermal interconnection, see section 2.3.4.

2 - The thermal simulation of the faces and spherical fuel tank over 8 orbital periods (a time span of 12 h) is shown in Figure 2.3, C, and the simulation of the temperature of the tank during these orbital periods is shown in Figure 2.3, D.

DOI:10.15774/PPKE.ITK.2023.002

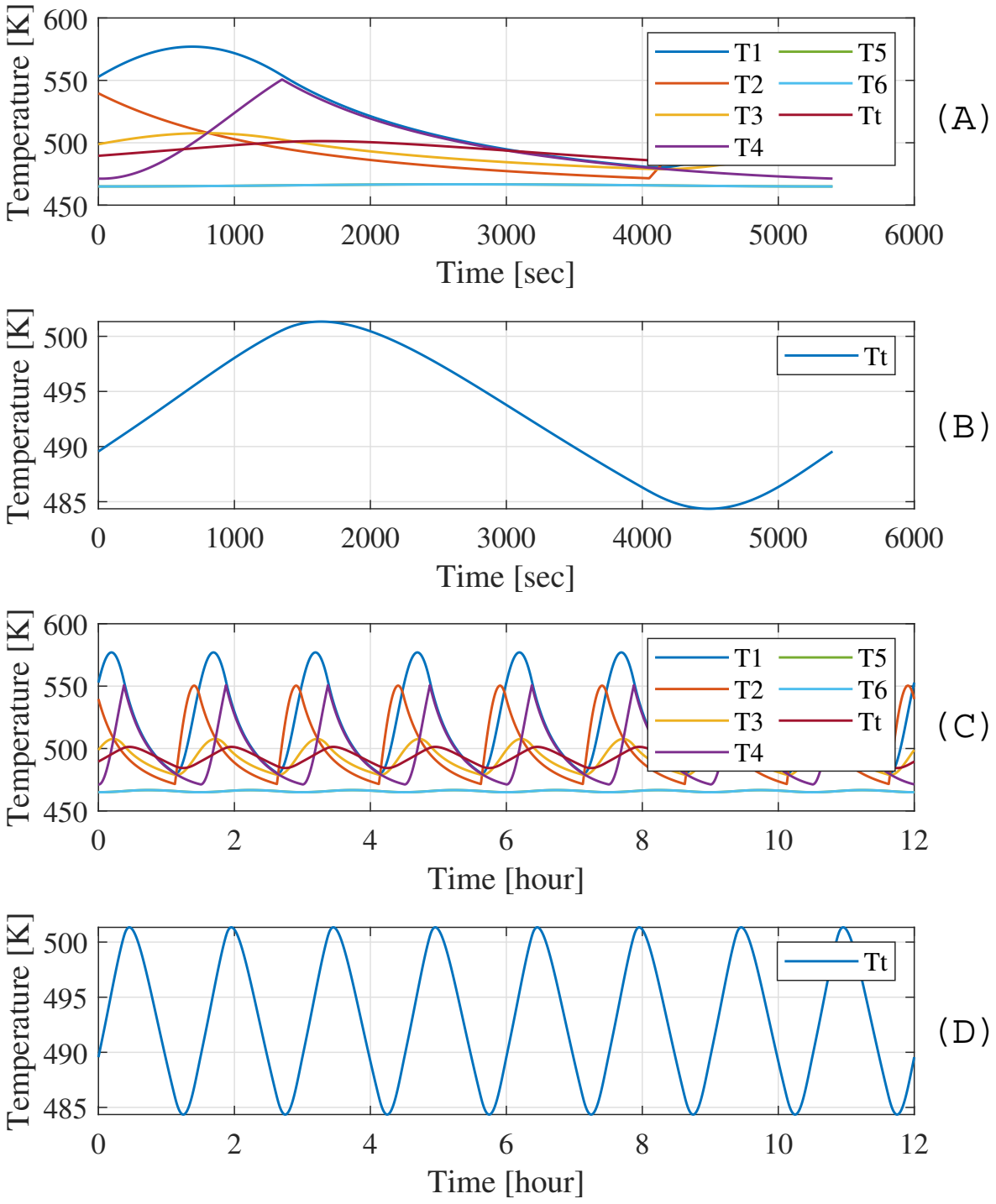


**Figure 2.2:** Simulation of the CubeSat heat rates assuming aluminum-uncoated surface over orbital motion (*A & B refer to one orbital simulation, C & D refer to eight times orbitals simulation*). (T1, ..., T6) refers to the temperatures of faces 1, ..., 6, respectively, and ($T_t$) denotes the temperature of the tank.

DOI:10.15774/PPKE.ITK.2023.002

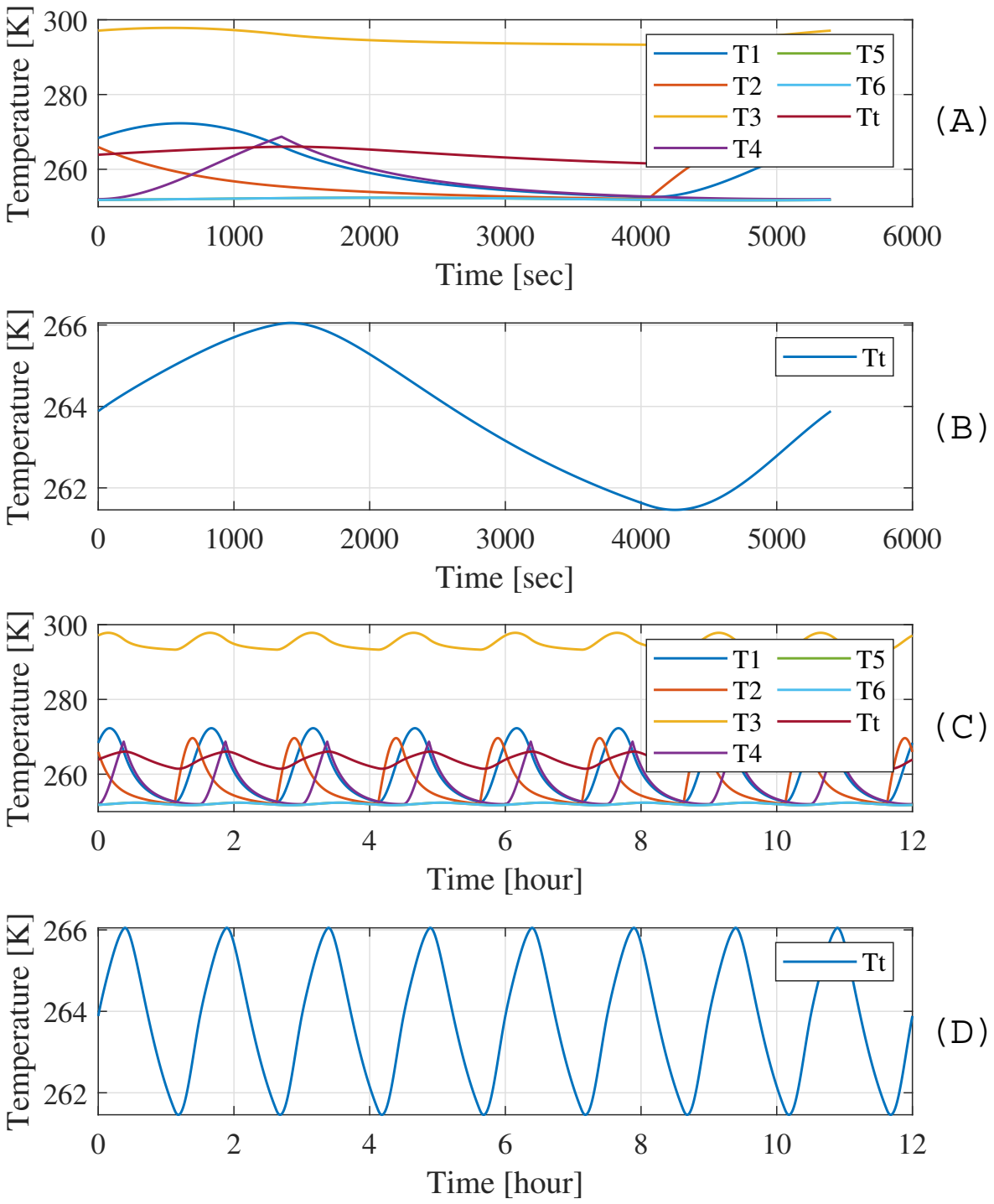


**Figure 2.3:** Simulation the CubeSat heat rates assuming aluminum-coated surface over orbital motion (*A & B refer to one orbital simulation, C & D refer to eight times orbital simulation*)

DOI:10.15774/PPKE.ITK.2023.002

**The CubeSat faces exposed to the Sun during its orbit are covered with solar panels ratio of $\lambda = 30\%$**

In this case, these three sides of the CubeSat are assumed to be composed of 70% aluminum and 30% solar panels, and the other faces are coated with magnesium oxide-aluminum oxide paint. The simulation results are as follows:

1 - The thermal simulation of the faces and spherical fuel tank during one orbital period (a time span of 0 sec to 5399 sec) is shown in Figure 2.4, A. The simulation of the temperature of the tank during this orbital period is also shown separately in Figure 2.4, B. The results show that the tank's temperature varied between a maximum of 281.9 K and a minimum of 265.4 K, while the temperatures of the faces also remained within the given temperature limits.

2 - The thermal simulation of the faces and spherical fuel tank over 8 orbital periods (a time span of 12 h) is shown in Figure 2.4, C, and the simulation of the temperature of the tank during these orbital periods is shown in Figure 2.4, D.

**The CubeSat faces exposed to the Sun during its orbit are covered with solar panels ratio of $\lambda = 70\%$**

The results, according to the assumption that three sides of the CubeSat are composed of 30% aluminum and 70% solar panels while the rest surface is coated with magnesium oxide-aluminum oxide paint, are shown below:

1 - The thermal simulation of the faces and spherical fuel tank during one orbital period (time span from 0 sec to 5399 sec) is shown in Figure 2.5, A, while simulation of the temperature of the tank during this orbital period is shown in Figure 2.5, B. The results show that the tank's temperature varied between a maximum of 302.4 K and a minimum of 270.6 K. In contrast, the temperatures of the faces were within thermal limits.

2 - The thermal simulation of the faces and spherical fuel tank over 8 orbital periods (a time span of 12 h) is shown in Figure 2.5, C, also the simulation of the temperature of the tank during these orbital periods is shown in Figure 2.5, D.

## 2.4 Equivalent thermal model of a CubeSat

In the second interval $P_2$, the CubeSat spends half of its orbital time in the shadow of the Earth (eclipse part). In the third part $P_3$, the satellite orbits again in the sight of the Sun (second luminous part). In section 2.3, a mathematical model is given for the thermal behavior of the satellite's surface and tank (separately for each orbital interval $P_1$, $P_2$ and $P_3$) in the form of nonlinear *switched* ordinary differential equations . In this section, the seven governing equations of the CubeSat's thermal dynamics are rewritten into an equivalent unified model concerning $\lambda$, which indicates the solar panel ratio. The *equivalent* "unified" state-space model formulation is done as follows:

DOI:10.15774/PPKE.ITK.2023.002

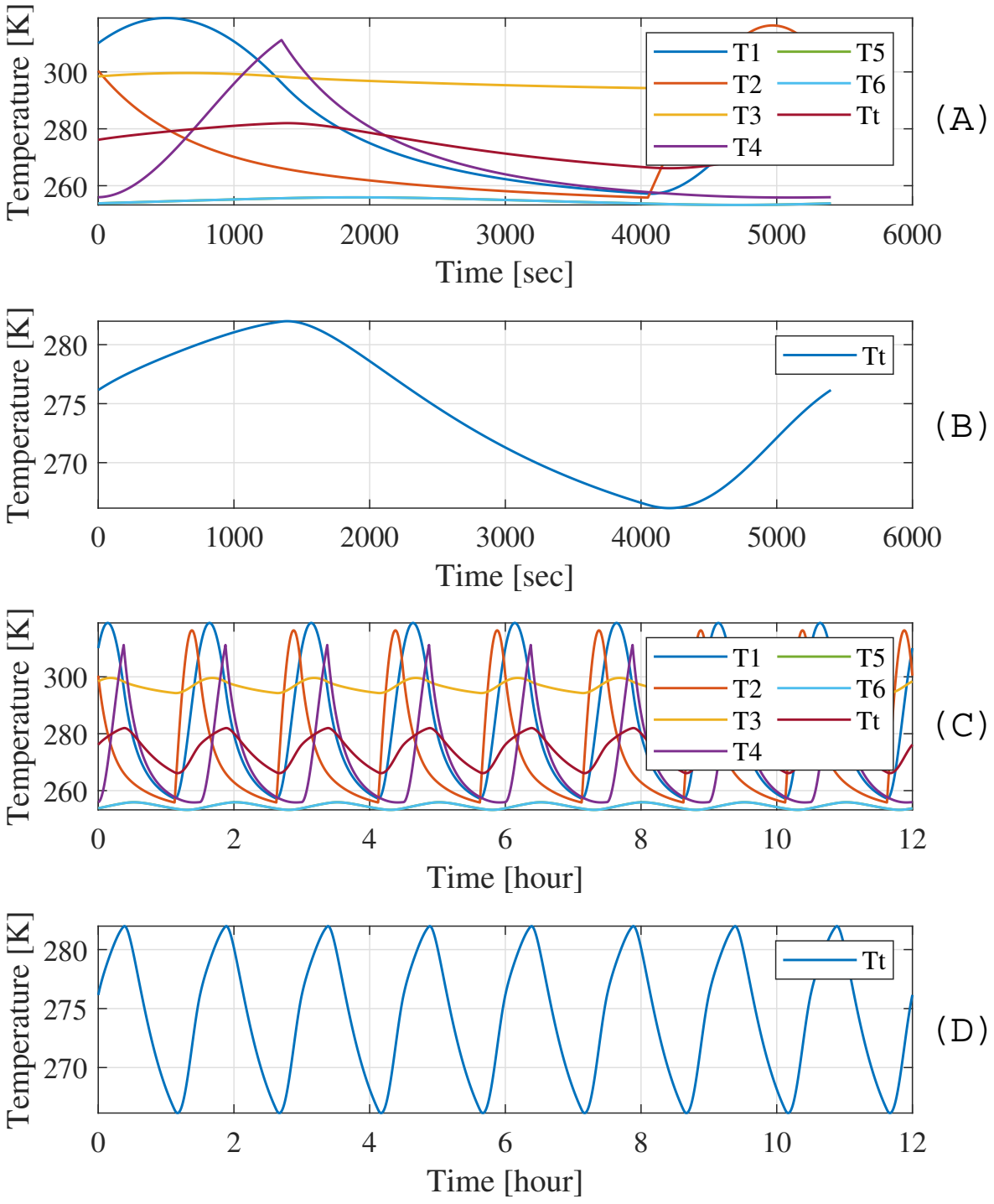


**Figure 2.4:** Simulation of the CubeSat heat rates performs 30% sc, covering three predefined faces over orbital motion (*A & B refer to one orbital simulation, C & D refer to eight times orbital simulation*)

DOI:10.15774/PPKE.ITK.2023.002

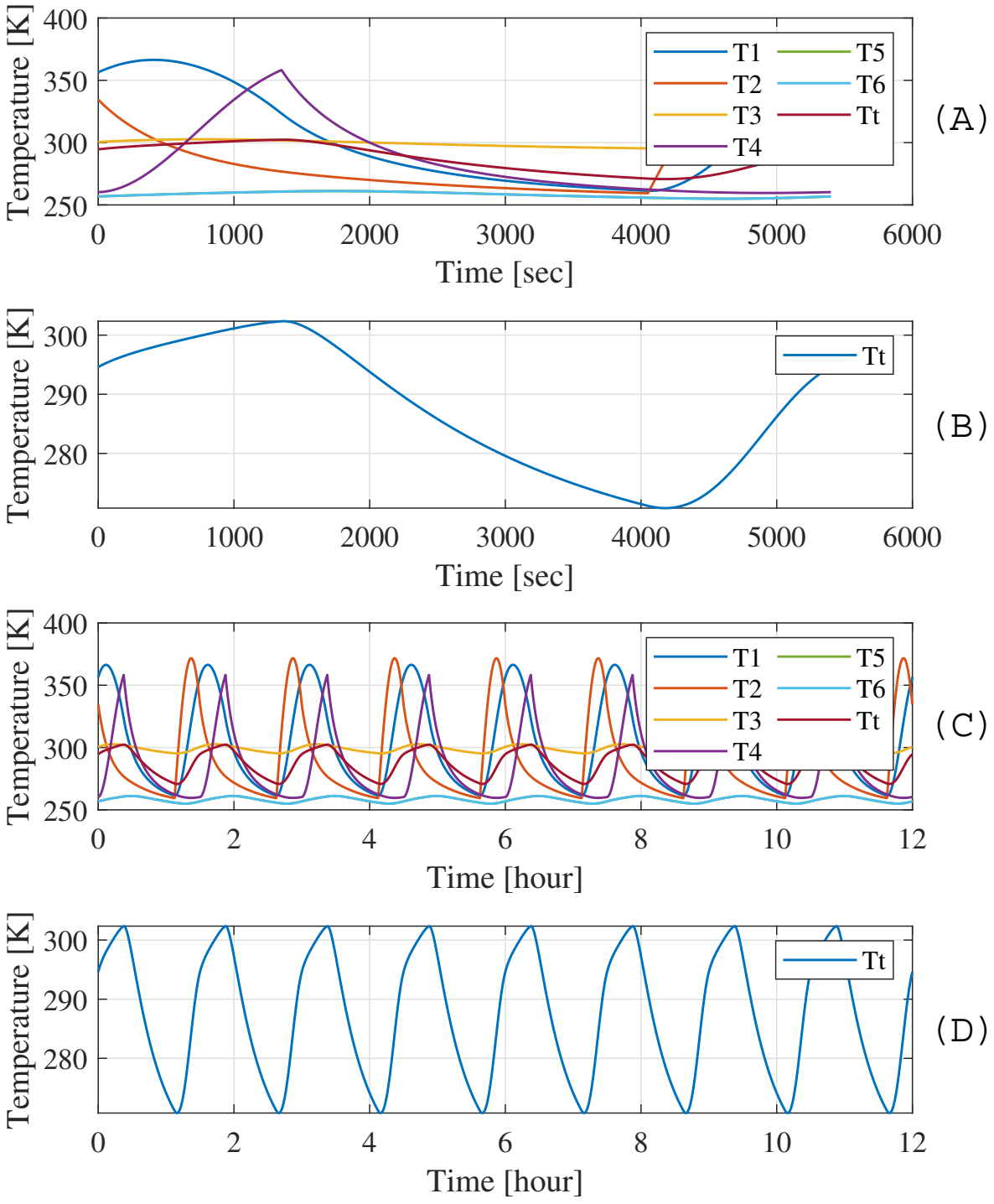


**Figure 2.5:** Simulation of the CubeSat heat rates performs 70% sc, covering three predefined faces over orbital motion (*A & B refer to one orbital simulation, C & D refer to eight times orbital simulation*)

DOI:10.15774/PPKE.ITK.2023.002

### 2.4.1 Formulation of an equivalent thermal model

Due to the Sunlight and shadowing effects of the Earth, the temperatures of the CubeSat surface and its fuel tank typically have large fluctuations throughout the orbit. Functions $\rho_1, \rho_2, \rho_4 : \mathbb{R}_+ \to [-1, 1]$ in the equivalent thermal model are meant to describe this periodic temperature fluctuation phenomenon in the dynamics. These time-varying terms in the dynamics are considered as known *time varying parameters* given as follows:

$$\rho_1(t) = \begin{cases} \cos\left(\frac{2\pi t}{P}\right), & \text{if } \frac{2\pi t}{P} \in \left[-\frac{\pi}{2}, \frac{\pi}{2}\right] + 2k\pi, k \in \mathbb{Z}, \\ 0, & \text{otherwise}, \end{cases} \tag{2.13a}$$

$$\rho_2(t) = \begin{cases} -\sin\left(\frac{2\pi t}{P}\right), & \text{if } \frac{2\pi t}{P} \in \left[-\frac{\pi}{2}, 0\right] + 2k\pi, k \in \mathbb{Z}, \\ 0, & \text{otherwise}, \end{cases} \tag{2.13b}$$

$$\rho_4(t) = \begin{cases} \sin\left(\frac{2\pi t}{P}\right), & \text{if } \frac{2\pi t}{P} \in \left[0, \frac{\pi}{2}\right] + 2k\pi, k \in \mathbb{Z}, \\ 0, & \text{otherwise}. \end{cases} \tag{2.13c}$$

Function $\rho_1$ has nonzero values only in intervals $P_1$ and $P_3$, whereas, functions $\rho_2$ and $\rho_4$ are nonzero in intervals $P_3$ and $P_1$, respectively. The graph of functions $\rho_1$, $\rho_2$ and $\rho_4$ are illustrated in Figure 2.6.

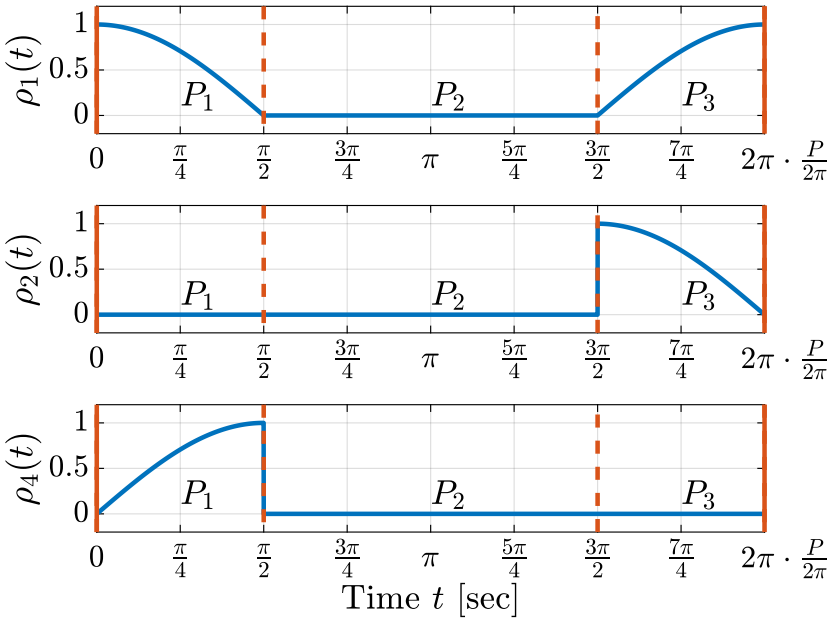


**Figure 2.6:** Graph of functions $\rho_1$, $\rho_2$ and $\rho_4$, which describe the temperature fluctuations of the CubeSat through its orbital motion

DOI:10.15774/PPKE.ITK.2023.002

The principle of constructing the new model is to integrate the three interval equations for the same face of CubeSat into one equation of the equivalent model, considering the time-varying parameter ($\rho$) and the solar panel ratios ($\lambda$). Each face in the original model in section 2.3 has three equations depending on its orbital motion's *CubeSat intervals (P1, P2, and P3)*. The new module synthesis stands upon combining these three equations into one equation concerning the ratio of solar panels, as in the following:

***First equation:***

$$Face1\begin{pmatrix} P_1 \\ P_2 \\ P_3 \end{pmatrix} = \begin{cases} (m_{\mathrm{Al}}C_p + m_{\mathrm{sc}}C_p^{\mathrm{sc}})\dfrac{dT_1}{dt} = G_{\mathrm{s}}a_{\mathrm{s}}^{\text{Al-sc}}A\cos\left(\dfrac{2\pi t}{P}\right) + \dot{Q} + \dot{Q}_{F_1} - \varepsilon_{\mathrm{IR}}^{\text{Al-sc}}\sigma AT_1^4 \\ (m_{\mathrm{Al}}C_p + m_{\mathrm{sc}}C_p^{\mathrm{sc}})\dfrac{dT_1}{dt} = \dot{Q} + \dot{Q}_{F_1} - \varepsilon_{\mathrm{IR}}^{\text{Al-sc}}\sigma AT_1^4 \\ (m_{\mathrm{Al}}C_p + m_{\mathrm{sc}}C_p^{\mathrm{sc}})\dfrac{dT_1}{dt} = G_{\mathrm{s}}a_{\mathrm{s}}^{\text{Al-sc}}A\cos\left(\dfrac{2\pi t}{P}\right) + \dot{Q} + \dot{Q}_{F_1} - \varepsilon_{\mathrm{IR}}^{\text{Al-sc}}\sigma AT_1^4 \end{cases}$$

$\therefore$ *The integration of the three equations into an equation concerning optical properties* $\lambda$ *and time-varying parameters* $\rho$ ►

$$\begin{aligned} k_{\text{Al-sc}}\dot{T}_1 =& G_s a_{\mathrm{s}}^{\text{Al-sc}}A\rho_1(t) + \dot{Q} + F_{\mathrm{Ft}}\varepsilon_{\mathrm{IR}}^{\mathrm{Al}}\sigma A(T_{\mathrm{t}}^4 - T_1^4) - \varepsilon_{\mathrm{IR}}^{\text{Al-sc}}\sigma AT_1^4 \\ =& G_s a_{\mathrm{s}}^{\mathrm{Al}}A\rho_1(t) + \dot{Q} + F_{\mathrm{Ft}}\varepsilon_{\mathrm{IR}}^{\mathrm{Al}}\sigma A(T_{\mathrm{t}}^4 - T_1^4) - \varepsilon_{\mathrm{IR}}^{\mathrm{Al}}\sigma AT_1^4 \\ &+ \lambda\left(G_s(a_{\mathrm{s}}^{\mathrm{sc}} - a_{\mathrm{s}}^{\mathrm{Al}})A\rho_1(t) - (\varepsilon_{\mathrm{IR}}^{\mathrm{sc}} - \varepsilon_{\mathrm{IR}}^{\mathrm{Al}})\sigma AT_1^4\right) \\ =& G_s a_{\mathrm{s}}^{\mathrm{Al}}A\rho_1(t) + \dot{Q} - (F_{\mathrm{Ft}}\varepsilon_{\mathrm{IR}}^{\mathrm{Al}}\sigma A + \varepsilon_{\mathrm{IR}}^{\mathrm{Al}}\sigma A)T_1^4 + F_{\mathrm{Ft}}\varepsilon_{\mathrm{IR}}^{\mathrm{Al}}\sigma AT_{\mathrm{t}}^4 \\ &+ \lambda\left(G_s(a_{\mathrm{s}}^{\mathrm{sc}} - a_{\mathrm{s}}^{\mathrm{Al}})A\rho_1(t) - (\varepsilon_{\mathrm{IR}}^{\mathrm{sc}} - \varepsilon_{\mathrm{IR}}^{\mathrm{Al}})\sigma AT_1^4\right) \end{aligned}$$

***Second equation:***

$$\begin{aligned} k_{\text{Al-sc}}\dot{T}_2 =& G_s a_{\mathrm{s}}^{\text{Al-sc}}A\rho_2(t) + \dot{Q} + F_{\mathrm{Ft}}\varepsilon_{\mathrm{IR}}^{\mathrm{Al}}\sigma A(T_{\mathrm{t}}^4 - T_2^4) - \varepsilon_{\mathrm{IR}}^{\text{Al-sc}}\sigma AT_2^4 \\ =& G_s a_{\mathrm{s}}^{\mathrm{Al}}A\rho_2(t) + \dot{Q} + F_{\mathrm{Ft}}\varepsilon_{\mathrm{IR}}^{\mathrm{Al}}\sigma A(T_{\mathrm{t}}^4 - T_2^4) - \varepsilon_{\mathrm{IR}}^{\mathrm{Al}}\sigma AT_2^4 \\ &+ \lambda\left(G_s(a_{\mathrm{s}}^{\mathrm{sc}} - a_{\mathrm{s}}^{\mathrm{Al}})A\rho_2(t) - (\varepsilon_{\mathrm{IR}}^{\mathrm{sc}} - \varepsilon_{\mathrm{IR}}^{\mathrm{Al}})\sigma AT_2^4\right) \\ =& G_s a_{\mathrm{s}}^{\mathrm{Al}}A\rho_2(t) + \dot{Q} - (F_{\mathrm{Ft}}\varepsilon_{\mathrm{IR}}^{\mathrm{Al}}\sigma A + \varepsilon_{\mathrm{IR}}^{\mathrm{Al}}\sigma A)T_2^4 + F_{\mathrm{Ft}}\varepsilon_{\mathrm{IR}}^{\mathrm{Al}}\sigma AT_{\mathrm{t}}^4 \\ &+ \lambda\left(G_s(a_{\mathrm{s}}^{\mathrm{sc}} - a_{\mathrm{s}}^{\mathrm{Al}})A\rho_2(t) - (\varepsilon_{\mathrm{IR}}^{\mathrm{sc}} - \varepsilon_{\mathrm{IR}}^{\mathrm{Al}})\sigma AT_2^4\right) \end{aligned}$$

***Third equation:***

$$\begin{aligned} k_{\mathrm{Al}}\dot{T}_3 =& AFG_s a_{\mathrm{s}}^{\mathrm{Al}}A\rho_1(t) + \dot{Q} + F_{\mathrm{Ft}}\varepsilon_{\mathrm{IR}}^{\mathrm{Al}}\sigma A(T_{\mathrm{t}}^4 - T_3^4) + a_{\mathrm{IR}}^{\mathrm{Al}}\sigma AT_E^4 - \varepsilon_{\mathrm{IR}}^{\mathrm{Al}}\sigma AT_3^4 \\ =& AFG_s a_{\mathrm{s}}^{\mathrm{Al}}A\rho_1(t) + \dot{Q} + a_{\mathrm{IR}}^{\mathrm{Al}}\sigma AT_E^4 + F_{\mathrm{Ft}}\varepsilon_{\mathrm{IR}}^{\mathrm{Al}}\sigma AT_{\mathrm{t}}^4 - (F_{\mathrm{Ft}}\varepsilon_{\mathrm{IR}}^{\mathrm{Al}}\sigma A + \varepsilon_{\mathrm{IR}}^{\mathrm{Al}}\sigma A)T_3^4 \end{aligned}$$

DOI:10.15774/PPKE.ITK.2023.002

***fourth equation:***

$$\begin{aligned}
k_{\text{Al-sc}}\dot{T}_4 =& G_s a_{\text{s}}^{\text{Al-sc}} A\rho_4(t) + \dot{Q} + F_{\text{Ft}}\varepsilon_{\text{IR}}^{\text{Al}}\sigma A(T_{\text{t}}^4 - T_4^4) - \varepsilon_{\text{IR}}^{\text{Al-sc}}\sigma A T_4^4 \\
=& G_s a_{\text{s}}^{\text{Al}} A\rho_4(t) + \dot{Q} + F_{\text{Ft}}\varepsilon_{\text{IR}}^{\text{Al}}\sigma A(T_{\text{t}}^4 - T_4^4) - \varepsilon_{\text{IR}}^{\text{Al}}\sigma A T_4^4 \\
&+ \lambda\left(G_s(a_{\text{s}}^{\text{sc}} - a_{\text{s}}^{\text{Al}})A\rho_4(t) - (\varepsilon_{\text{IR}}^{\text{sc}} - \varepsilon_{\text{IR}}^{\text{Al}})\sigma A T_4^4\right) \\
=& G_s a_{\text{s}}^{\text{Al}} A\rho_4(t) + \dot{Q} - (F_{\text{Ft}}\varepsilon_{\text{IR}}^{\text{Al}}\sigma A + \varepsilon_{\text{IR}}^{\text{Al}}\sigma A)T_4^4 + F_{\text{Ft}}\varepsilon_{\text{IR}}^{\text{Al}}\sigma A T_{\text{t}}^4 \\
&+ \lambda\left(G_s(a_{\text{s}}^{\text{sc}} - a_{\text{s}}^{\text{Al}})A\rho_4(t) - (\varepsilon_{\text{IR}}^{\text{sc}} - \varepsilon_{\text{IR}}^{\text{Al}})\sigma A T_4^4\right)
\end{aligned}$$

A similar arrangement is established for the whole TMM intervals equations. Thus, the module describing the thermal exchange mechanism of CubeSat is as presented in (2.15). Finally, the final form of CubeSat's thermal model concerning solar panels ratios, as shown in equations (2.16).

$$\begin{aligned}
k_{\text{Al-sc}}\dot{T}_1 &= e_1\rho_1(t) + \dot{Q} - (k_0 + k_1)T_1^4 + k_0 T_{\text{t}}^4 + \lambda(e_2\rho_1(t) - k_2 T_1^4) \\
k_{\text{Al-sc}}\dot{T}_2 &= e_1\rho_2(t) + \dot{Q} - (k_0 + k_1)T_2^4 + k_0 T_{\text{t}}^4 + \lambda(e_2\rho_2(t) - k_2 T_2^4) \\
k_{\text{Al-sc}}\dot{T}_4 &= e_1\rho_4(t) + \dot{Q} - (k_0 + k_1)T_4^4 + k_0 T_{\text{t}}^4 + \lambda(e_2\rho_4(t) - k_2 T_4^4) \\
k_{\text{Al}}\dot{T}_3 &= k_5\rho_1(t) + \dot{Q} + k_6 T_E^4 - (k_0 + k_1)T_3^4 + k_0 T_{\text{t}}^4 \\
k_{\text{Al}}\dot{T}_5 &= \dot{Q} - (k_0 + k_1)T_5^4 + k_0 T_{\text{t}}^4 \\
k_{\text{Al}}\dot{T}_6 &= \dot{Q} - (k_0 + k_1)T_6^4 + k_0 T_{\text{t}}^4 \\
k_{\text{T}}\dot{T}_{\text{t}} &= k_0\left(T_1^4 + T_2^4 + T_3^4 + T_4^4 + T_5^4 + T_6^4 - 6T_{\text{t}}^4\right) + \dot{Q}_{\text{c}}
\end{aligned} \tag{2.15}$$

$\therefore$ *The model concerning optical properties* $\lambda$ *and time-varying parameters* $\rho$ ►

$$\begin{aligned}
k_{\text{Al-sc}}(\lambda)\dot{T}_1 =& \dot{Q} + \dot{Q}_{\text{F}_1} + G_s\left(a_{\text{s}}^{\text{Al-sc}}(\lambda)\right)A\rho_1(t) \\
&- \left(\varepsilon_{\text{IR}}^{\text{Al-sc}}(\lambda)\right)\sigma A T_1^4 \\
k_{\text{Al-sc}}(\lambda)\dot{T}_2 =& \dot{Q} + \dot{Q}_{\text{F}_2} + G_s\left(a_{\text{s}}^{\text{Al-sc}}(\lambda)\right)A\rho_2(t) \\
&- \left(\varepsilon_{\text{IR}}^{\text{Al-sc}}(\lambda)\right)\sigma A T_2^4 \\
k_{\text{Al}}\dot{T}_3 =& \dot{Q} + \dot{Q}_{\text{F}_3} + AF G_s a_{\text{s}}^{\text{Al}} A\rho_1(t) \\
&+ a_{\text{IR}}^{\text{Al}}\sigma A T_{\text{E}}^4 - \varepsilon_{\text{IR}}^{\text{Al}}\sigma A T_3^4 \\
k_{\text{Al-sc}}(\lambda)\dot{T}_4 =& \dot{Q} + \dot{Q}_{\text{F}_4} + G_s\left(a_{\text{s}}^{\text{Al-sc}}(\lambda)\right)A\rho_4(t) \\
&- \left(\varepsilon_{\text{IR}}^{\text{Al-sc}}(\lambda)\right)\sigma A T_4^4 \\
k_{\text{Al}}\dot{T}_5 =& \dot{Q} + \dot{Q}_{\text{F}_5} - \varepsilon_{\text{IR}}^{\text{Al}}\sigma A T_5^4 \\
k_{\text{Al}}\dot{T}_6 =& \dot{Q} + \dot{Q}_{\text{F}_6} - \varepsilon_{\text{IR}}^{\text{Al}}\sigma A T_6^4 \\
k_{\text{T}}\dot{T}_{\text{t}} =& k_0(T_1^4 + T_2^4 + T_3^4 + T_4^4 + T_5^4 + T_6^4 - 6T_{\text{t}}^4) + \dot{Q}_{\text{c}}
\end{aligned} \tag{2.16}$$

where

DOI:10.15774/PPKE.ITK.2023.002

$$
\begin{cases}
e_1 = G_s\, a_{\mathrm{s}}^{\mathrm{Al}}\, A \\
e_2 = G_s\, A\, (a_{\mathrm{s}}^{\mathrm{sc}} - a_{\mathrm{s}}^{\mathrm{Al}}) \\
k_0 = F_{\mathrm{ft}}\, \sigma\, \varepsilon_{\mathrm{IR}}^{\mathrm{Al}}\, A \\
k_1 = \sigma\, \varepsilon_{\mathrm{IR}}^{\mathrm{Al}}\, A \\
k_2 = \sigma\, (\varepsilon_{\mathrm{IR}}^{\mathrm{sc}} - \varepsilon_{\mathrm{IR}}^{\mathrm{Al}})\, A \\
k_5 = AF\; G_s\, a_{\mathrm{s}}^{\mathrm{Al}}\, A \\
k_6 = \sigma\, a_{\mathrm{IR}}^{\mathrm{Al}}\, A \\
k_{\mathrm{Al}} = m\, C_p \\
k_{\mathrm{T}} = m_{\mathrm{s}} C_p^{\mathrm{s}} + m_{\mathrm{g}} C_v \\
k_{\text{Al-sc}} = m_{\mathrm{Al}} C_p + m_{\mathrm{sc}} C_p^{\mathrm{sc}} \\
k_{\text{Al-sc}}(\lambda) = m_{\mathrm{Al}} C_p + \lambda\, m_{\mathrm{sc}} C_p^{\mathrm{sc}} \\
a_{\mathrm{s}}^{\text{Al-sc}}(\lambda) = (1-\lambda)\, a_{\mathrm{s}}^{\mathrm{Al}} + \lambda\, a_{\mathrm{s}}^{\mathrm{sc}} \\
\varepsilon_{\mathrm{IR}}^{\text{Al-sc}}(\lambda) = (1-\lambda)\, \varepsilon_{\mathrm{IR}}^{\mathrm{Al}} + \lambda\, \varepsilon_{\mathrm{IR}}^{\mathrm{sc}}
\end{cases}
$$

are auxiliary parameters for more convenient notation.

The physical parameters and the time-dependent variables of the model are as follows: $T_{\mathrm{E}} = 255\,\mathrm{K}$ is the Earth's reference temperature, $T_{\mathrm{t}}\,[\mathrm{K}]$ is the tank's temperature, $a_{\mathrm{IR}}^{\mathrm{Al}} = 0.09$ is the Aluminum infrared absorptivity, $a_{\mathrm{s}}^{\mathrm{Al}} = 0.09$ is the Aluminum solar absorptivity, $a_{\mathrm{s}}^{\mathrm{sc}} = 0.92$ is the solar panel solar absorptivity, $a_{\mathrm{s}}^{\text{Al-sc}}(\lambda)$ is the Aluminum and solar panel average absorptivity, $\varepsilon_{\mathrm{IR}}^{\mathrm{Al}} = 0.92$ is the Aluminum infrared emissivity, $\varepsilon_{\mathrm{IR}}^{\mathrm{sc}} = 0.85$ is the solar panel infrared emissivity, $\varepsilon_{\mathrm{IR}}^{\text{Al-sc}}(\lambda)$ is the Aluminum and solar panel average infrared emissivity, $\dot{Q}_{\mathrm{c}}\,[\mathrm{W}]$ is the heat flux applied to the tank generated by the heater, $\dot{Q}_{\mathrm{F}_i}\,[\mathrm{W}]$ is the radiated heat transfer between the $i$th face and the tank, $\dot{Q} = 2\,\mathrm{W}$ is the power dissipated heat rate, $C_p = 980\,\mathrm{J/(kgK)}$ is the specific heat of Aluminum, $C_p^{\mathrm{s}} = 504\,\mathrm{J/(kgK)}$ is the stainless steel specific heat, $C_p^{\mathrm{sc}} = 1600\,\mathrm{J/(kgK)}$ is the solar panel specific heat, $C_v = 743\,\mathrm{J/(kgK)}$ is the Nitrogen specific heat, $m_{\mathrm{Al}} = 0.04\,\mathrm{kg}$ is the mass of an Aluminum face, $m_g = 0.0074\,\mathrm{kg}$ is the mass of nitrogen in the tank, $m_{\mathrm{s}} = 0.0926\,\mathrm{kg}$ is the mass of the tank (stainless steel), $m_{\mathrm{sat}} \simeq 1\,\mathrm{kg}$ is the total mass of CubeSat, $m_{\mathrm{sc}} = 0.0085\,\mathrm{kg}$ is the mass of solar panel covering a whole face, $G_s = 1367\mathrm{W/m^2}$ is the solar constant, $\sigma = 5.669 \cdot 10^{-8}\,\mathrm{WK^4/m^2}$ is the Stefan-Boltzmann constant, $A = 0.01\,\mathrm{m^2}$ is the area of each face, $AF = 0.28$ is the albedo factor, $F_{\mathrm{ft}} = \frac{1}{(1+H)^2}$ is the view factor between a face and the tank, where $H = h/r$, where $h = 0.025\mathrm{m}$ is the distance of the tank's surface to the face, and $r = 0.025\,\mathrm{m}$ is the tank radius.

The radiated heat transfer $\dot{Q}_{\mathrm{F}_i}$ between the $i$th face and the tank is defined as follows:

$$
\dot{Q}_{\mathrm{F}_i} = F_{\mathrm{ft}}\, \varepsilon_{\mathrm{IR}}^{\mathrm{Al}}\, \sigma A (T_{\mathrm{t}}^4 - T_i^4),\ i = 1, \ldots, 6. \tag{2.17}
$$

The tank is equipped with a supplementary heat source (*actuator* or *heater*), which generates the *control signal* $u = \dot{Q}_{\mathrm{c}}$ in the form of a (non-negative) heat flux $\dot{Q}_{\mathrm{c}}$ [36].

DOI:10.15774/PPKE.ITK.2023.002

### 2.4.2 Thermal calculation of various solar panel ratios

The solar panels are responsible for providing power to the CubeSat by converting solar energy into electric power through a photovoltaic process. Because of the surface area constraints in a CubeSat, calculating the solar panel area is important to propose the possibility of increasing the solar panel area concerning the thermal boundary conditions of the CubeSat. Therefore, the thermal performances of the CubeSat surface and tank at different solar panel ratios are presented in this subsection. The simulations are accomplished for the case in which the power dissipated inside the satellite due to the operation of its electric component is fixed at 2 W with a total orbit time of 1.5 h. Furthermore, the solar panels are supposed to cover three faces of the CubeSat due to their sun-facing sides.

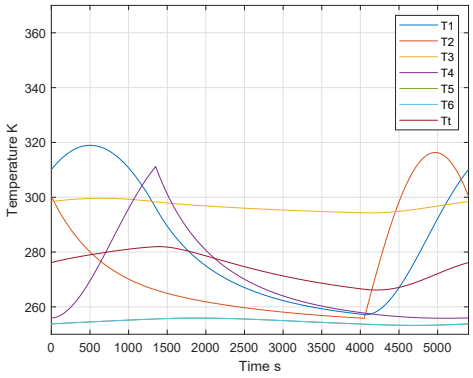


**(a)** Dynamic thermal behavior of the CubeSat surface and fuel tank when $\lambda = 0.3$

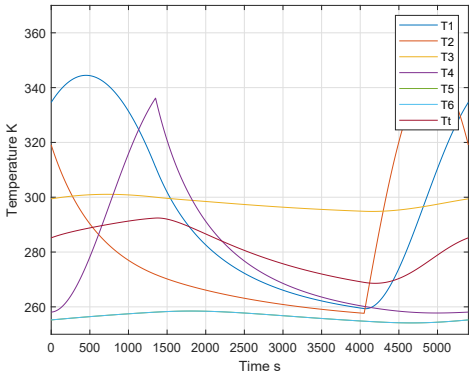


**(b)** Dynamic thermal behavior of the CubeSat surface and fuel tank when $\lambda = 0.5$

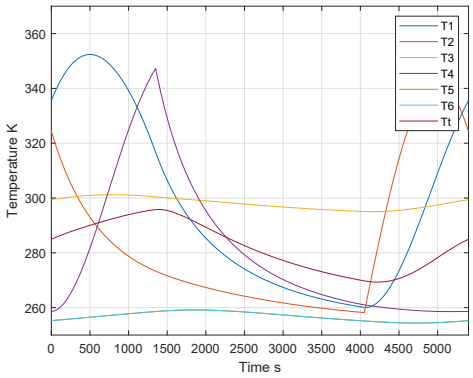


**(c)** Dynamic thermal behavior of the CubeSat surface and fuel tank when $\lambda = 0.6$

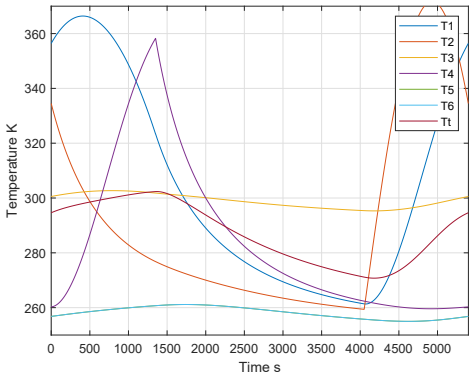


**(d)** Dynamic thermal behavior of the CubeSat surface and fuel tank when $\lambda = 0.7$

**Figure 2.7:** Dynamic thermal behavior of the CubeSat surface and fuel tank with different solar panel ratios

Figure 2.7 *(a, b, c, and d)* illustrates the thermal responses of the CubeSat's sides and tank with $\lambda =$ *(0.3, 0.5, 0.6, and 0.7)* of solar panel ratios, respectively, covering three sides of the CubeSat. The simulations successfully produced the thermal effects of increasing the ratio of the solar panels placed on CubeSat's specific walls. The CubeSat surface and tank temperatures manifested in Figure 2.7d stand much higher than the CubeSat surface and tank temperatures exposed in Figure 2.7a. So it is clearly explained that the CubeSat temperature rises by increasing the solar panels' ratio.

DOI:10.15774/PPKE.ITK.2023.002

## 2.5 Quasi-LPV formulation of the thermal model

Beginning from the nonlinear input-affine dynamical model (2.16), with seven differential equations formulated with respect to physical laws, an equivalent quasi-LPV model representation can be formulated in the following form:

$$\boxed{I_k(\lambda)\dot{x} = A(x)x + Bu + E(x,\rho)\lambda + F(\rho)\,,} \tag{2.18}$$

where the *state vector* $x$ contains seven state variables, as shown below:

$$x = \begin{pmatrix} T_1 & T_2 & T_3 & T_4 & T_5 & T_6 & T_\mathrm{t} \end{pmatrix}^T \in \mathbb{R}^n \ (n=7)$$

containing the six temperature values $(T_1,\ldots,T_6)$ of the six faces of CubeSat, respectively, and the fuel tank's temperature $T_\mathrm{t}$.

Vector $\rho$ contains the three time-varying parameter signals, as shown in the following:

$$\rho = \begin{pmatrix} \rho_1 & \rho_2 & \rho_4 \end{pmatrix}^T \in \mathbb{R}^p \ (p=3)$$

which model the periodic temperature fluctuation effect caused by the Sunlight; see equations (2.13a),(2.13b), and (2.13c).
Coefficient matrices $I_k(\lambda)$, $A(x)$, $B$, $E(x,\rho)$ and $F(\rho)$ in (2.18) are given as follows:

$$I_k(\lambda) = \mathrm{diag}(k_{\text{Al-sc}}(\lambda), k_{\text{Al-sc}}(\lambda), k_\mathrm{Al}, k_{\text{Al-sc}}(\lambda), k_\mathrm{Al}, k_\mathrm{Al}, k_\mathrm{T}), \tag{2.19a}$$

$$A(x) = \begin{pmatrix} -k_{01}T_1^3 & 0 & 0 & 0 & 0 & 0 & k_0 T_\mathrm{t}^3 \\ 0 & -k_{01}T_2^3 & 0 & 0 & 0 & 0 & k_0 T_\mathrm{t}^3 \\ 0 & 0 & -k_{01}T_4^3 & 0 & 0 & 0 & k_0 T_\mathrm{t}^3 \\ 0 & 0 & 0 & -k_{01}T_3^3 & 0 & 0 & k_0 T_\mathrm{t}^3 \\ 0 & 0 & 0 & 0 & -k_{01}T_5^3 & 0 & k_0 T_\mathrm{t}^3 \\ 0 & 0 & 0 & 0 & 0 & -k_{01}T_6^3 & k_0 T_\mathrm{t}^3 \\ k_0 T_1^3 & k_0 T_2^3 & k_0 T_3^3 & k_0 T_4^3 & k_0 T_5^3 & k_0 T_6^3 & -6k_0 T_\mathrm{t}^3 \end{pmatrix}, \tag{2.19b}$$

$$B = \begin{pmatrix} 0 \\ 0 \\ 0 \\ 0 \\ 0 \\ 0 \\ 1 \end{pmatrix},\ E(x,\rho) = \begin{pmatrix} k_4\rho_1 - k_2 T_1^4 \\ k_4\rho_2 - k_2 T_2^4 \\ 0 \\ k_4\rho_4 - k_2 T_4^4 \\ 0 \\ 0 \\ 0 \end{pmatrix},\ F(\rho) = \begin{pmatrix} \dot{Q} + k_3\rho_1 \\ \dot{Q} + k_3\rho_2 \\ \dot{Q} + k_5\rho_1 + k_6 T_\mathrm{E}^4 \\ \dot{Q} + k_3\rho_4 \\ \dot{Q} \\ \dot{Q} \\ 0 \end{pmatrix}, \tag{2.19c}$$

where

$$\begin{cases} k_{01} = k_0 + k_1 \\ k_1 = \sigma\ \varepsilon_\mathrm{IR}^\mathrm{Al}\ A \\ k_2 = \sigma\ (\varepsilon_\mathrm{IR}^\mathrm{sc} - \varepsilon_\mathrm{IR}^\mathrm{Al})\ A \\ k_3 = G_s\, a_\mathrm{s}^\mathrm{Al} A \\ k_4 = G_s\, (a_\mathrm{s}^\mathrm{sc} - a_\mathrm{s}^\mathrm{Al}) A \\ k_5 = AFG_s\, a_\mathrm{s}^\mathrm{Al} A \\ k_6 = a_\mathrm{IR}^\mathrm{Al}\, \sigma A \end{cases}$$

are auxiliary constants.

DOI:10.15774/PPKE.ITK.2023.002

## 2.6 Equivalent model evaluation

In this section, we are going through the simulations of the new model together with the original model to illustrate and compare the CubeSat thermal behaviors in these models. A Matlab Simulink model has been employed to analyze the CubeSat surface and tank thermal performance of the equivalent model in parallel with the TMM in section 2.3 even with the same features as section 2.3.5. So the new model simulation has been done for the case that three faces of the satellite are covered by 30% of solar panels ($\lambda$= 0.3), as shown in Figure 2.8b. Also, part (a) of that figure introduces the Matlab Simulink constructions for the two models, which gave us the computational results. The simulation results of the mutual

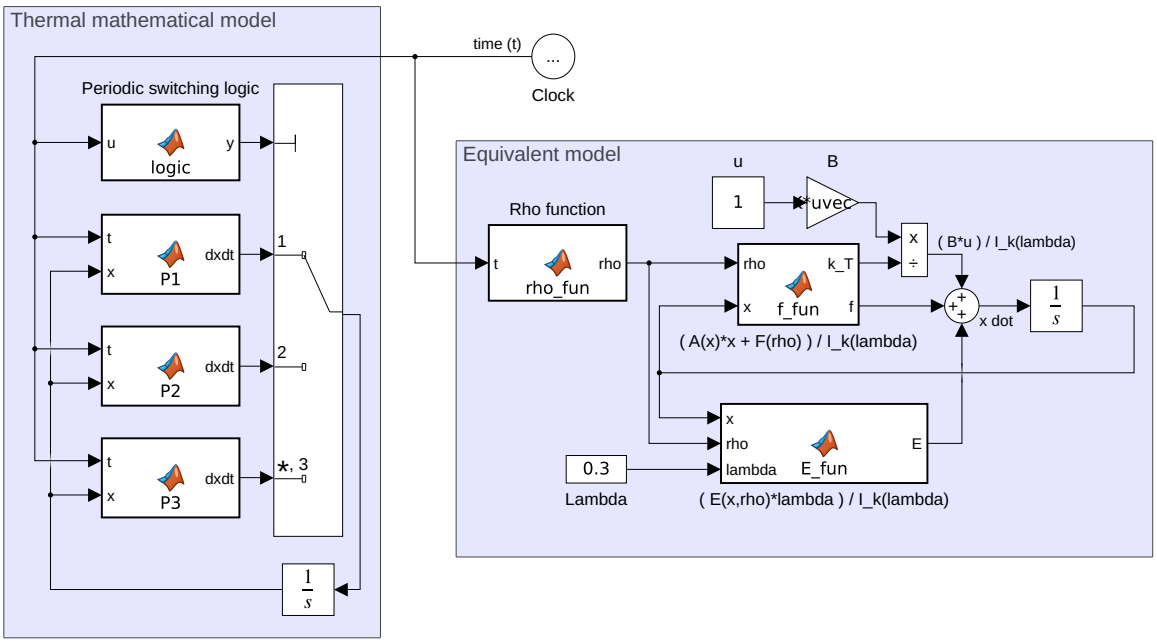


**(a)** Matlab Simulink diagrams of the models

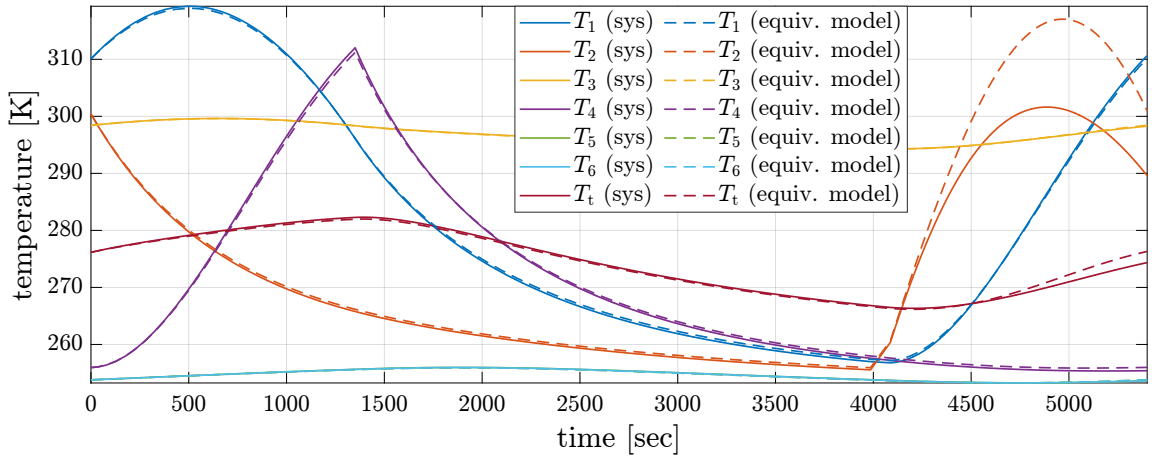


**(b)** Simulation of the models

**Figure 2.8:** The Models' performance in Matlab

DOI:10.15774/PPKE.ITK.2023.002

## 2.7 Conclusion

A thermal mathematical model was constructed and studied to compute the transient temperatures of the CubeSat surface and fuel tank. Several cases were studied using various surface compositions. The obtained results show that the proposed TMM is able to calculate the radiative heat the CubeSat encounters through its assumed orbit. Initially, the CubeSat surface was assumed to be composed of the uncoated aluminum alloy 6061-T6. So far, the corresponding results conclude that the CubeSat surface and fuel tank temperatures would be too high. Therefore, additional finishes applied to the surface were taken into consideration. The first choice of finish was to coat the entire surface of the satellite with magnesium oxide-aluminum oxide paint. The obtained results of the CubeSat show that faces and fuel tank temperatures dropped because of the increased emissivity and decreased absorptivity of its surface. Further simulations were performed of cases in which the faces were exposed to the Sun when partially covered with solar panels. The results indicate that the case described in subsection 2.3.5, which delivers the most electrical power due to the highest percentage of solar panels, still satisfies the temperature limits of the fuel tank and surfaces of the satellite. Moreover, the remodeling of the TMM has been accomplished concerning solar panel ratios $\lambda$, which paves the way to derive the quasi-LPV formulation of the thermal model. The evaluation of the new syntheses was performed, and both models' responses matched sufficiently well. Finally, different $\lambda$ possibilities were presented, illustrating the significant influence of solar panel ratios on the CubeSat dynamic thermal responses. The results also suggest the possibility of installing a fuel tank inside a CubeSat, which could be the first step required to add a propulsion system that can generate thrust for this CubeSat.

DOI:10.15774/PPKE.ITK.2023.002

# Chapter 3

# Thermal control approaches for a CubeSat

## 3.1 Background

As certain electronic and thermodynamic components of the CubeSat were generally designed for terrestrial applications, we require the spacecraft equipment to operate at/around room temperature. Furthermore, at room temperature, it is less expensive and much easier to conduct qualification and flight acceptance testing, as well as equipment development [1]. Due to the payload's varying mass, shape, and distribution, a spacecraft requires strong structural stability, so a thermally-induced distortion must be minimized or rigidly controlled. As a first step, a thermal mathematical model was built in [P1] to analyze the thermal behavior of the CubeSat system equipped with an additional propellant tank placed in the middle of the spacecraft. The possibility to regulate the fuel tank temperature employing PID-based control systems to follow a prescribed constant temperature during the satellite orbital motion was examined in [P4]. For tank temperature control, a nonlinear control design technique is utilized using input/output feedback linearization as proposed in [P5]

The so-called *Model Predictive Control* (MPC) concepts span a fairly wide class of system models. MPC techniques are explicitly formulated for nonlinear models in a quasi-LPV form as in [P2]. It is challenging that the thermal controller design has multiple objectives. Firstly, we have to keep *propellant tank at approximately room temperature* with minimal or no fluctuation. Moreover, the temperature of the CubeSat's surface should not exceed a given upper bound. Secondly, a control signal has to be computed, which can be realized with the onboard heater; namely, it must be non-negative and *not exceed an upper power limit*. On the other hand, we are interested in *maximizing the area* of the solar panel to produce more electrical energy to operate the onboard computer or other (e.g., telecommunication) devices or sensors. Then, it is worth mentioning that the solar panel significantly influences the average/baseline temperature level of each component of the CubeSat object. Therefore, the proportion ($\lambda$) of the solar panel area ($A_{\mathrm{P}} = \lambda\, A$) and the total face area ($A$) are distinguished design parameters in the manufacturing of the CubeSat. Finally, the integrated design of an *optimal* solar panel area and an appropriate control signal, together, provide that the component temperatures fulfill the prescribed technological constraints.

DOI:10.15774/PPKE.ITK.2023.002

The Chapter is organized as follows: Two preliminary PID techniques are presented in section 3.2. Then the dynamic power supplied to the tank employing PID-based approaches is illustrated in section 3.3. Next, the CubeSat tank thermal regulation utilizing a linearization scenario is shown in section 3.4. Also, the tank thermal regulations of the two models are summarized in section 3.4 as a comparison. Finally, an integrated model predictive control design approach is presented in Section 3.5.

## 3.2 PID-based temperature control of CubeSat

The most elementary controller for temperature tracking is a PID, the scheme of which is shown in Figure 3.1. Suppose a linear or linearized mathematical model of the plant is given; in that case, it is possible to apply various PID-based design techniques to determine the controller parameters that will meet the transient and steady-state specifications of the closed-loop system. In order to find the minimum required heat flux, Matlab Simulink models have been implemented to simulate the CubeSat thermal dynamics controlled by PID-based controllers. During the analysis, two different PID strategies were considered. Firstly, the traditional PID control loop is applied with actuator saturation. Then, the control dynamics are supplemented by integral anti-windup feedback of the actuator's error.

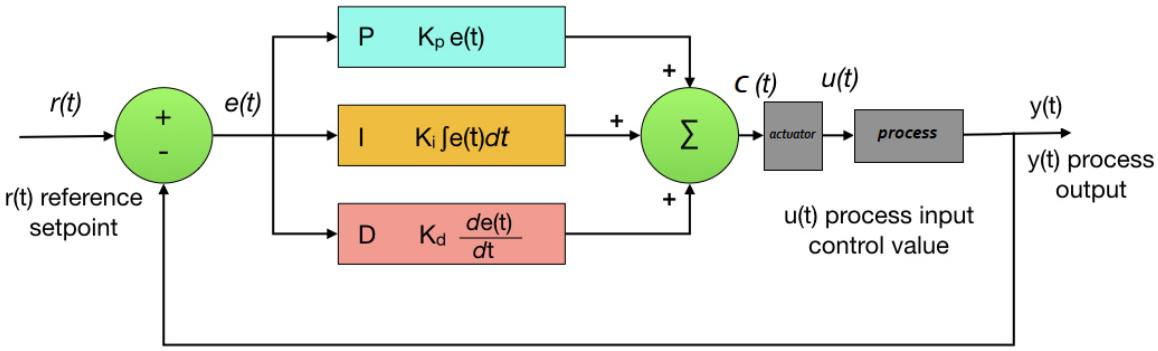


**Figure 3.1:** PID closed-loop control system

### 3.2.1 Process and Actuator

The spacecraft has extensive temperature oscillations caused by the periodically changing environment. Then the CubeSat surface and its fuel tank temperatures through the orbit have large fluctuations due to the Sunlight and the Earth's shadow effects. Since the satellite equipment usually operates efficiently within a narrow temperature range, and most materials have non-zero coefficients of thermal expansion, larger than preferred temperature changes could lead to thermal distortion [1]. Thus, an active control strategy has to be implemented in the CubeSat thermal control system.

DOI:10.15774/PPKE.ITK.2023.002

The thermal mathematical model for the CubeSat surface and its fuel tank, described in section 2.3, was the process simulated by using the Embedded Matlab function with some other components. The actuator is either an actual device by which some specific physical variables are controlled (regulated) or it is a unit that supplies the input (e.g., material flow or power) to the process. The physical control input might be a heater that provides a heating rate to the fuel tank [70]. The heater attached to the fuel tank generates the control signal to produce the additional heat flux $\dot{Q}_c$ along the shady part of the orbit. In this study, the actuator ( *heater*) is assumed to be a device that converts the control signal ($C_s$) into additional heat flux $\dot{Q}_c$ and passes it to the satellite propellant tank as a supplementary heat source, as shown in Figure 3.2.

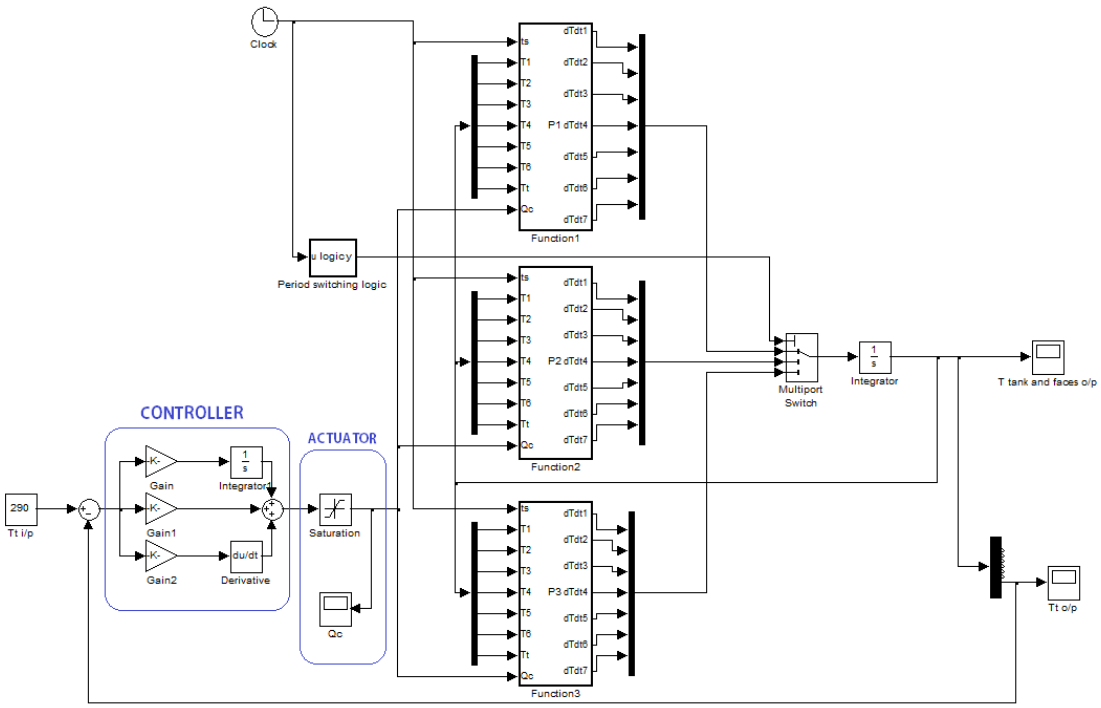


**Figure 3.2:** Simulink model of the initial PID controller

### 3.2.2 Simulations of CubeSat thermal control system

The investigations of the ability to control the satellite propellant tank within the prescribed temperature range were done for the case of the CubeSat being covered by 70% aluminum and 30% solar panels. So $\lambda = 0.3$; namely, 30% portion of the appropriate faces are covered by solar panels. The thermal simulation results in Figure 2.4 show that the transient tank temperature oscillates between 282 K and 266.2 K. If the requirement is to regulate the tank temperature at 290 K, a heater should be attached to the tank during the satellite orbits, which provides the additional heat rate $\dot{Q}_c$ to the fuel tank along with the satellite orbital motion. The elements and structure of the control system are shown in Figure 3.3.

DOI:10.15774/PPKE.ITK.2023.002

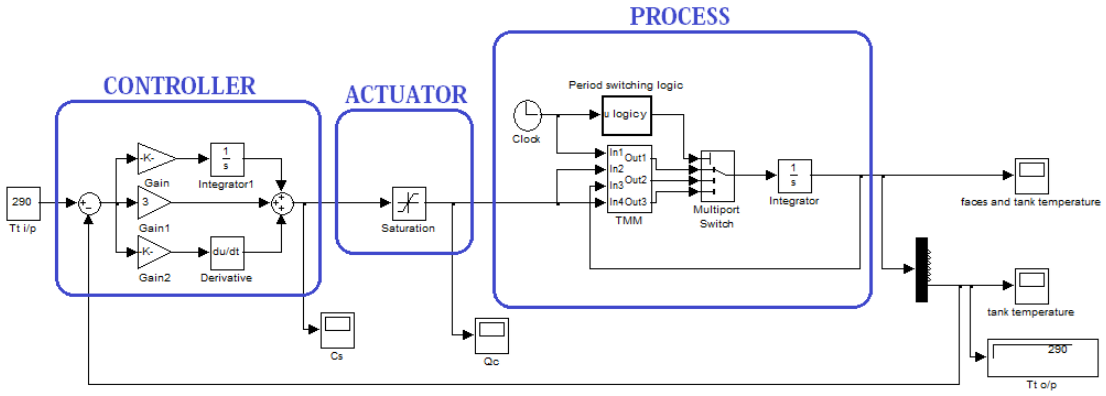


**Figure 3.3:** Structure of controlled system using PID controller

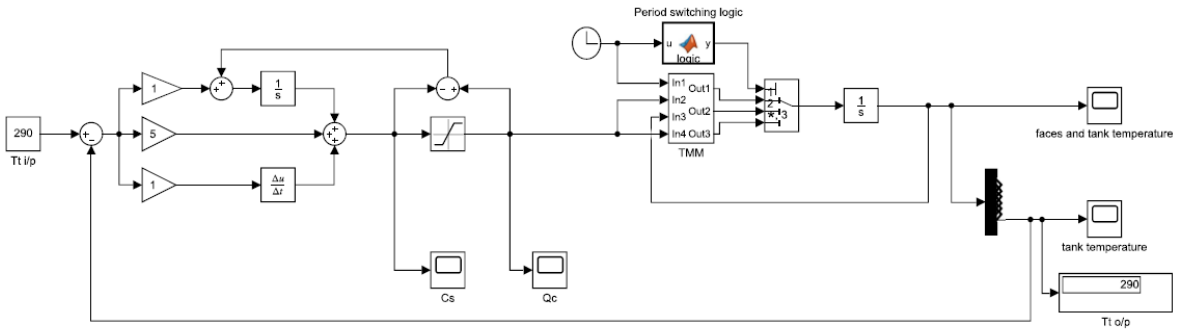


**Figure 3.4:** The PID controller with anti-windup block diagram.

The transparency of the PID control mechanism, the availability of reliable and cost-effective commercial PID modules, and their widespread acceptance by operators are among the reasons for its success. There are many PID tuning methods, each with pros and cons. For instance, *commonly known as rule-based tuning methods*, the Kappa-tau tuning method is an evolution of the Ziegler-Nichols method. This method is designed to overcome the shortcomings of Ziegler-Nichols, such as high proportional gains, but it provides poor results for systems with long normalized dead time. The lambda tuning method is suited only for PI controller tuning, a derivative parameter can not be taken into consideration. The Ziegler–Nichols tuning method is a heuristic method of PID tuning. So far, it is suitable for a stable system, as in our case, and it provides an acceptable time response for our model. Therefore, Ziegler and Nichols's rules were used to set the values of $K_P$, $T_I$, and $T_D$. The obtained controller parameters are $K_P$= 5, $T_I$= 1s and $T_D$= 1s based on experimental step responses. The satellite faces and the fuel tank temperatures have been examined for two orbits, as shown in Figure 3.5.

DOI:10.15774/PPKE.ITK.2023.002

In practice, the heating power is limited to about 1.5 W [71], as shown by the saturation block in the actuator part in Figure 3.3 and the corresponding thermal performance of the fuel tank as presented in Figure 3.5. *Windup* is a phenomenon, caused by interactions between the integral action and saturation. Thus, to improve the control response, an anti-windup scheme was used, as shown in Figure 3.4. Figure 3.6 shows the corresponding controlled fuel tank temperature.

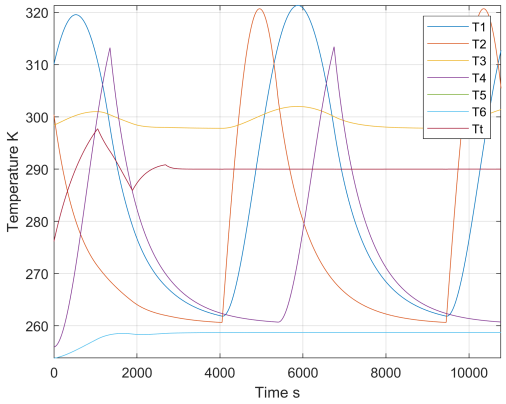


**Figure 3.5:** The satellite surface temperatures and the regulated fuel tank temperature by using a simple PID controller

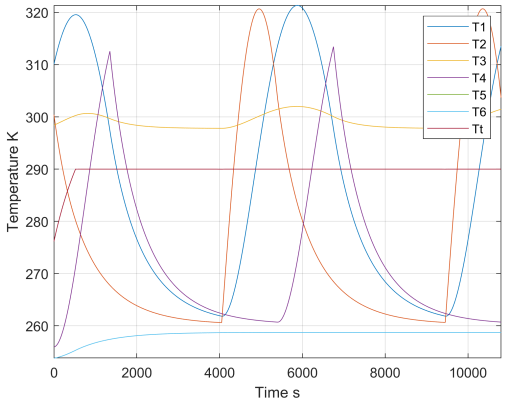


**Figure 3.6:** The satellite surface temperatures and the regulated fuel tank temperature by using a PID controller in the anti-windup scheme

Two PIDs procedures are employed to illustrate the CubeSat tank thermal responses clearly. The satellite fuel tank thermal responses by using the classic PID controller and the PID with anti-windup are shown, respectively in Figure 3.7 (a, and b). It is visible that the initial transient is not acceptable for the simple PID without anti-windup. However, the anti-windup solution satisfies the design specifications with a short settling time and a slight overshoot.

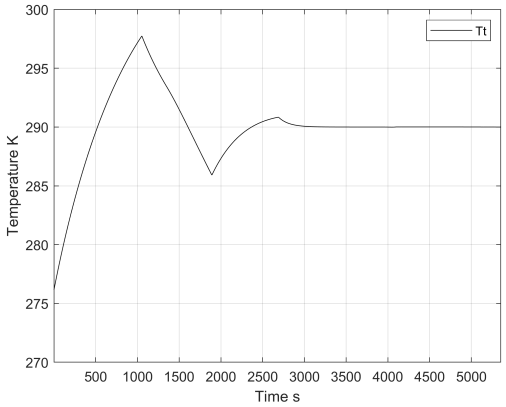


**(a)** Using the PID controller

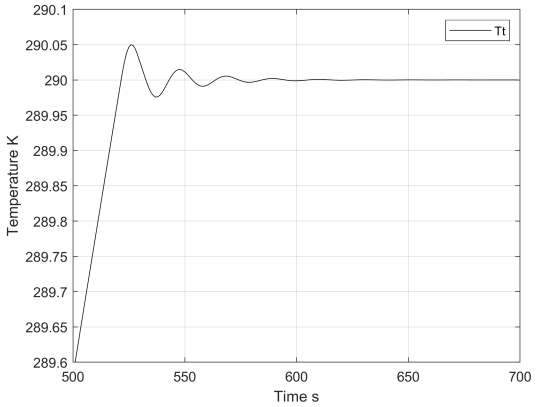


**(b)** Using the PID controller with anti-windup

**Figure 3.7:** The CubeSat's fuel tank thermal response

DOI:10.15774/PPKE.ITK.2023.002

## 3.3 Simulations of different heating power values

The power of an active heater in a small satellite is hardly limited. Hence, it is necessary to determine a minimum power limit at which the detailed PID synthesizes steer the tank temperature at the reference value along the satellite orbits and seek the best responses satisfying the purpose. Therefore, PID-based controllers are designed and simulated to control the satellite propellant tank temperature at 290 K employing manifold heating power limits.

The following simulations are presented for different values of the heating power limits with classic PID and anti-windup PID controllers. Moreover, the same conditions for both control schemes are considered to observe the fuel tank thermal responses among multiple different maximal heat flux values, such as 2, 1.5, 1.3, and 1 W.

- **Fuel tank thermal responses by using a PID controller with different heating power limit values:**

  The thermal behaviors of the PID-controlled fuel tank have been simulated with different values of maximal heating power (2, 1.5, 1.3, and 1 W), as shown respectively in Figure 3.8 (a, b, c, and d).

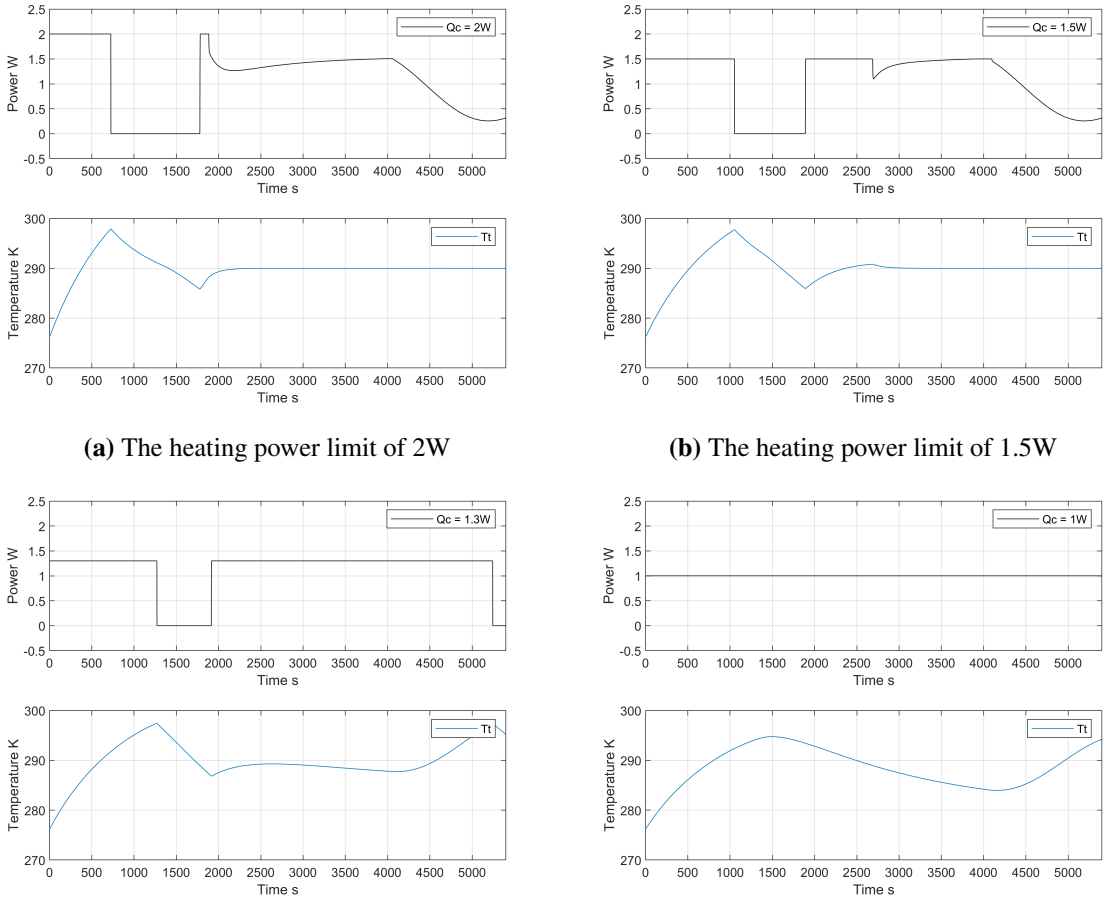


**(a)** The heating power limit of 2W

**(b)** The heating power limit of 1.5W

**(c)** The heating power limit of 1.3W

**(d)** The heating power limit of 1W

**Figure 3.8:** The PID regulated dynamic thermal response of the fuel tank with different heating power limit values of the heater

DOI:10.15774/PPKE.ITK.2023.002

- **Fuel tank thermal responses by using an anti-windup PID controller with different heating power values:**

  The thermal behaviors simulations for the fuel tank have been conducted by applying an anti-windup controller with the following values of the maximal heating power (2, 1.5, 1.3, and 1 W), as shown respectively in Figure 3.9 (a, b, c, and d).

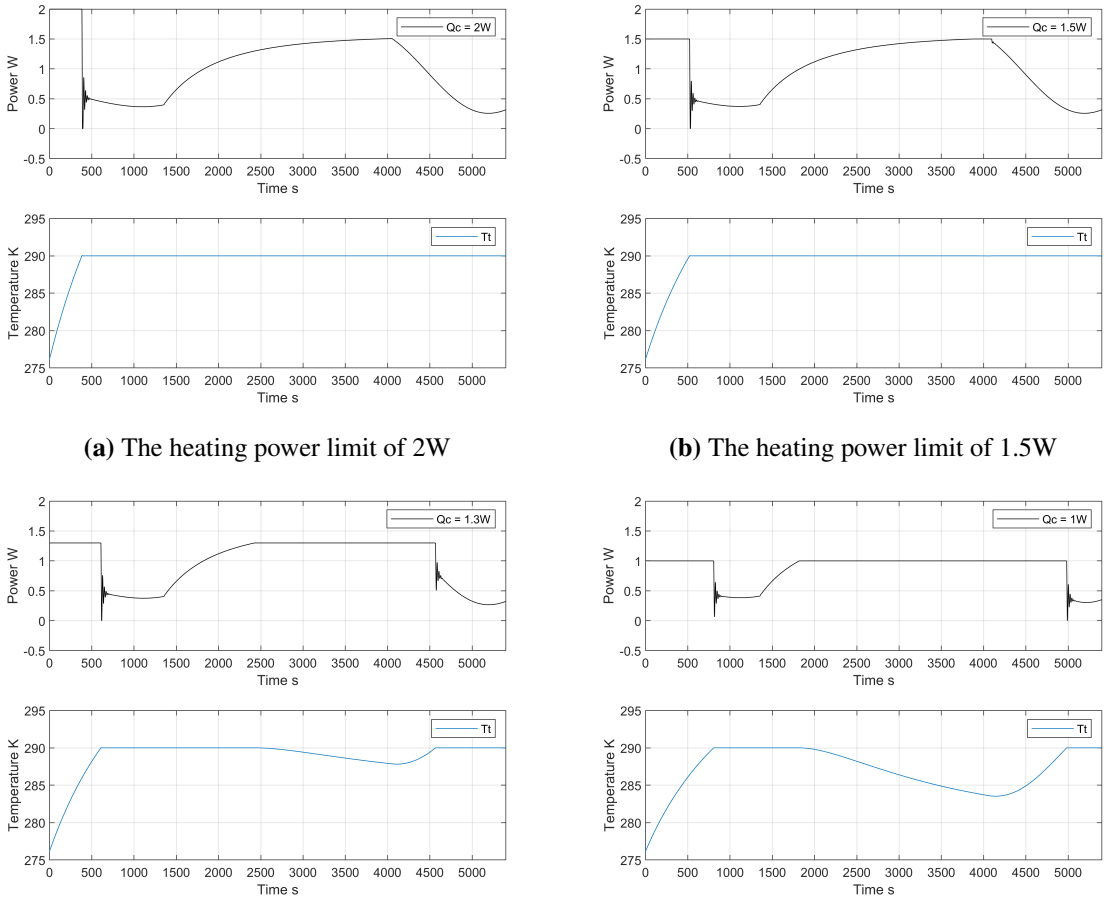


**(a)** The heating power limit of 2W




**(b)** The heating power limit of 1.5W




**(c)** The heating power limit of 1.3W




**(d)** The heating power limit of 1W

**Figure 3.9:** The anti-windup PID regulated dynamic thermal response of the fuel tank with different heating power values of the heater

DOI:10.15774/PPKE.ITK.2023.002

## 3.4 Linearization-based control system

The input/output linearization feedback law is derived using the thermal mathematical model equations from Chapter 2 considering the case of 70% aluminum and 30% solar panels ($\lambda = 0.3$) covering three satellite's faces, which are exposed to the Sun throughout the circular satellite's orbit. Foremost, it is necessary to limit the heat flux passed by the heater to the propellant tank at 1.5 W.

The dynamic equation of the tank's temperature is written as follows:

$$\dot{T}_{\mathrm{t}} = \frac{k_0}{k_{\mathrm{T}}}\left(\sum_{i=1}^{6} T_i^4 - 6T_{\mathrm{t}}^4\right) + \frac{1}{k_{\mathrm{T}}}u, \tag{3.1}$$

To perform a feedback linearization, the following nonlinear input function can be computed:

$$u = k_{\mathrm{T}}e_r - k_0\left(\sum_{i=1}^{6} T_i^4 - 6T_{\mathrm{t}}^4\right), \tag{3.2}$$

where $k_0 = F_{Ft}\ \sigma\ \varepsilon_{\mathrm{IR}}^{\mathrm{Al}}\ \sigma\ A$, and $(k_{\mathrm{T}})$ is a constant which is equal to $(m_{\mathrm{s}}C_p^{\mathrm{s}} + m_g C_v)$; see section 2.4.2, $T_{\mathrm{t}}$ is the fuel tank temperature, $u$ is the input of the nonlinear system, $e_r$ is the error signal, i.e., the difference between the fuel tank reference temperature value $(V_r)$ which is equal to 290 K, and the fuel tank output temperature $T_{\mathrm{t}}$.

Observe that by substituting feedback (3.2) into (3.1) we obtain:

$$\dot{T}_{\mathrm{t}} = e_r. \tag{3.3}$$

The Matlab Simulink model configuration presented in Figure 3.10 is a simple integrator that describes the fuel tank thermal control system via the input-output linearization structure. Figure 3.11 exposes the thermal behavior schemes of the propellant tank and the CubeSat surface. It is clear that the peak power delivered to the tank through the heater is 1.5 W, as presented in Figure 3.12, which satisfies the physical constraints.

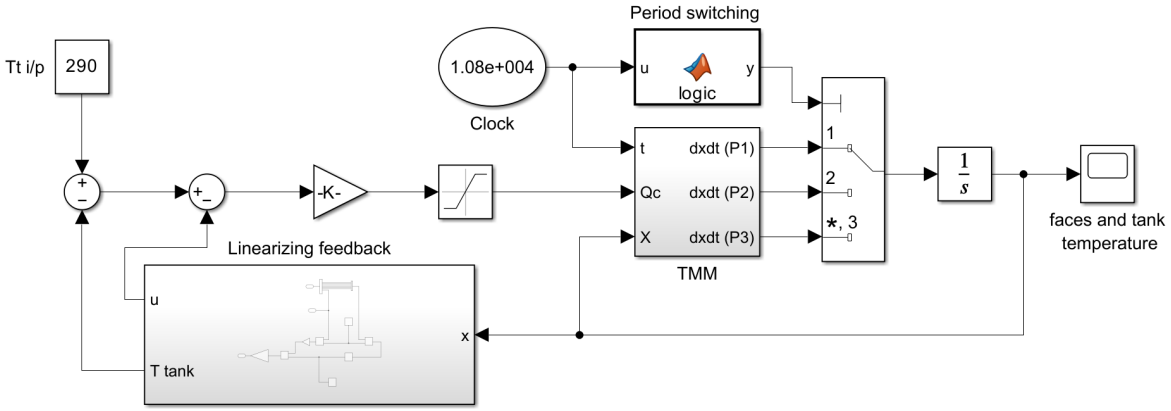


**Figure 3.10:** Input/output linearization control framework in Matlab/Simulink

DOI:10.15774/PPKE.ITK.2023.002

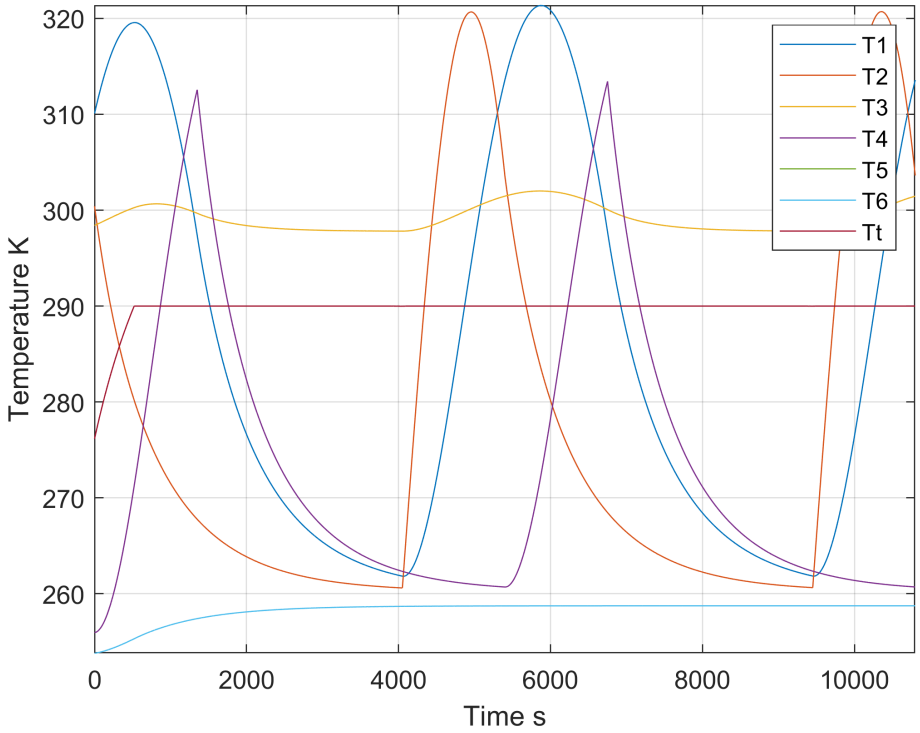


**Figure 3.11:** CubeSat surface and its fuel tank thermal behaviors via linearization-based controller and heating power limited at 1.5 W

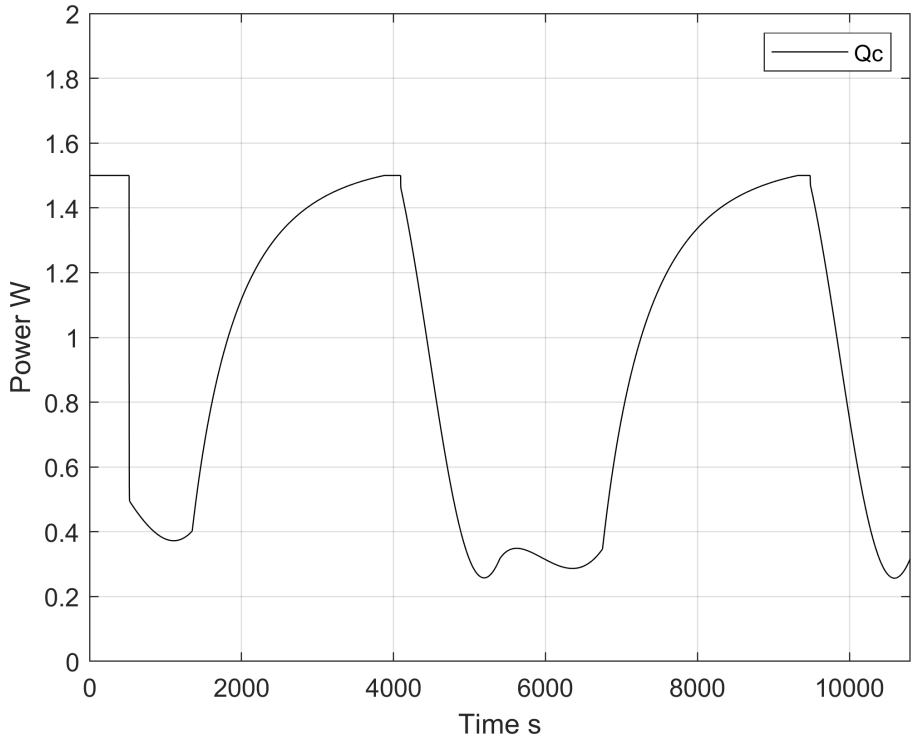


**Figure 3.12:** The essential heat flux to regulate the fuel tank temperature

DOI:10.15774/PPKE.ITK.2023.002

**The simulations of regulated models operate two controlled instances to compare the thermal time responses of the fuel tank.**

The Matlab Simulink model has been employed to analyze the CubeSat surface and the tank's regulated thermal responses for the model in section 2.4 in parallel with the TMM

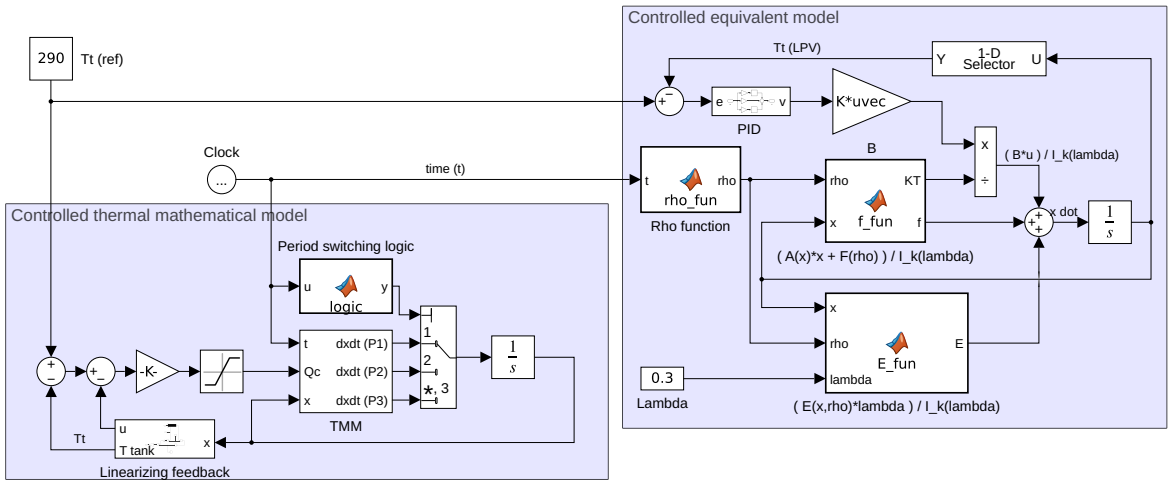


**(a)**

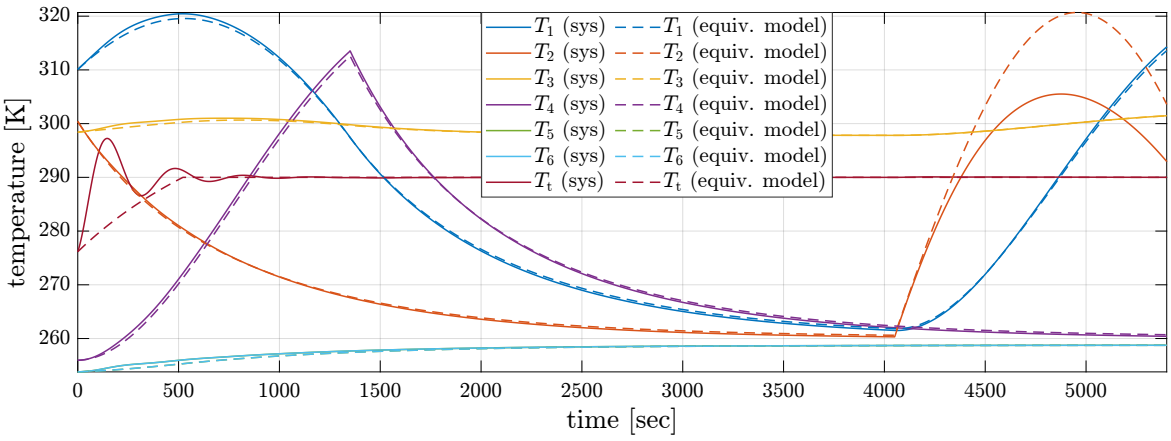


**(b)**

**Figure 3.13:** (a) Matlab/Simulink of the unified model controlled by PID and the original TMM with input-output linearization, (b) Simulation of these two syntheses

In Figure 3.13 (b), the differences between the transit time responses for the fuel tank temperatures of two models come from using two different controller types. For the new model, the PID control system is employed to regulate the fuel tank temperature, so the time response of the fuel tank temperature has a small overshoot[P4]. While for the original TMM, the input-output linearization method is performed to control the tank temperature; thus, the time response of the tank temperature has no overshoot; see [P5]. In addition, this Figure demonstrates that the two models track the fuel tank reference temperature with identical steady-state responses despite being subjected to different control syntheses.

DOI:10.15774/PPKE.ITK.2023.002

## 3.5 Integrated control design and parameter computation using MPC

In this section, we present a simultaneous design for both a feasible control input signal ($\dot{Q}_c$) and an optimal solar panel area ($\lambda\ A$). To model and solve nonlinear MPC optimization problems we used Matlab's Model Predictive Control Toolbox [55] (MPC-Toolbox), which is based on [45] and on the works (e.g., [72]) collected in [46].

### 3.5.1 Nonlinear MPC design

In this subsection, we present in brief the MPC optimization problem based on [72]. We consider a continuous-time nonlinear system as

$$\dot{x}(t) = f(x(t), u(t), \rho(t)), \tag{3.4}$$

where $x$ is the state vector, $u$ is the input or the manipulated variable, and $\rho$ is a known disturbance signal. We assume that the present and future values of $\rho$ are both available. It is realistic in the case of a CubeSat when the orbit of the device is precisely known.

Note that the MPC is a discrete-time controller, therefore, a sampled model of (3.4) is considered by the MPC-Toolbox [55, Pg. 10.4] by using the implicit trapezoidal method (i.e., the Tustin approximation) with a constant sampling period ($h$).

Additionally, we consider a zero-order hold on the manipulated variable $u$ (i.e., $u$ is designed in the form of a staircase function). On the other hand, we assume that the known disturbance $\rho$ is a piecewise affine function, namely:

$$\begin{aligned} &u(t) = u(t_k), \text{ for all } t \in [t_k, t_{k+1}), \text{ and} \\ &\rho(t) \approx \rho(t_k) + \frac{t - t_k}{h}(\rho(t_{k+1}) - \rho(t_k)), \text{ for all } t \in [t_k, t_{k+1}), \end{aligned} \tag{3.5}$$

where $t_k = k \cdot h$ for any integer number $k$. Then, the Tustin approximation of (3.4) simplifies to

$$\begin{aligned} x(t_{k+1}) \approx x(t_k) + \frac{h}{2}\Big( &f\big(x(t_k), u(t_k), \rho(t_k)\big) + \\ &+ f\big(x(t_{k+1}), u(t_k), \rho(t_{k+1})\big)\Big). \end{aligned} \tag{3.6}$$

Let $\hat{x}(t_{k+i}|t_k)$, $i = 1, \ldots, N$ denote the value of the state at time $t_{k+i}$ *predicted* at the $k$th time step $t_k$ using the discrete-time approximation (3.6) in the knowledge of $x(t_k)$, $\rho(t_k)$, $\ldots$, $\rho(t_{k+i})$ and for some input. Similarly, let $u(t_{k+i}|t_k)$, $i = 0, \ldots, N-1$ denote the value of the input at time $t_{k+i}$ *computed* at the $k$th time step $t_k$. Integer number $N$ constitutes the so-called *prediction horizon* of the MPC problem. Then, the MPC input design at time $t_k$ can be formulated as follows.

DOI:10.15774/PPKE.ITK.2023.002

***Problem 1*** *(General MPC design).* Consider a dynamical system (3.4). Assume that the values of $x(t_k)$, $\rho(t_k)$, ..., $\rho(t_{k+N})$ are available at time $t_k$. Compute $\hat{x}(t_{k+i}|t_k)$, $i = 1,\dots,N$ and $u(t_{k+i}|t_k)$, $i = 0,\dots,N-1$, which minimize a cost function

$$J\big(\hat{x}(t_{k+1}|t_k),\dots,\hat{x}(t_{k+N}|t_k),\hat{u}(t_k|t_k),\dots,u(t_{k+N-1}|t_k)\big), \tag{3.7}$$

and satisfy the following equality constraints (prediction model):

$$\begin{cases} \hat{x}(t_{k+i+1}|t_k) = \hat{x}(t_{k+i}|t_k) + \\ \quad + \dfrac{h}{2}\Big(f\big(\hat{x}(t_{k+i}|t_k),u(t_{k+i}|t_k),\rho(t_{k+i})\big) + \\ \qquad + f\big(\hat{x}(t_{k+i+1}|t_k),u(t_{k+i}|t_k),\rho(t_{k+i+1})\big)\Big), \\ \hat{x}(t_k|t_k) = x(t_k). \end{cases} \tag{3.8}$$

We are allowed to enforce additional custom constraints on the designed input and the predicted state values, e.g., we can prescribe bounds for the state:

$$\underline{x} \le x(t_{k+i}|t_k) \le \overline{x} \text{ for all } i = 1,\dots,N, \tag{3.9a}$$

or the rate of the input can also be bounded

$$\underline{v} \le u(t_{k+i}|t_k) - u(t_{k+i-1}|t_k) \le \overline{v} \text{ for all } i = 1,\dots,N-1, \tag{3.9b}$$

or, e.g., the input can be set constant on the prediction horizon ($u(t_{k+i}|t_k) = u(t_k|t_k)$ for all $i = 1,\dots,N-1$). $\triangle$

Note that in Problem 1, both the predicted state $\hat{x}(t_{k+i}|t_k)$, $i = 1,\dots,N$ and the "planned" input $u(t_{k+i}|t_k)$, $i = 0,\dots,N-1$ are considered as *free decision variables*, and they are meant to be found such that both the prediction model (3.8) and the prescribed control goals (e.g., (3.9)) are satisfied.

In a typical MPC design, a sequence of input values are computed *on-line* in each time-step $t_k$ for a typically short prediction horizon (e.g., $N = 10$), and only the first computed input value $u(t_k|t_k)$ is applied to the system for all $t \in [t_k, t_{k+1})$. Then, a new computation is performed at $t_{k+1}$ in the knowledge of the already measured new state value $x(t_{k+1})$, and again only $u(t_{k+1}|t_{k+1})$ is applied to the system on the next sampling interval $t \in [t_{k+1}, t_{k+2})$. Note that the on-line MPC design is applicable in real time only if the processing time of the MPC optimization is less than the sampling period ($h$).

### 3.5.2 Optimal solar panel area computation

In this section, we propose an *off-line* MPC optimization to compute the optimal solar panel area. Differently from the on-line MPC, we compute a sequence of input values only at time step $k = 0$ and we consider a larger prediction horizon (e.g., $N = 40$, 60 or 100), which covers two consecutive orbital periods. Roughly speaking, after computing $\lambda$ with an off-line MPC, we are ready to manufacture the satellite and control the temperatures by using, e.g., a PID controller or an on-line MPC. Note that our primary aim is to obtain an optimal/feasible $\lambda$, rather than to control the system, therefore, an on-line MPC design is not addressed for the thermal model of the CubeSat system.

Due to the fact that an optimal control sequence is computed only in $t_0$ ($k = 0$), the term "$|t_0$" is omitted from the arguments of $\hat{x}$ and $u$. The off-line MPC problem for the optimal $\lambda$ computation is summarized as follows.

DOI:10.15774/PPKE.ITK.2023.002

***Problem 2*** *(Optimal $\lambda$ computation).* Consider a dynamical system (3.4), with

$$\begin{aligned} &x : [0,\infty) \to \mathbb{R}^7,\ x_j(t) = T_j(t), j = 1,\dots,6,\ x_7(t) = T_{\mathrm{t}}(t),\\ &u : [0,\infty) \to \mathbb{R}^2,\ u_1(t) = \dot{Q}_{\mathrm{c}}(t),\ u_2(t) = u_\lambda(t),\\ &\rho : [0,\infty) \to \mathbb{R}^3. \end{aligned} \tag{3.10}$$

Assume that the values of $x(t_0)$, $\rho(t_0)$, …, $\rho(t_N)$ are available at time $t_0 = 0$. Compute $\hat{x}(t_i)$, $i = 1,\dots,N$ and $u(t_i)$, $i = 0,\dots,N-1$, which minimize the cost function

$$J\big(u(t_0)\big) = 1 - u_2(t_0), \tag{3.11}$$

satisfy the difference equation

$$\begin{cases} \hat{x}(t_{i+1}) = \hat{x}(t_i) + \dfrac{h}{2}\Big(f\big(\hat{x}(t_i), u(t_i), \rho(t_i)\big) + \\ \qquad\qquad + f\big(\hat{x}(t_{i+1}), u(t_i), \rho(t_{i+1})\big)\Big), \\ \hat{x}(t_0) = x(t_0), \end{cases} \tag{3.12}$$

and satisfy the following additional constraints

$$\begin{aligned} &1.\ \hat{x}_7(t_i) \in [\underline{T_{\mathrm{t}}}, \overline{T_{\mathrm{t}}}] \text{ for all } i = k_{(\mathrm{start})},\dots,N,\\ &2.\ \hat{x}_j(t_i) \le \overline{T_{\mathrm{F}}} \text{ for all } j = 1,\dots,6 \text{ and all } i = 1,\dots,N,\\ &3.\ u_1(t_i) \in [0, \overline{u}] \text{ for all } i = 1,\dots,N-1,\\ &4.\ u_2(t_i) = u_2(t_0)\ (= \lambda) \text{ for all } i = 1,\dots,N-1,\\ &5.\ u_2(t_0) \in [0,1], \end{aligned} \tag{3.13}$$

where $\underline{T_{\mathrm{t}}}$, $\overline{T_{\mathrm{t}}}$, $\overline{T_{\mathrm{F}}}$, $\overline{u}$ and the integer number $k_{(\mathrm{start})}$ are constant scalar values given a priori. $\triangle$

Note that the quasi-LPV model formulation in (2.18) of the thermal model does not fit into the model class (3.4) required by the MPC design, as the "input" $\lambda$ appears on both sides of (2.18). Therefore, we consider the following relaxed quasi-LPV model:

$$\begin{aligned} \dot{x}(t) = I_k^{-1}(\lambda^*)\Big(&A(x(t))x(t) + Bu_1(t) + \\ &+ E(x(t),\rho(t))u_2(t) + F(\rho(t))\Big), \end{aligned} \tag{3.14}$$

where $u(t) = \begin{pmatrix} \dot{Q}_{\mathrm{c}}(t) \\ \lambda \end{pmatrix}$ and the parameter $\lambda^*$ is assumed to be known before the optimization. Note that dynamics (3.14) are equivalent to (2.17) if and only if $\lambda^* = \lambda$.

To find an optimal value for $\lambda$, we iteratively approximate $\lambda^* \approx \lambda$ as follows. Consider an initial value $\lambda^*_{(0)}$ for $\lambda^*$. In the $\kappa$th iteration, we perform the MPC optimization described in Problem 2 for $\lambda^* = \lambda^*_{(\kappa)}$. If the resulting optimal value for $\lambda = u_\lambda(t_0)$ is not "close enough" to $\lambda^*_{(\kappa)}$ (e.g., $|\lambda - \lambda^*_{(\kappa)}| > \varepsilon_\lambda$), we perform again the optimization with $\lambda^*_{(\kappa+1)} = \lambda$.

### 3.5.3 Numerical simulations and results

The computations presented in this section were processed on a laptop with an Intel Core i7-4710MQ CPU at 2.50 GHz and 16 GB of RAM.

During the analysis, we considered six different case studies with different sampling rates ($h$), and control objectives ($\underline{T_{\mathrm{t}}}$, $\overline{T_{\mathrm{t}}}$, $\overline{u}$, $k_{(\mathrm{start})}$), but with a common value for $\overline{T_{\mathrm{F}}} = 370$K, and $\lambda^*_{(0)} = 0.5$ with $\varepsilon_\lambda = 0.0005$. In each case study, the MPC design is performed over two orbital periods with sampling rate $h = \frac{2P}{N}$. As presented in Section 3.5.1, the input is searched

DOI:10.15774/PPKE.ITK.2023.002

in the form of a piecewise constant function during the optimization, whereas, the external known disturbance function is assumed to be a piecewise linear function in time. After the optimization, the thermal model in (2.18) of the CubeSat system is simulated with the computed control input sequence $u_1(t_i)$, $i = 0,\dots,N-1$ and the optimal $\lambda$ with the assumption that the input is *piecewise linear* between the computed discrete values $u(t_i)$, namely:

$$\begin{aligned} \bar{u}_1(t) = u_1(t_i) + \frac{t-t_i}{h}(u_1(t_{i+1}) - u_1(t_i)), \\ \text{for all } t \in [t_i, t_{i+1}), \\ i = 0,\dots,N-1. \end{aligned} \tag{3.15a}$$

Differently from the MPC optimization, the simulation is performed on four consecutive orbital periods. Therefore, the control input sequence for the second orbital period computed through the MPC optimization is periodically extended in the simulation for the next two consecutive orbital periods, namely:

$$\bar{u}_1(t) = \bar{u}_1\big(t-(\ell-1)P\big), \text{ for all } t \in [\ell P, (\ell+1)P), \ell = 2,3. \tag{3.15b}$$

Let $\bar{x}(t_i)$ denote the simulated state at time $t_i$ of the state-space model (2.17) driven by the computed input signal $\bar{u}(t)$ in (3.15). In order to quantify the prediction error of the MPC design with respect to the simulated time evaluation of the tank temperature, we compute the following two error quantities:

$$\begin{aligned} \text{MSE}: &\ \tfrac{1}{N}\textstyle\sum_{i=1}^{N}(\hat{x}_7(t_i) - \bar{x}_7(t_i))^2, \\ \text{abs. err.}: &\ \max_{i=1,\dots,N}|\hat{x}_7(t_i) - \bar{x}_7(t_i)|. \end{aligned} \tag{3.16}$$

The abbreviation MSE designates the mean squared error between the predicted and simulated values of the tank temperature at the discrete-time points $t_i$, $i = 1,\dots,N$. Whereas, the absolute error (abs. err.) is the maximal absolute values of the difference between the predicted and simulated value of the tank temperature at the discrete-time points over the prediction horizon.

The MPC optimization results for the six different case studies are presented in details in Figures 3.14-3.19, respectively. Each of Figures 3.14-3.19 contains six subplots (A)-(F), which illustrate the following results: subplot (A) presents the optimal staircase control input sequence $u_1(t_i) = \dot{Q}_{\mathrm{c}}(t_i)$, $i = 0,\dots,N-1$, computed through the MPC optimization; subplot (B) shows the predicted values of the tank temperature at $t_0,\dots,t_N$ (blue dotted line), and the interval constraint on $T_{\mathrm{t}}(t_i) \in [\underline{T_{\mathrm{t}}}, \overline{T_{\mathrm{t}}}]$ for all $i = k_{(\mathrm{start})},\dots,N$ (red region); subplot (C) illustrates the predicted values $T_j(t_i)$ of the surface temperatures at $t_0,\dots,t_N$, and $j = 1,\dots,6$; subplot (D) illustrates the interpolated piecewise affine input function (3.15) considered in the simulations; in Subplot (E), the simulated time evaluation of the tank temperature is compared against the predicted time series of the tank temperature through the mean squared and absolute prediction errors (3.16); subplot (F) illustrates the simulated time evaluation of the surface temperatures.

The presented data in subplots (A)-(C) are computed through the MPC optimization, and they span two orbital periods. The data in (D)-(F) present the simulation results of the thermal model (2.17) driven by the input (3.15).

DOI:10.15774/PPKE.ITK.2023.002

In Figure 3.14, we present the first case study. We designed an optimal value for the solar panel area and a controller sequence to keep the tank temperature around 290 K. If we allow higher fluctuation $T_{\mathrm{t}}(t_i) \in [287, 293]$ K, $i = 3, \ldots, N$, ($N = 40$, $h = 270$s), but require a low power control signal ($\overline{u} = 1.2$ W), we obtain $\lambda \simeq 0.51$. In the second case study (Figure 3.15), we restricted the tank temperature to a tighter interval $T_{\mathrm{t}}(t_i) \in [289, 291]$ K. The optimization points out that the solar panel ratio should be decreased to $\lambda = 0.4481$, at the same time, the applicable heating power limit should be increased to $\overline{u} = 1.4$ W (Figure 3.15). It is worth remarking that the control objectives are more conservative in this case compared to the first case study. Therefore, we considered a shorter sampling period $h = 180$s ($N = 60$). Observing the results of the first two control design setups, we can conclude that smaller temperature fluctuations can be achieved if the solar panel area is small enough and the actuator has a higher power limit to be able to provide the necessary heat flux during the shady parts of the orbit.

In the next two cases, our major objective is to analyze the precision and complexity of the proposed optimization method for two different sampling periods. In these computations, the baseline tank temperature was raised to 300 K, and we allowed $\pm 3$ K fluctuation (namely, $\underline{T_{\mathrm{t}}} = 297$ K, and $\overline{T_{\mathrm{t}}} = 303$ K). First, we considered a longer sampling period $h = 270$s ($N = 40$), secondly, we used a shorter one $h = 108$s ($N = 100$). In both cases, one feasible power bound for the heater was $\overline{u} = 1.75$ W. As Figures 3.16 and 3.17 illustrate, a shorter sampling period may result in a more precise prediction model (3.12). Obviously, the undershoot and overshoot from the allowed (red) region are lower if a shorter sampling period is selected. Unfortunately, the computational complexity of the optimization increases combinatorially as we consider a longer prediction horizon (i.e., a larger $N = \frac{2P}{h}$).

From the authors experience, the bound conditions for the surface temperatures ($\hat{x}_j(t_i) \leq 370$ K for all $i = 1, \ldots, N$, and all $j = 1, 6$) are trivially satisfied in the previous four cases (Figures 3.14-3.17). Therefore, this constraint is removed from the optimization to reduce its computational complexity.

Another pair of interesting experiments is illustrated in Figures 3.18 and 3.19. Let us relax the upper bound for the CubeSat's surface and tank temperature $\overline{T_{\mathrm{F}}} = \overline{T_{\mathrm{t}}} = \infty$. (In the numerical computations we consider finite but "large enough" value for $\overline{T_{\mathrm{t}}} = 330$ K.) Using MPC, we can find the lowest feasible upper bound $\overline{u}$ for the input power, such that the heater can maintain the tank's temperature above $\underline{T_{\mathrm{t}}}$. The optimization was performed in two different cases for $\underline{T_{\mathrm{t}}} = 290$ K and $\underline{T_{\mathrm{t}}} = 297$ K. Through the optimization, we concluded that the CubeSat's appropriate faces should be completely covered by solar panels ($\lambda = 1$), and the minimum required upper bound for the thermal flux should be $\overline{u} = 1.069$ and $\overline{u} = 1.545$, respectively. However, we have seen in the previous syntheses that, in the real-world scenario, $\lambda = 1$ is not a feasible value for solar panel coverage. In this case, the parts of the satellite will be overheated, and we are not able to give a control input sequence that keeps the faces and the tank temperature below the prescribed values, i.e., the optimization is infeasible with the criteria $\hat{x}_j(t_i) \leq 370$ K for all $i = 1, \ldots, N$, and all $j = 1, 6$.

Although the on-line MPC design is planned as future work, we remark that the dynamics of the CubeSat's thermal system are relatively slow, therefore, the processing time of the "off-line" MPC can be easily kept much below the sampling period. From the second case study (Figure 3.15, we have found that for a relatively large prediction horizon ($N = 60$) the optimization can still be executed (comfortably) within a single sampling period.

DOI:10.15774/PPKE.ITK.2023.002

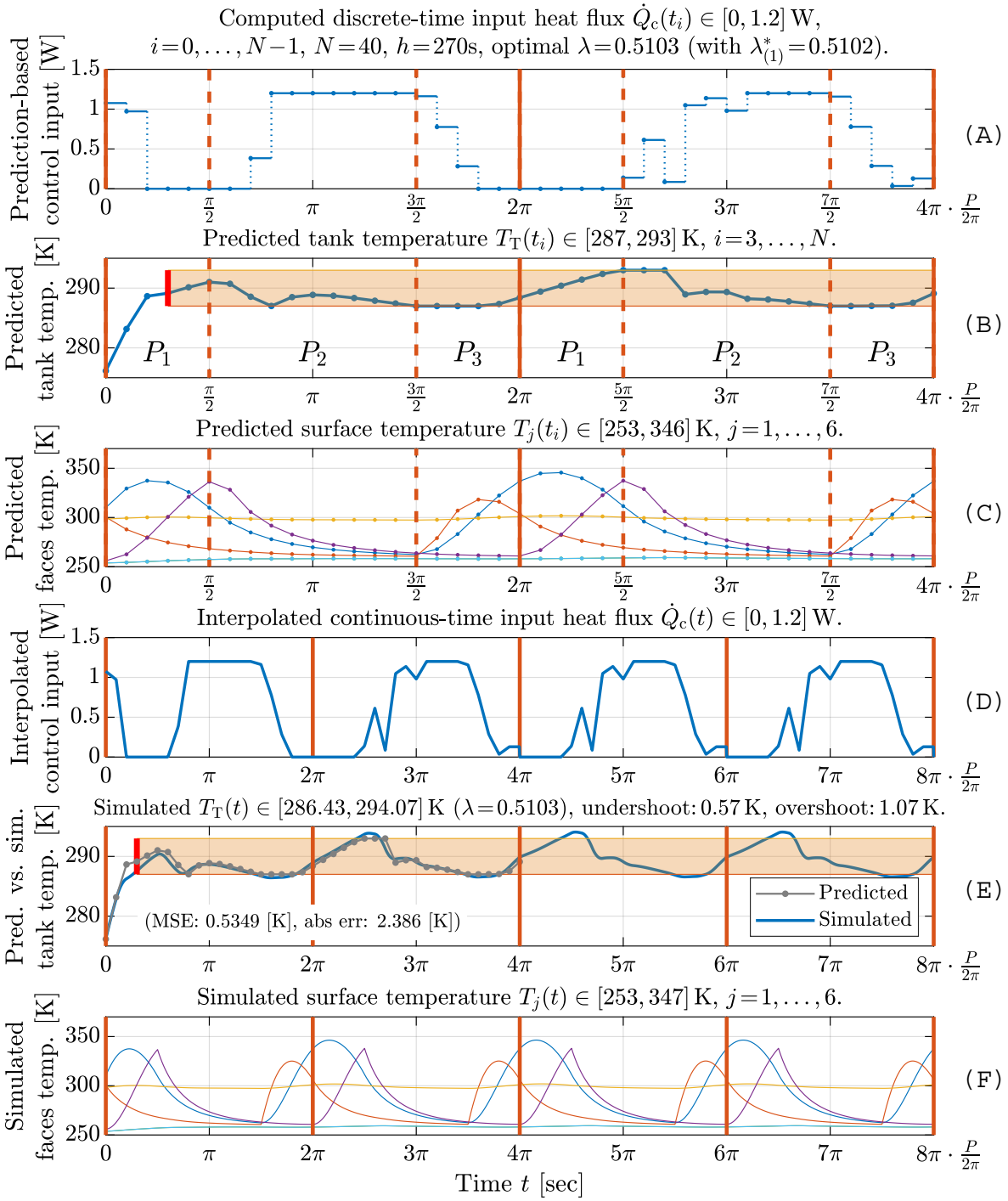


**Figure 3.14:** Low power ($\dot{Q}_c \leq 1.2$ W) MPC design allowing higher ($\pm 3$ K) fluctuation around $T_t = 290$ K with $h = 270$s, $N = 40$. The final value of $\lambda^*$ was obtained through two iterations: $\lambda^*_{(0)} = 0.5$, $\lambda^*_{(1)} = 0.5102$. The processing time of the MPC optimization was less than 15 seconds. The constraints (3.12) and (3.13) were tested less than 500 times during the optimization

DOI:10.15774/PPKE.ITK.2023.002

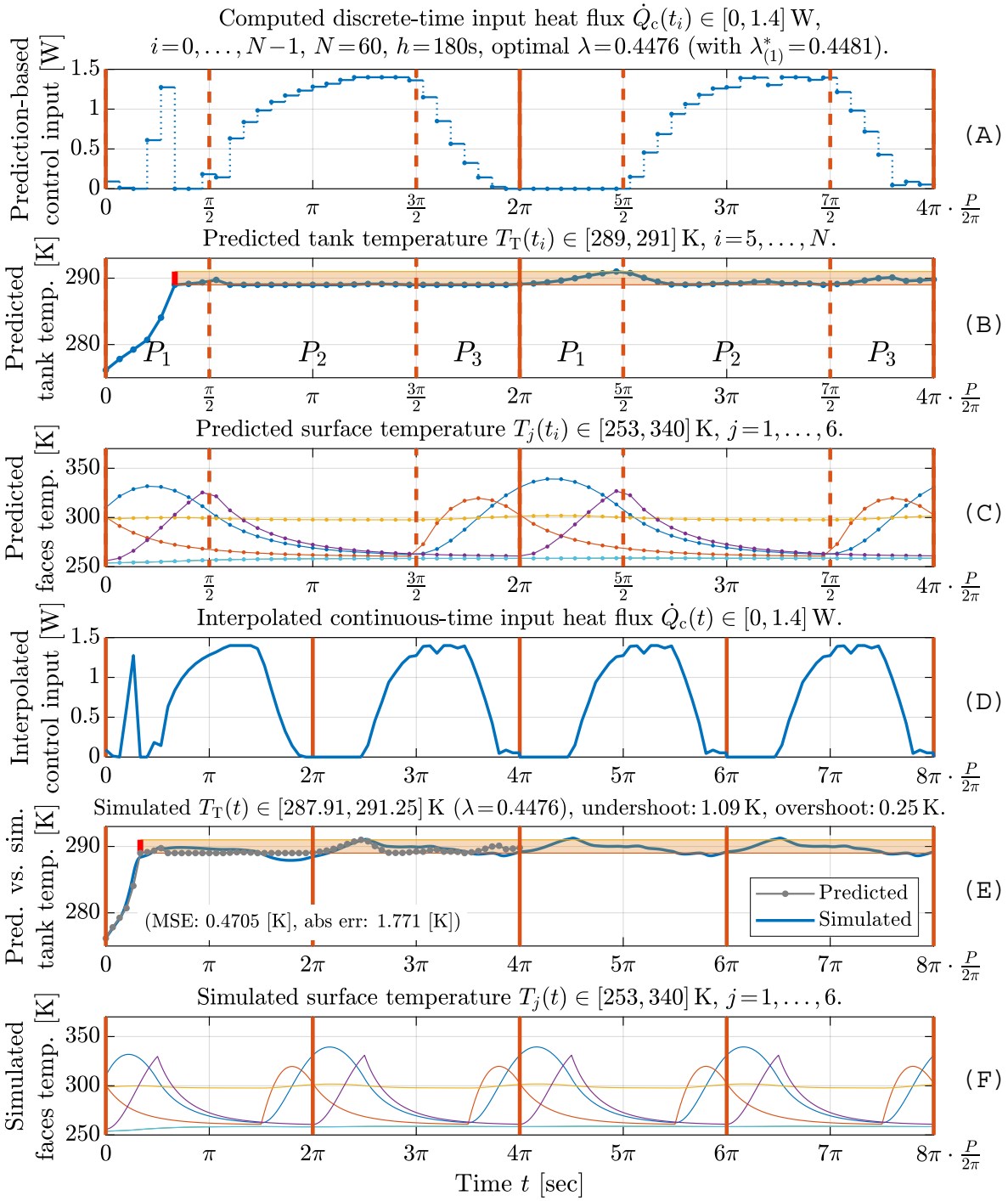


**Figure 3.15:** Medium power ($\dot{Q}_c \leq 1.4$ W) MPC design allowing smaller ($\pm 1$ K) fluctuation around $T_t = 290$ K with $h = 180$s, $N = 60$. The final value of $\lambda^*$ was obtained through two iterations: $\lambda^*_{(0)} = 0.5$, $\lambda^*_{(1)} = 0.4481$. The processing time of the MPC optimization was less than 40 seconds. The constraints (3.12) and (3.13) were tested less than 750 times during the optimization

DOI:10.15774/PPKE.ITK.2023.002

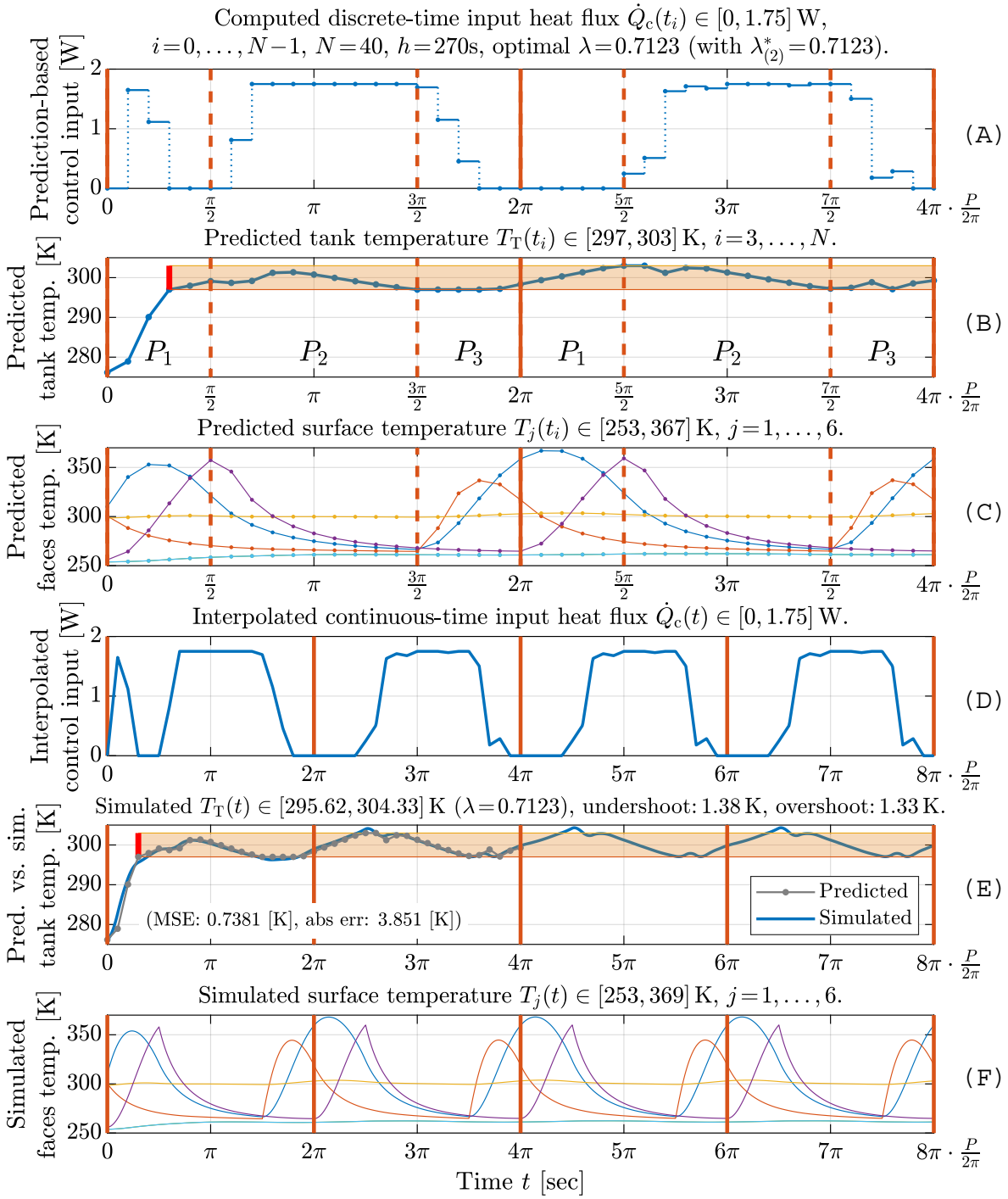


**Figure 3.16:** High power ($\dot{Q}_c \leq 1.75$ W) MPC design enforcing a higher baseline tank temperature ($T_t = 300$ K) but allowing higher ($\pm 3$ K) fluctuation ($h = 270$s, $N = 40$). The final value of $\lambda^*$ was obtained through three iterations: $\lambda^*_{(0)} = 0.5$, $\lambda^*_{(1)} = 0.7095$, $\lambda^*_{(2)} = 0.7123$. The processing time of the MPC optimization was less then 15 seconds. The constraints (3.12) and (3.13) were tested less than 550 times during the optimization

DOI:10.15774/PPKE.ITK.2023.002

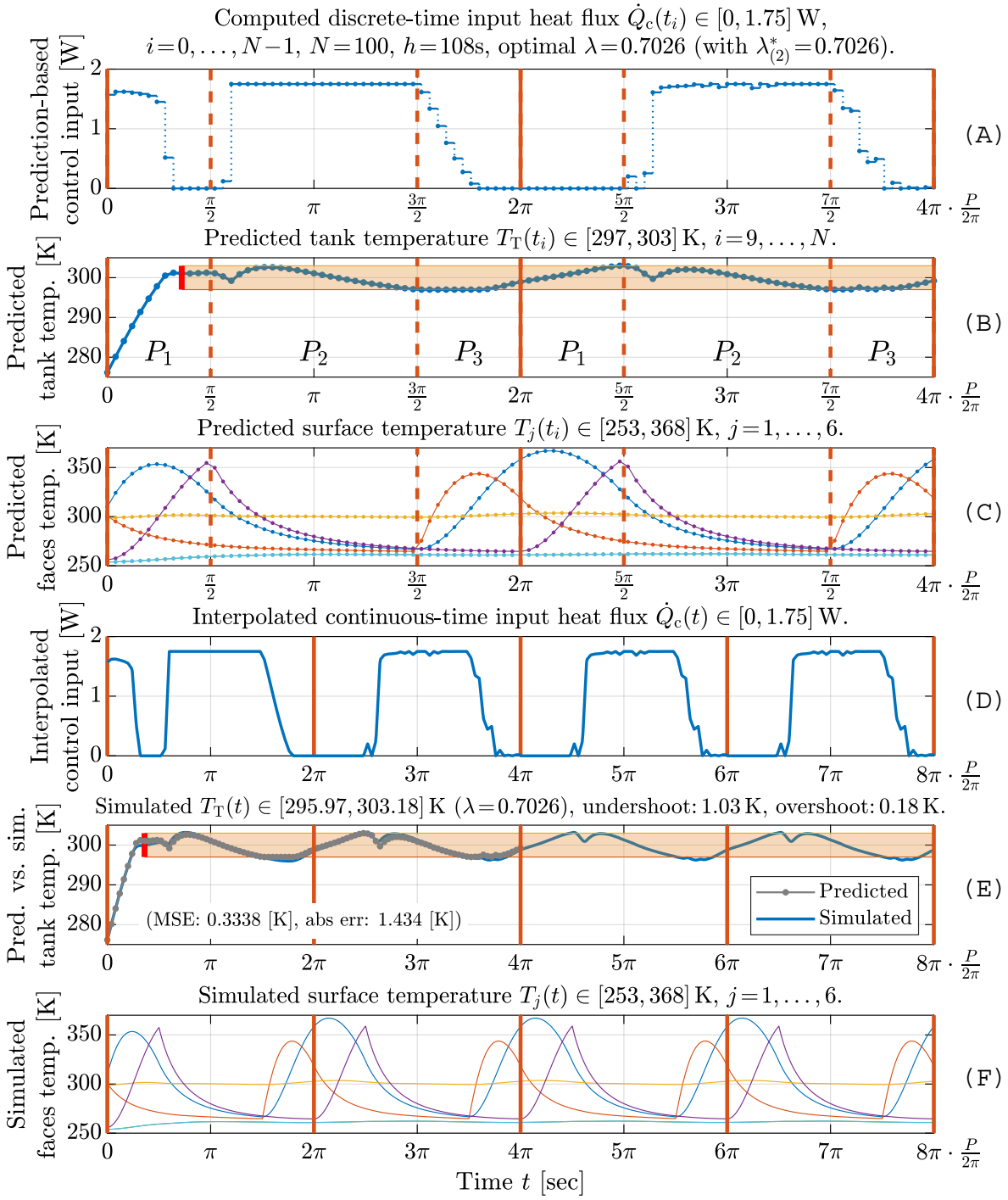


**Figure 3.17:** High power ($\dot{Q}_c \leq 1.75$ W) MPC design enforcing a higher baseline tank temperature ($T_t = 300$ K) but allowing higher ($\pm 3$ K) fluctuation ($h = 108$s, $N = 100$). The final value of $\lambda^*$ was obtained through three iterations: $\lambda^*_{(0)} = 0.5$, $\lambda^*_{(1)} = 0.7$, $\lambda^*_{(2)} = 0.7026$. The processing time of the MPC optimization was less than 200 seconds. The constraints (3.12) and (3.13) were tested less than 650 times during the optimization

DOI:10.15774/PPKE.ITK.2023.002

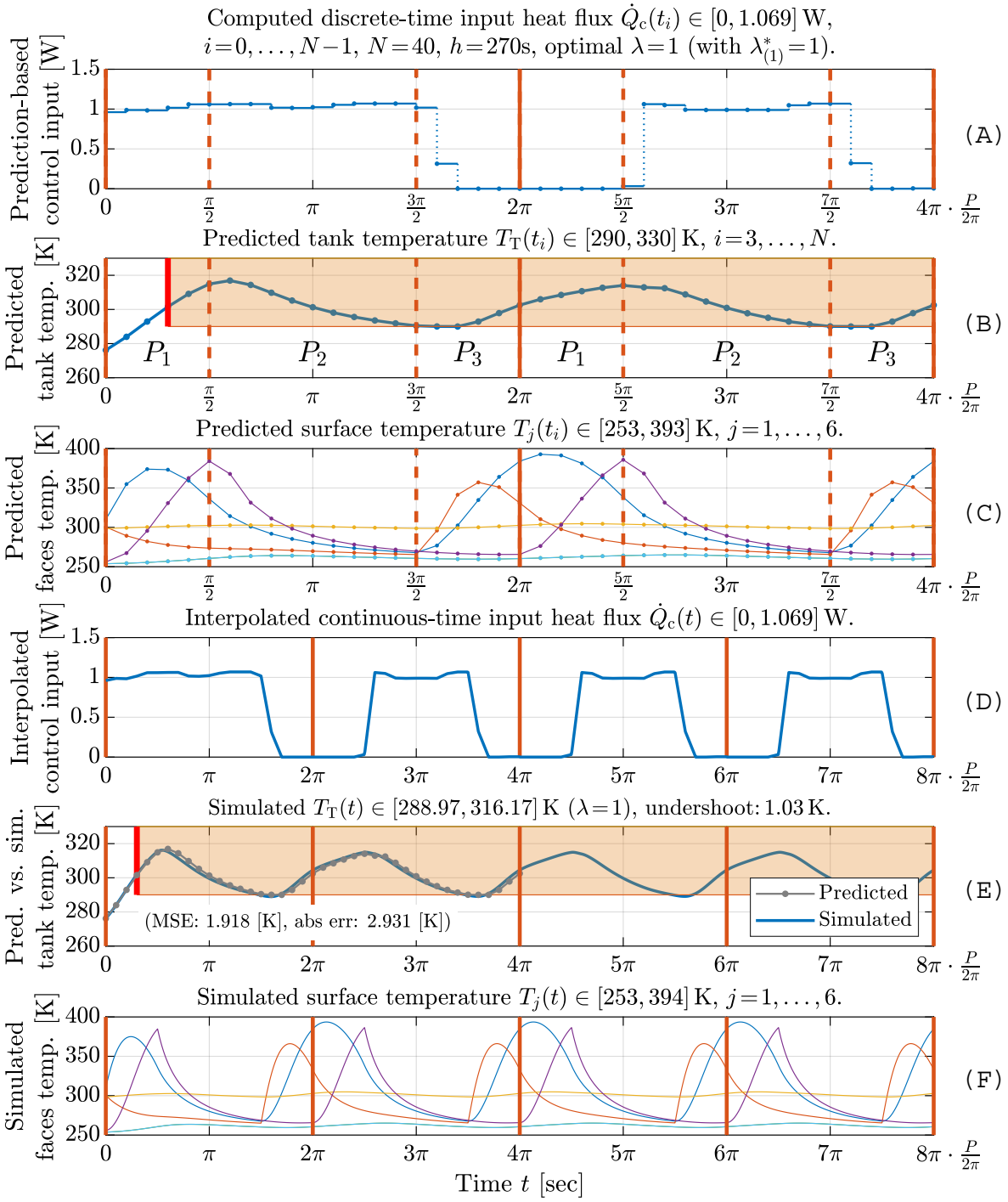


**Figure 3.18:** Minimum thermal flux required to keep the tank's temperature above 290 K if $\lambda = 1$ (i.e., the appropriate faces of the CubeSat are fully covered by the solar panel). The sampling period is $h = 270$s, the prediction horizon is $N = 40$. The final value of $\lambda^*$ was obtained through two iterations: $\lambda^*_{(0)} = 0.5$, $\lambda^*_{(1)} = 1$. The processing time of the MPC optimization was less than 1 second. The constraints (3.12) and (3.13) were tested 30 times during the optimization

DOI:10.15774/PPKE.ITK.2023.002

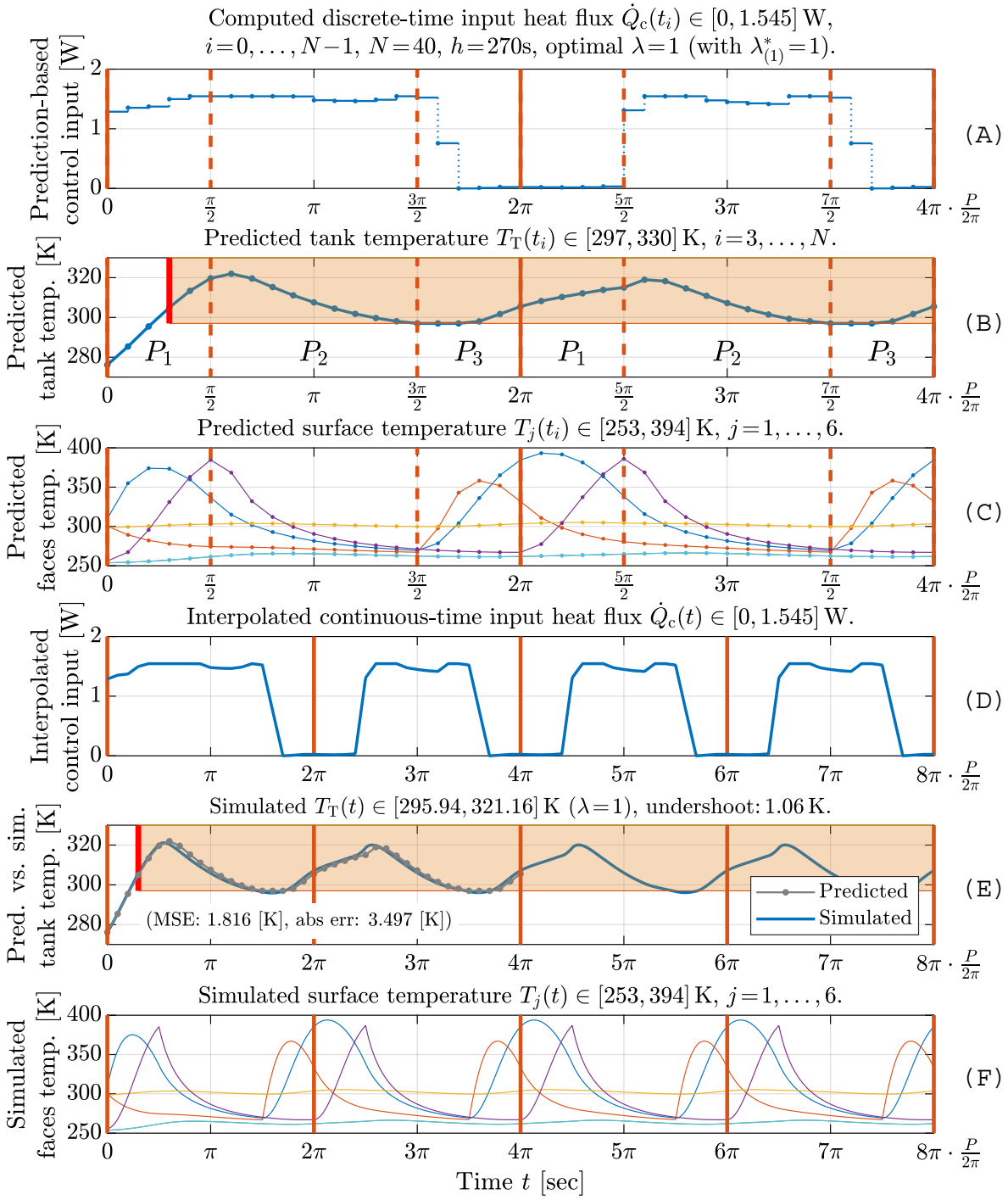


**Figure 3.19:** Minimum thermal flux required to keep the tank's temperature above 297 K if $\lambda = 1$ (i.e., the appropriate faces of the CubeSat are fully covered by the solar panel). The sampling period is $h = 270$s, the prediction horizon is $N = 40$. The final value of $\lambda^*$ was obtained through two iterations: $\lambda^*_{(0)} = 0.5$, $\lambda^*_{(1)} = 1$. The processing time of the MPC optimization was less than 1 second. The constraints (3.12) and (3.13) were tested 12 times during the optimization

DOI:10.15774/PPKE.ITK.2023.002

## 3.6 Conclusion

In this Chapter, control approaches for the thermal system of an orbiting CubeSat were presented. During its orbital motion, the satellite flies along the Sunny and shady sides of the Earth. Thus, periodic fluctuations can be observed in the thermal dynamics of the different components of the CubeSat. To maintain the tank temperature within an acceptable range, a passive control approach was presented in Chapter 2 by manipulating the surface coating of the CubeSat and the power dissipated heat flux of the onboard electrical devices. Differently from Chapter 2, four distinct control design techniques to track a given reference tank temperature were simulated by considering multiple input saturation levels and solar panel coverage. Furthermore, simultaneous designs for passive and active control were presented for selecting an optimal area for the solar panels *(*passive control) and computing a feasible heat flux signal *(*active control). First, the area of the solar panels has been fixed to simulate the CubeSat tank thermal responses under PID-based control techniques, and different heater power saturation levels have been tested in the classical PID controller scheme with an anti-windup compensation. Then, a feedback linearization technique was applied to achieve reference tracking. These new theoretical and computational results open up new avenues for manufacturing and operating CubeSat in order to meet technological thermal constraints. The simulation results show that the minimum heating power to achieve the prescribed control goals is about 1.5 W. Moreover, the results clearly show that the thermal response of the fuel tank, *corresponding to the anti-windup PID controller*, is more advantageous because of the faster rising time and almost no overshoot. Finally, an optimization-based model-predictive approach was demonstrated to simultaneously design an optimal solar panel ratio and a feasible control input sequence. The results show that an off-line model-predictive analysis is particularly useful for assessing the physical limits of the control. It is especially true for nonlinear models, where the available analysis and control design techniques are more limited than the results for linear time-invariant systems.

DOI:10.15774/PPKE.ITK.2023.002

# Chapter 4

# Unmanned aerial vehicle navigation using GNSS/INS integration

## 4.1 Background

Satellite navigation is challenging in critical places, mainly because of the signal blockage problem. As a result, satellite systems are frequently integrated with inertial navigation systems, which compensate for each other. In other words, regarding advantages and drawbacks during the application, the Inertial Navigation System (INS) and the Global Navigation Satellite System (GNSS) are two types of common navigation equipment. Therefore, the INS/GNSS integrated navigation system is a reasonably constructed system that is vastly employed in aviation, aerospace, and sailing [13].

This Chapter proposes a K-Nearest Neighbor (KNN) predictor algorithm to predict signals between sampling instants of GNSS receiver data based on actual GNSS data attributes. The KNN method uses the database to search for data similar to the current data. Thus, the obtained data are the so-called nearest neighbors of the existing data [73]. The integration of INS/GNSS with a Kalman filter into ultra-tightly coupled synthesis is then proposed. The Kalman filter's measurement update establishes a connection between the states and measurements. So, a link between GNSS measurements, In-Phase (I) and Quadrature (Q) signals, and INS data, location, velocity, and attitude, is formed in an ultra-tightly integrated system. Thus, ultra-tightly is not a direct coupling technique as loosely, and tightly coupled systems [74]. Then, a comprehensive software was constructed in the Matlab environment to carry out the analysis. The algorithms' main idea is that KNN predicts new GNSS data points based on k training samples, which correspond to the measured GNSS data, and then the output of the predictor is integrated with the INS data.

The results show that the KNN predicts precisely the signs localized between the GNSS sampling points and that integrating GNSS/INS provides satisfying performance, especially with a short period of GNSS data loss.

The Chapter is organized as follows: The collecting and processing of the experimental data are presented respectively in sections 4.2, and 4.3. Then, the modulation technique specifying how to satisfy the GNSS/INS integration is proposed in section 4.4. Lastly, in section 4.5 the results of simulations according to different scenarios that concern variations in GNSS data blocking time are displayed.

DOI:10.15774/PPKE.ITK.2023.002

## 4.2 Experimental data records

The whole system is tested on data recorded with an actual flying drone. The logs were produced when a video recording campaign was run at the Mátyásföld, *(144m Above Mean Sea Level (AMSL), 47.4992 N, 19.1977 E)*, model airfield near Budapest [75]. Mátyásföld airfield was a commercial, public airfield at the beginning of the 20th century, which also served as the main airport of Budapest before Budaörs airport was built [76; 77]. Nowadays, it is only used for recreational purposes, as it is the home of the *MMBK SE, RC* model aircraft club [78]. As shown in Figure 4.1, the airfield has a maintained runway for RC planes and a fixed table to carry out minor fixes or setup of the model planes. It is one of the locations where scientific experiments [79] took place before introducing the new drone regulation in Hungary in 2021.

An Inertial Measurement Unit (IMU), such as the ArduCopter's [80], is made up of at least three accelerometers that measure the three-axis gravity vectors and two gyros that measure rotation around the tilt and pitch axes in airborne vehicles. The Attitude Heading Reference System (AHRS) is an IMU plus the code to decrypt the output from its sensors to identify the position and heading of airborne vehicles. Both are insufficient on their own since gyros drift over time and accelerometers are inaccurate over short periods of movement time. To develop an AHRS, the data from both types of sensors must be integrated into the software to ascertain the actual aircraft attitude and motion. The Kalman filter is one method for accomplishing this. Autopilots, which combine a CPU and sensors in one device, have now supplanted them.

The data were recorded with a 3DR Iris+ [81] drone running the ArduCopter firmware. During the experiments, the AHRS_GPS_GAIN parameter was set to 1, which means that the AHRS took into account GNSS measurements as well to flatten out disturbances in IMU sensor measurements. 3DR Iris+ was a commercially available product of the 3D Robotics company, and it is an RC-controlled quadcopter with the PixHawk flight control computer [82]. The maximum flight time is around 20 minutes with the 5100 mAh battery. The aircraft can carry a payload of a maximum of 450g.

In the original experiment [75], the Iris+ was programmed to fly automatically along with the predefined waypoints and carried a 2-axis Tarot gimbal with a GoPro camera; see Figure 4.2. In addition, the Iris+ has a UBlox GPS + Compass Module [83] and two IMU modules composed of two sets of accelerometers and gyroscopes to track the aircraft's position. The precision of the tracking changes with the number of satellites seen by the GPS antenna, but in general, the accuracy is enough to run automatic flights; it is typically within a 1m radius.

## 4.3 Converting geographic coordinate system to ECEF coordinate system

The Earth's Figure depicts geographic (*geodetic*) coordinates, commonly known as meridians and latitude lines. So, geodetic coordinates are determined on the surface of a reference ellipsoid, which characterizes the Earth's shape. Meridians pass across the north and south poles of the planet, intersecting at right angles with the latitudes. Except for the equator, the latitudes are not great circles, meaning their centers are not the same as the Earth's center. The altitude of a location is also considered, along with the geodetic coordinates of a point. The

DOI:10.15774/PPKE.ITK.2023.002

**Figure 4.1:** Mátyásföld airfield top view image [78], the red box shows the location of the model runway, the table, and the parking area for cars; the green box indicates the helipad.

**Figure 4.2:** 3DR Iris+ aircraft with Tarot Gimbal and GoPro camera [84]

*Earth-Centered Earth-Fixed* (ECEF) coordinate frame is the Cartesian coordinate frame used in satellite navigation systems. ECEF employs three-dimensional (X, Y, and Z) coordinates (in meters) to describe the position of an object. The expression *Earth-Center* refers to the fact that the origin of the axis (0, 0, 0) is at the mass center of gravity (as determined by years of satellite tracking). The term *Earth-Fixed* refers to the fact that these axes are fixed to the Earth (i.e., they rotate with the Earth); see Figure 4.3.

The obtained data was in LLA geodetic coordinates; while the subsequent calculations are required, the data is in ECEF cartesian coordinates. Thus, Matlab was used for converting the geographic coordinates into the ECEF coordinates. Then, Figure 4.4 represents the 3D trajectory of the moving drone in LLA coordinates, and Figure 4.5 denotes the 3D trajectory of the moving drone in ECEF coordinates. Finally, to illustrate the data recorded in the experiment, we zoom in on the drone's altitude in both coordinates, as presented in Figure 4.6. It is demonstrated that the INS signals recorded in ECEF coordinates are not much smoother than signals in LLA coordinates, but the differences in the coordinate scales are significant.

DOI:10.15774/PPKE.ITK.2023.002

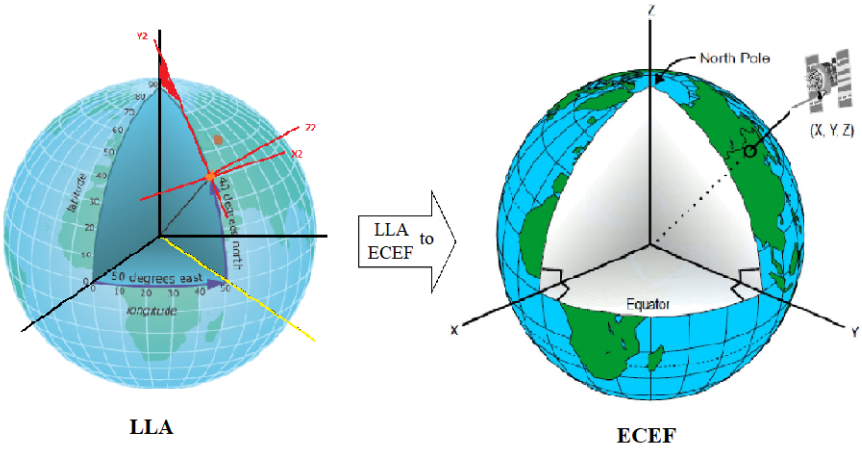


**Figure 4.3:** LLA and ECEF coordinate systems

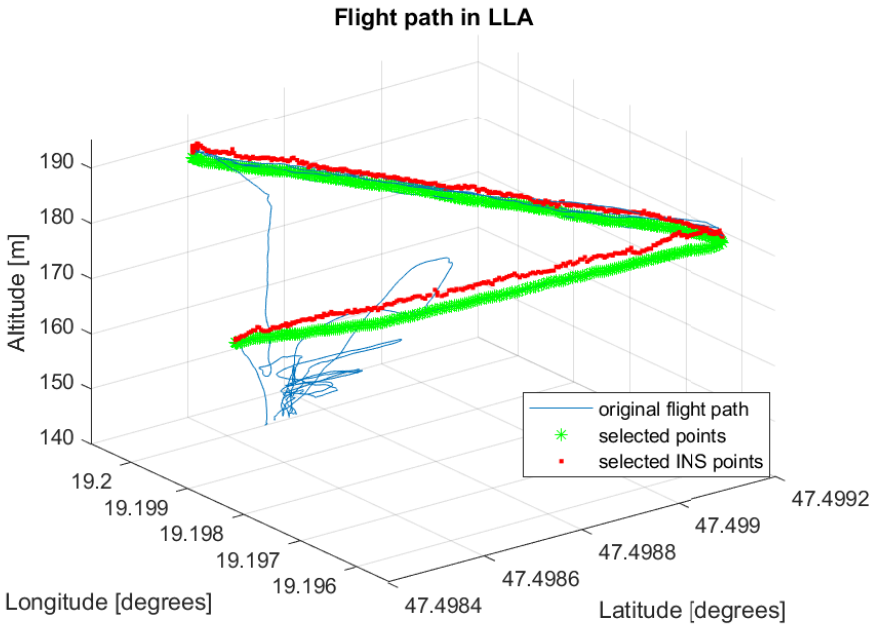


**Figure 4.4:** LLA of The 3D trajectory of the moving drone

DOI:10.15774/PPKE.ITK.2023.002

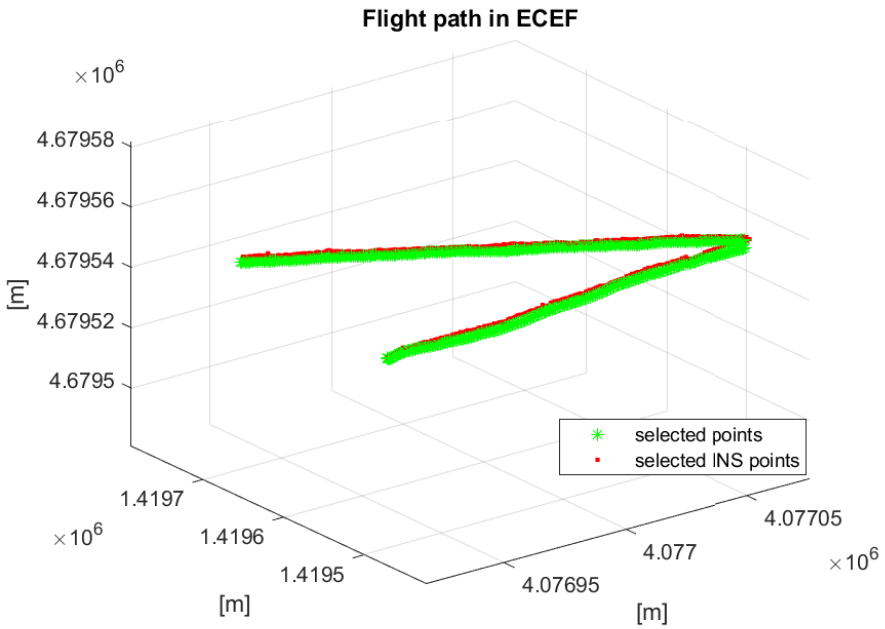


**Figure 4.5:** ECEF of the 3D trajectory of the moving drone

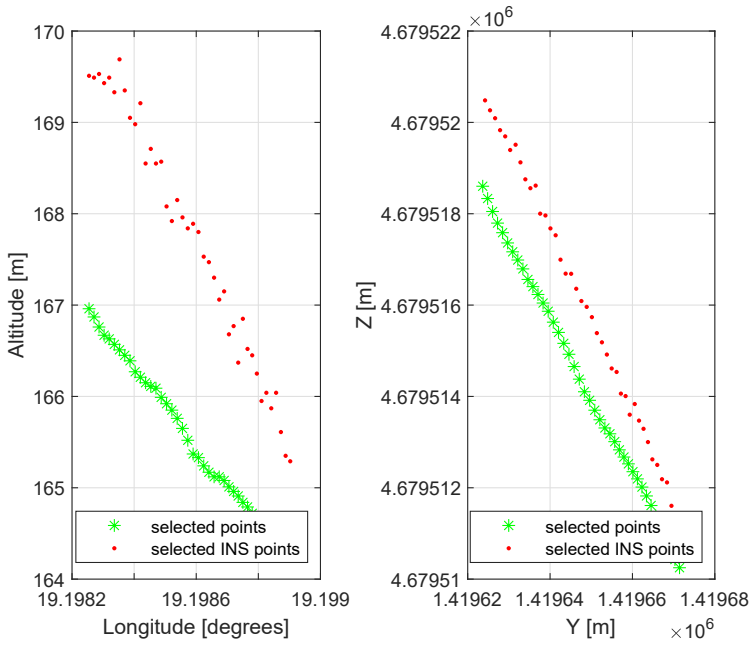


**Figure 4.6:** ECEF and LLA altitude trajectory of the moving drone

DOI:10.15774/PPKE.ITK.2023.002

## 4.4 Modulation of GNSS/INS integration

GNSS/INS integration's main idea is to use the position information measured by GNSS to correct the INS drift errors[64].

The K-Nearest Neighbor (KNN) algorithm belongs to the supervised learning category and is used for classification and regression. It is also a universal algorithm for filling in missing values and resampling datasets. The name (*K-nearest neighbor*) means considering k nearest data points to predict the new data point. Thus, the KNN predictor algorithm is used at the GNSS receiver's output to predict between GNSS instant samples' data for synchronization purposes with INS [85; 86].

### 4.4.1 K-nearest neighbor predictor algorithm

For neighborhood classification, a KNN algorithm variant is used. In the case of KNN, when the k parameter is selected, various dataset properties need to be considered. As a result, the classification performance is better with a higher k-value because of the effect of noise reduction, but at the same time, the classes will be closer to each other. Thus, the boundaries between the classes are less clear. So, a KNN is a supervised learning algorithm where the training samples determine the classification rules without additional parameters [73].

In other words, the K-Nearest Neighbor (KNN) principle is to locate k entities from the training data that are closest to the data being tested. The KNN algorithm is relatively straightforward; it works by determining the K-nearest neighbor from the testing data to the training data and then using the majority of KNN to predict the testing data. Hence, this algorithm aims to predict new GNSS data based on actual GNSS data characteristics. The position information is provided at 1 Hz by the GNSS receiver. However, the system which integrates GNSS and INS measurements (see Figure 4.7) needs the information at 10 Hz. To fulfill this requirement, the predictor will estimate nine new data points at every measured point (for example, for a GNSS measurement at t = 6 sec, the predictor provides data for t = 6.1, 6.2, … 6.9 sec). If the GNSS receiver is blocked, the predictor will produce estimates for a few seconds. The predictor needs four data points to produce the estimates. For example, at t = 6.1 sec, these four preceding points are used to estimate: t = 5.7, 5.8, 5.9, and 6 sec.

Since KNN predictions are based on the axiomatic assumption that objects close in distance are practically similar, it makes sense to distinguish between the K-nearest neighbors when making predictions, that is giving the closest points among the K-nearest neighbors more influence over the search point's outcome. This can be accomplished by introducing a series of weights $\omega$, one for each nearest neighbor, defined by their relative proximity to the inquiry site. As a result, KNN is one of the methods utilized in classification approaches to predict output variables. The dataset is separated into training and testing data in the classification process. KNN compares the given testing data to the training data using a similarity measure. The Euclidean distance between real GNSS data (testing data ($x_{\text{test}}$)), and training data ($x_{\text{train}}$) is used in K-nearest neighbor to compare the given testing data to training data, as shown in equation (4.1) [87]:

DOI:10.15774/PPKE.ITK.2023.002

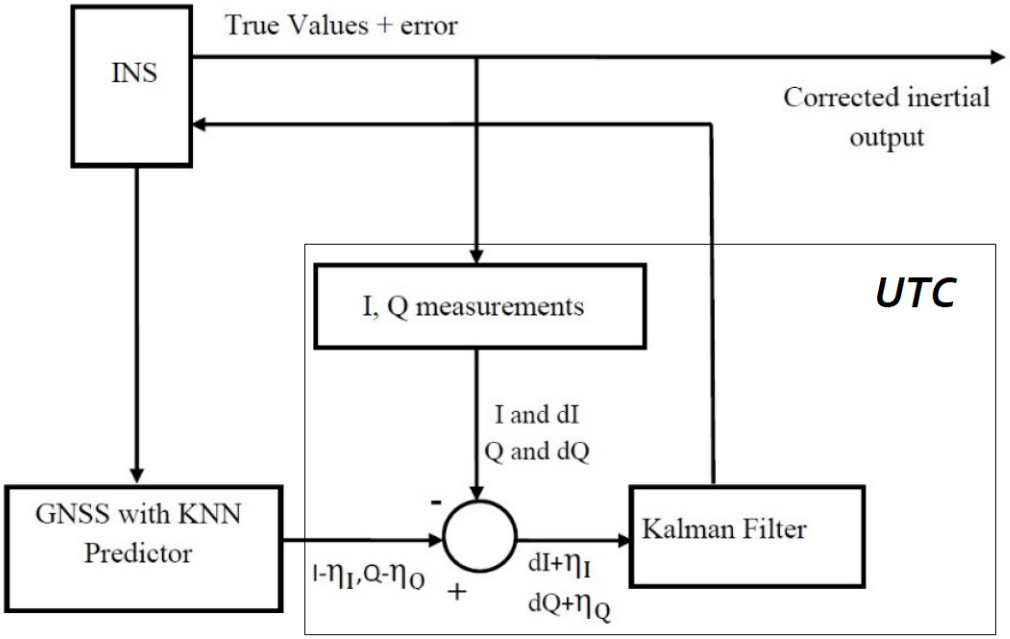


**Figure 4.7:** Kalman filter for ultra-tightly coupled GNSS/INS Integration

$$d(X,Y,Z) = \sqrt{\sum_{i=1}^{n}(X1_i - X2_i)^2 + \sum_{i=1}^{n}(Y1_i - Y2_i)^2 + \sum_{i=1}^{n}(Z1_i - Z2_i)^2} \tag{4.1}$$

where $x_{\text{train}}$ is $X1$, $Y1$, and $Z1$; and $x_{\text{test}}$ is $X2$, $Y2$, and $Z2$.

The KNN method selects the data points closest to the testing data in GNSS to ask for training data. Then, the data output from the k training can be chosen to be the nearest neighbors to predict the unknown GNSS data. Thus, the following KNN equation is used to predict the required data [88]:

$$\hat{y}_l = \frac{1}{k}\sum_{j=1}^{k} y_j \tag{4.2}$$

where $k$ is the number of nearest neighbors of $y_j$.

Hence, to consider the correlation between times, the following equation can be used for GNSS data prediction [87]:

$$\hat{y}_l = \sum_{j=1}^{k} \omega_j y_j \tag{4.3}$$

where $\hat{y}_l$ is the testing of the predicted data, $y_j$ is the testing data, and $\omega_j$ is the weight of the *j-neighbor*. When $n$ is the number of the training data, the KNN time series model can be presented as [87]:

$$\omega_j = j/n \tag{4.4}$$

DOI:10.15774/PPKE.ITK.2023.002

### 4.4.2 Kalman filter

In order to navigate precisely with GNSS, the INS systems have to ensure that INS is the essential keeper of short-term navigation information. The Kalman filter keeps navigation information as accurate as the noise sources allow. In GNSS/INS integration, the Kalman filter represents the stochastic vehicle dynamics with the INS and uses it to estimate, correct, and compensate for errors in the INS implementation. A vital feature of the integrated navigator is maintaining short-term accuracy when GNSS signals are not available for a few seconds [89; 90; 91].

The Kalman filter is the optimal estimator of the expected value of the state of the process in the case of the zero-mean white noise of the measurements. It is a set of equations in quadratic form, and the process can be described with a stochastic difference equation. Regardless of any optimum criterion, the Kalman filter is considered the conditional expectation process of the state-space of concern to the whole past observation stream. Thus, the estimated value of $X(k)$ (discrete-time from) is $\hat{X}(k|k)$ and defined by [90; 92; 93]:

$$\hat{X}(k) = E\{X(k)|Y(k)\} \tag{4.5}$$

where $\hat{X}(k)$ is the estimated state, $E\{\ \}$ is the expected value, $Y(k)$ represents all the data history $\{Y(0), Y(1), Y(2), Y(3)\ \ldots\ Y(k)\}$, and the associated estimate error covariance matrix is given by the following:

$$P(k|k) = E\{[X(k) - \hat{X}(k|k)][X(k) - \hat{X}(k|k)]^T\} \tag{4.6}$$

where $P(k|k)$ is the error covariance matrix. The following linear recursive formulas summarize the optimal Kalman filtering algorithm:

- ***Filter estimate***

$$\begin{aligned}\hat{X}(k|k) = F(k,k-1)\hat{X}(k-1|k-1)\ + K(k)[Y(k) \\ -H(k)F(k,k-1)\hat{X}(k-1|k-1)]\end{aligned} \tag{4.7}$$

- ***Filter gain***

$$K(k) = P(k|k-1)H^T(k)[H(k)P(k|k-1)H^T(k) + R(k)]^{-1} \tag{4.8}$$

- ***Error covariance***

$$P(k+1|k) = F(k,k-1)P(k|k)F^T(k,k-1) + Q(k) \tag{4.9}$$

$$P(k|k) = [I - K(k)H(k)]P(k|k-1) \tag{4.10}$$

where

$$\begin{cases}\hat{X}(k):\ n\ \times\ 1 \text{ estimated state vector} \\ F(k)\text{: n} \times \text{n state transition matrix} \\ K(k)\text{: n} \times 1 \text{ Kalman gain vector} \\ Q(k)\text{: n} \times 1 \text{ covariance matrix of the system noise vector} \\ R(k)\text{: m} \times 1 \text{ covariance of the measurement noise vector} \\ H(k)\text{: m} \times \text{n observation matrix} \\ P(k)\text{: n} \times \text{n covariance matrix of the state vector}\end{cases}$$

Initial estimates of $P(0|0)$ and $\hat{X}(0|0)$ are required for this algorithm..

DOI:10.15774/PPKE.ITK.2023.002

### 4.4.3 Ultra-tightly coupled integration of GNSS/INS

The ultra-tight GNSS/INS integration is becoming more popular despite its implementation complexities (the INS is collocated with the GNSS), as it has unique advantages such as excellent anti-jamming performance and increased dynamic ranges. In the case of ultra-tight GNSS/INS integration, *I and Q* (In-phase and Quadrature) variables from the GNSS correlator are integrated with the position, velocity, and attitude of the INS. The main difference between ultra-tight coupling and the widely used loose or tight GNSS/INS integration methods is that the INS aiding of the GNSS receiver is optional in loosely or tightly coupled systems, whereas, in the case of ultra-tight coupling, it is part of the integration. The main reason behind this is that the GNSS and INS variables are strongly connected through the vehicle's dynamics. Another advantage of integrating INS data into the GNSS tracking loop is that it can suppress the Doppler effect between the satellites and the receiver introduced by the vehicle dynamics. Thus, this design makes the GNSS more reliable in an extended dynamic range, which is almost impossible to achieve with other techniques (such as increasing the carrier tracking loop bandwidth, which increases the thermal noise, possibly degrading the measurement accuracy). The mathematical analysis and the ultra-tight integration design based on the Kalman filter are introduced in [94]. The architecture and equations are as follows.

Equation (4.11) is used to estimate the phase and frequency of the GNSS signal [91; 92]:

$$y(t) = AC(t-t_1)D(t-t_1)\cos(w(t-t_1)+\psi_d(t))+\xi. \tag{4.11}$$

By neglecting the effect from the atmosphere, the delay propagation ($\tau$) can be given as follows:

$$t_1 = \frac{|X_s(\tau_t)-X_u(\tau_r)|}{c} \tag{4.12}$$

$$A = \sqrt{2P} \tag{4.13}$$

$$\tau_r = \tau_t + \tau \tag{4.14}$$

$$w = 2\pi D(t) \tag{4.15}$$

where $\tau_t$ is the time of the transmitting signal, $\tau_r$ is the time of the receiving signal, $t$ is the time of the routing period, $X_s(\tau_t)$ is the GNSS satellite position, $X_u(\tau_r)$ is the user position, $P$ is the signal power, $C(t)$ is the sequence of the code C/A, $\tau$ is the delay propagation, $D(t)$ is the navigation message at 50 Hz, the navigation message is the phase of the initial carrier, $\xi$ is the Gaussian Noise, $c$ is the velocity of light, and $w$ is the angular frequency.

From the above equations, one can write equation (4.11) as follows [95]:

$$y(t) = AC(t-t_1)D(t-t_1)\cos\left(w't+\psi'\right)+\xi \tag{4.16}$$

$$yw' = w\left(1-\frac{v_r}{c}-\frac{a_r}{c}(t+2t_0)\right) \tag{4.17}$$

$$\psi' = -\frac{w}{c}(\,|X_s(t_0-\tau)-X_u(t_0)\,|-v_r t_0+a_r t_0^2)+\varphi_d \tag{4.18}$$

Equations (17) and (18) represent the association of velocity and position with frequency and phase. The sequential loop function may represent the path for existing parameters in order to obtain navigation data.

DOI:10.15774/PPKE.ITK.2023.002

$$v_r = \frac{d}{dt} \left| X_s\left(t_0 - \tau\right) - X_u\left(t_0\right) \right| \tag{4.19}$$

$$a_r = \frac{d^2}{dt^2} \left| X_s\left(t_0 - \tau\right) - X_u\left(t_0\right) \right| \tag{4.20}$$

where $w'$ is the receiver carrier frequency, $\psi'$ is the phase of the GNSS signal, and $t_0$ is the time at the reference point. To explain the relationship between $I$, $Q$, $w'$, and $\psi'$, let $\hat{w}$ and $\hat{\psi}$ be the estimated values of the receiver and k (number of iteration); hence, by multiplying the estimated local carrier ($\hat{\psi}$) with the signal arriving and integrating redetection interval, one can get a quadrature signal [96].

$$I = \int_{KT}^{(K+1)T} \sin\left(\hat{wt} + \hat{\psi}\right) \left[A cos\left(w't + \psi'\right) + \xi_I\right] dt \tag{4.21}$$

$$Q = \int_{KT}^{(K+1)T} \cos\left(\hat{wt} + \hat{\psi}\right) \left[A cos\left(w't + \psi'\right) + \xi_Q\right] dt \tag{4.22}$$

$I$ and $Q$ data are quadrature-phase signal data. According to Figure 4.7, there is a feedback link from the Kalman filter data to the INS, and then we make measurements to evaluate I and Q data according to equations (4.21) and (4.22). When they are feedback from the Kalman filter, which has a link from GNSS, their rates, in the beginning, are 1 Hz. Before the KNN predictor, the GNSS rate is 1 Hz. Thus, we assume that the GNSS data are available every 1 sec. Equations (4.21) and (4.22), as shown above, can be written as follows [94; 96]:

$$I = \int_{KT}^{(K+1)T} \left(\frac{A}{2}[sin\left(w_e t + \psi_e\right)] + \xi_I\right) dt \tag{4.23}$$

$$Q = \int_{KT}^{(K+1)T} \left(\frac{A}{2}[cos\left(w_e t + \psi_e\right)] + \xi_Q\right) dt \tag{4.24}$$

$$w_e = \hat{w} - w' \tag{4.25}$$

$$\psi_e = \hat{\psi} - \psi' \tag{4.26}$$

where $I$ and $Q$ are the elements generated by the mixer, $\xi_I$ and $\xi_Q$ are the components of quadrature noise, $w_e$ is the frequency error, and $\psi_e$ is the phase error. The errors are then reduced from the iteration loops, and by taking the supposition and integration of Equations (4.23) and (4.24), the result is as follows [95; 96]:

$$E\left[I\right] = \frac{-A}{2w_e}\left[cos\left(w_e\left(K+1\right)T + \psi_e\right) - cos\left(w_e KT + \psi_e\right)\right] \tag{4.27}$$

$$E\left[Q\right] = \frac{-A}{2w_e}\left[sin\left(w_e\left(K+1\right)T + \psi_e\right) - sin\left(w_e KT + \psi_e\right)\right] \tag{4.28}$$

$$w_e = \frac{w}{c} \left| v_u - \hat{v}_u \right| = \frac{w}{c} v_e \tag{4.29}$$

$$\psi_e = \frac{-w}{c}\left[\left|x_u - \hat{x}_u\right| - \left|v_u - \hat{v}_u\right| t\right] = \frac{-w}{c}\left[x_e - v_e t\right] \tag{4.30}$$

DOI:10.15774/PPKE.ITK.2023.002

where $T$ is the rate data; $x_u$ and $v_u$ are the position and velocity, which are measured at the receiver; $\hat{x}_u$ and $\hat{v}_u$ are the position and velocity of the receiver estimates; $x_e$ and $v_e$ are the position and velocity errors. The represented measurements by the complementary filter are $Y$, where $Y = (\text{INS measurements}) - (\text{GNSS measurements})$. Hence, by combining velocity and position with ($I$ and $Q$) measurements, and according to Figure 4.7, one can get the following equations [64; 96]:

$$dE[I] = \frac{1}{2}\left[\frac{\partial E[I]}{\partial \psi_e}\frac{\partial \psi_e}{\partial x} + \frac{\partial E[I]}{\partial w_e}\frac{\partial w_e}{\partial x}\right] \tag{4.31}$$

$$dE[Q] = \frac{1}{2}\left[\frac{\partial E[Q]}{\partial \psi_e}\frac{\partial \psi_e}{\partial \dot{x}} + \frac{\partial E[Q]}{\partial w_e}\frac{\partial w_e}{\partial \dot{x}}\right] \tag{4.32}$$

$$z = \{I + dI, Q + dQ\}_k - \{I - \xi_I,\ Q - \xi_Q\}_k \tag{4.33}$$

$$z = \{dI + \xi_I, dQ + \xi_Q\}_k \tag{4.34}$$

where $dI$ and $dQ$ are the deviations of INS measurements due to the inertial INS sensor ($I$ and $Q$), $\xi_I$, and $\xi_Q$ are the GNSS ($I$ and $Q$) measurements' components of the quadrature noise, and k is the iteration number. The two measured components from the INS ($I$ and $Q$) will be subtracted from the GNSS receiver components ($I$ and $Q$). The result is shown in the equation (4.34). Thus, the Kalman filter treats the remaining signal after subtraction and generates the estimation error.

DOI:10.15774/PPKE.ITK.2023.002

## 4.5 Measurement based computation results

The INS and GNSS computation data were obtained from the drone autopilot records. The logs were formed during a video recording campaign Mátyásföld model airport close to Budapest; see section 4.2. Therefore, the investigations were conducted using a 3DR Iris+ drone with ArduCopter firmware [75; 81; 80].

To keep the mathematical model simple enough to be manageable, it is frequently necessary to ignore certain properties of the system. Hopefully, the advantage gained from mathematical simplicity offsets the errors introduced by ignoring some aspects of the system. Hence, we have considered that the recorded INS data from the drone was not merged with other sensors to simplify the computation. It would be suitable for algorithms that require real-time calculations, such as in our case. Another aspect is that this algorithm would be mostly used for situations when a fixed-wing aircraft encounters satellite signal loss during turn maneuvers.

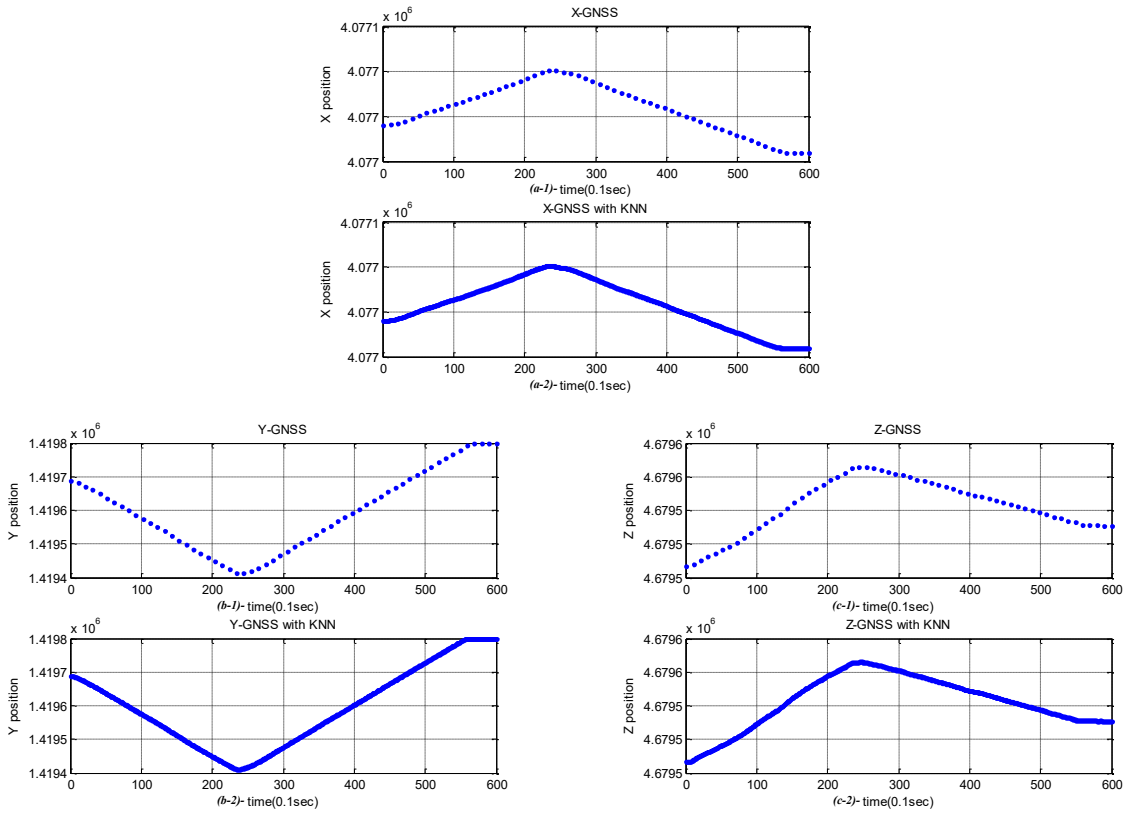


**Figure 4.8:** Comparing the drone trajectory coordinates in (X, Y, and Z) when using the the GNSS data without a predictor and GNSS data with a KNN predictor; a-1 shows the drone trajectory in $X$-axis without using the KNN predictor; a-2 shows the drone trajectory in $X$-axis by using the KNN predictor; b-1 shows the drone trajectory in $Y$-axis without using the KNN predictor; b-2 shows the drone trajectory in $Y$-axis by using the KNN predictor; c-1 shows the drone trajectory in $Z$-axis without using KNN predictor; c-2 shows the drone trajectory in $Z$-axis by using the KNN predictor

DOI:10.15774/PPKE.ITK.2023.002

The INS information is available every 0.1 sec, while the GNSS receiver information is available every second. Nevertheless, the INS and GNSS must be time-synchronized to estimate the errors from the two frameworks in a specific time interval. Figure 4.8 shows the comparison of the drone trajectory coordinates in (X, Y, and Z) when using the (GNSS data without a predictor) and (GNSS data with a KNN predictor). This Figure shows the drone's trajectory in the three coordinates, represented by 60 points. At each point, GNSS provides the target position (X, Y, and Z). These points are 1 sec apart, and hence the whole duration of the trajectory is 60 sec.

The KNN predictor algorithm was used to enable GNSS receiver output to predict between samples instant when the GNSS signal is lost for a few seconds. Hence, after adding the KNN predictor to the GNSS receiver's output, it has 600 points of (target position (X, Y, and Z)); these points are 0.1 sec apart for the same whole 60-sec duration of the trajectory. The following scenarios are taken for the evaluation performance of the proposed GNSS/INS system (all of these scenarios are taken after adding the KNN predictor for the integration of GNSS/INS):

**Scenario (I):** This scenario compares the positions in three coordinates (X, Y, and Z) for INS, GNSS, and the integration of GNSS/INS without blocking the GNSS data (see Figure 4.9).

Figure 4.9 (a) presents the simulation of the integrated positioning, INS positioning, and GNSS localization signs in the X-axis for 60 sec. Firstly, we can observe that the integrated positioning lies between the INS and the GNSS localization signals, which indicates that the integration synthesis is well-performing. It also shows that the integrated positioning signal follows the INS signal with a constant error. Simulation of the positioning systems in the Y-axis for 60 sec is demonstrated in Figure 4.9 (b), again it has the same performance in part (a) that the integrated signs are following the INS signal with a constant error. Moreover, Figure 4.9 (c) shows the behavior of the integrated positioning signal that tracks the INS signal with a steady error in the Z-axis for the same period.

**Scenario (II):** This scenario is like Scenario (I) but with a blocking time of 1 sec in the GNSS receiver (see Figure 4.10).

The same integration methodology utilized in the first scenario is employed with the slight blocking of the GNSS signal as 1 sec. So Figure 4.10 (a) shows the X-axis of integrated positioning, INS, and GNSS signal behaviors for 60 s; it can be seen that the new signal (i.e., integrated signs) has still tried to track the INS signal. However, of course, it has a more significant error when the GNSS has lost that it depends on the GNSS signal; see Figure 4.7. Then the Y-axis of the integrated signals is shown in Figure 4.10 (b), and it also presents that the integration signal is stacked in the same error problem when the GNSS signal is lost. Afterward, Figure 4.10 (c) displays the behavior of the integrated signal in the Z-axis for 60

DOI:10.15774/PPKE.ITK.2023.002

sec when the GNSS signal has blocked for 1 sec; also, it can be observed that there is an error gap at the period of GNSS lost.

**Scenario (III):** This scenario is like Scenario (I), but with a blocking time of 4 sec in the GNSS receiver (see Figure 4.11).

Employing the same integration procedure as in the previous scenarios, the simulation of the integrated positioning system connecting to the GNSS signal is blocked for 4 sec. Figure 4.11 (a) displays the X-axis of integrated positioning, INS, and GNSS signal behaviors for 60 sec. It can be noticed that the new signal has tracked the INS signal even though the new positioning signal has a more considerable error within the period of the GNSS being blocked regarding the longer blocking time of the GNSS signal. Additionally, Figure 4.11 (b) presents the Y-axis of the integrated positioning signs for 4 sec of GNSS blocked time. Also, Figure 4.11 (c) shows the Z-axis of the integrated positioning signs in 60 sec when the GNSS signal is lost for 4 sec.

**Scenario (IV):** This scenario is like Scenario (I), but with a blocking time of 8 sec in the GNSS receiver (see Figure 4.12).

Finally, the integrated positioning sign simulations concerning the 8 sec of the GNSS blocking signal are performed. Figure 4.12 (a) presents the X-axis simulation of the integrated positioning, INS, and GNSS signals for 60 sec, incorporating an 8 sec lost signal from GNSS. It can be clearly seen that the integrated signs have a bigger error than the above scenarios; thus, as a final corollary, the error accumulates whenever the blocking period is increased. Nevertheless, Figure 4.12 (b) shows the simulation of the integrated positioning signs in the Y-axis for 60 sec, with the total blocking time of the GNSS signal being 8 sec. Later on, Figure 4.12 (c) illustrates the simulation of the integrated signs in the Z-axis for 60 sec with a signal loss of 8s.

From the above scenarios, one can conclude that using GNSS/INS with a KNN predictor can decrease the deviation in the three coordinates (X, Y, and Z) when there is a blocking in time (lost signal) for a few seconds in the GNSS receiver. The standard deviation of INS, GNSS without predictor, and GNSS/INS with KNN predictor can be seen in Table 4.1 when the GNSS receiver is used with and without blocking for a few seconds.

To answer the question of why we should synchronize the GNSS signal, we need to explain that the INS updates every 0.1 seconds, while GNSS updates every 1 second. This is because after receiving the satellite signal, the receiver demodulates it, generates a signal similar to the satellite signal, and shifts registers to be identical to the satellite signal. Next, the receiver has to calculate the time difference to find the distance of the receiver from the satellite. Then, decode the signal to provide the navigational message. This procedure must be carried out in the receiver for at least four satellites in order to compute the position of the aerial vehicle in ECEF coordinates, which are then converted to a geodetic coordinate frame.

DOI:10.15774/PPKE.ITK.2023.002

**Table 4.1:** The standard deviation of INS, GNSS without predictor, and GNSS/INS with KNN predictor, when the GNSS receiver with and without blocking in a few seconds

| GNSS | Standard Deviation | | | | | | | | |
|---|---|---|---|---|---|---|---|---|---|
| | $\sigma_{INS}$ | | | $\sigma_{GNSS}$ | | | $\sigma_{GNSS/INS}$ | | |
| | X-Axis | Y-Axis | Z-Axis | X-Axis | Y-Axis | Z-Axis | X-Axis | Y-Axis | Z-Axis |
| **No blocking** | 27.8269 | 117.5755 | 15.7477 | 27.6191 | 117.2243 | 15.8113 | 27.7402 | 117.4276 | 15.7710 |
| **1 sec blocking** | 27.8269 | 117.5755 | 15.7477 | 27.5380 | 117.1091 | 15.6933 | 27.7465 | 117.4192 | 15.7247 |
| **4 sec blocking** | 27.8269 | 117.5755 | 15.7477 | 27.4144 | 116.8594 | 15.3463 | 27.6745 | 117.1738 | 15.6184 |
| **8 sec blocking** | 27.8269 | 117.5755 | 15.7477 | 26.6793 | 115.8801 | 15.0102 | 27.4085 | 116.6536 | 15.5051 |

Furthermore, because this is a novel investigation employing the KNN algorithm predictor for data synchronization of ultra-tight GNSS/INS integration, we conducted a brief evaluation of this study by comparing the prediction data accuracy with some of the state-of-the-art methods employing similar main ideas, as shown in table 4.2.

The main drawback of the Least-Mean-Square Algorithm (LMS) is that it is sensitive to the scaling of its input. This makes selecting a learning rate that ensures algorithm stability inconceivable. The Normalized Least Mean Squares Filter (NLMS) is a variant of the LMS algorithm that solves this problem by normalizing the input power. The normalized least-mean-square (NLMS) algorithm usually converges faster than the LMS algorithm since it utilizes a variable convergence factor, but it is still unstable for large datasets [65].

Wavelet Neural Networks (WNNs) is mathematical functions that split data into different frequency components and then study each component with a resolution matched to scale. The proposed approach based on the WNNs uses Morlet as an activation function in the hidden layer of the wavelet neural network, while the Radial Basis Function Neural Networks (RBFNNs) use a basis function that can be calculated as a Gaussian function. The Wavelet Neural Networks (WNNs) method for prediction has great ability, suitability, and more stability for GPS prediction than RBFNN, but it needs more time for alteration, which is not suitable for unmanned aerial vehicles [66].

In reference [67], they suggested a carrier phase prediction method based on carrier open-loop tracking to achieve carrier phase continuity. In order to increase the effectiveness of phase prediction, the prediction approach investigates reliable receiver clock drift estimates. It focuses on extending the effective time of carrier phase prediction by accurately estimating the receiver clock drift. Then it may overcome the carrier phase discontinuity problem caused by frequent signal blockages of particular satellite signals. This positioning method is more accurate than the methods that rely on the frequency and amplitude of the signal because it is very sensitive to any slight change in a moving signal. However, it continued to rely on assumptions and, as a result, extended the processing time.

DOI:10.15774/PPKE.ITK.2023.002

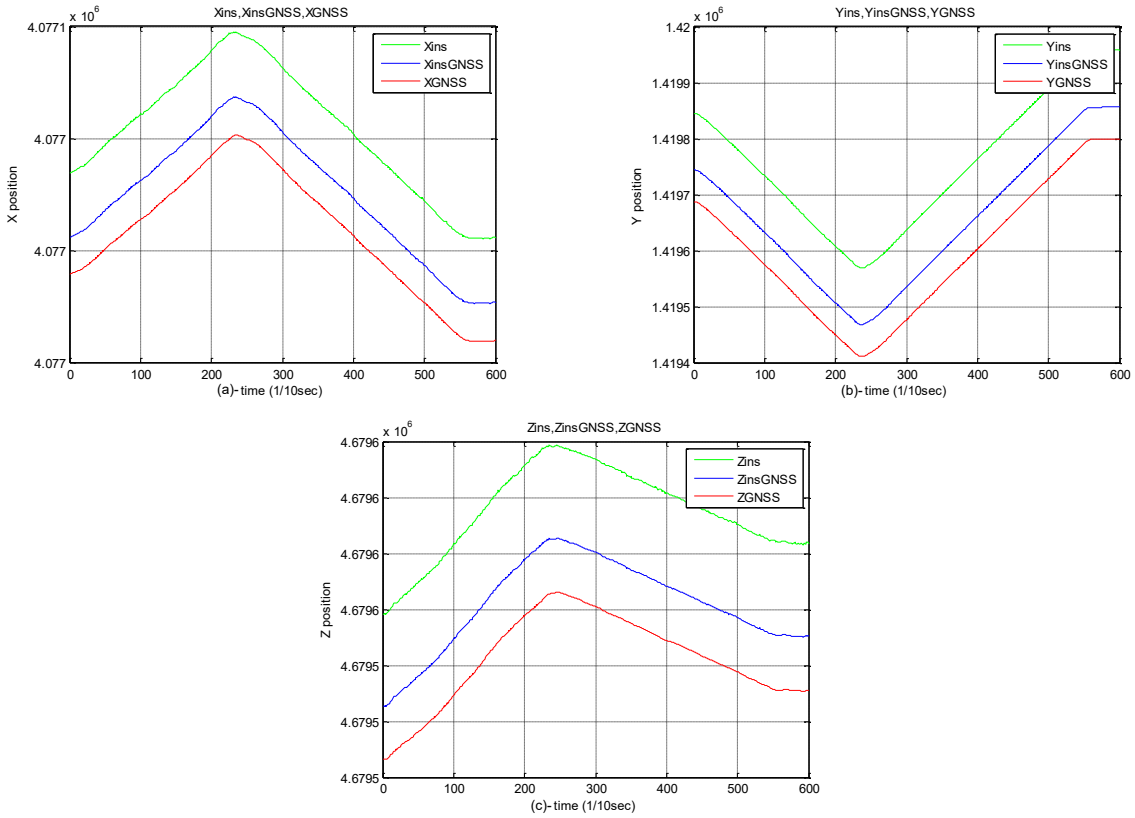


**Figure 4.9:** Comparing between the positions in three coordinates (X, Y, and Z), for INS, GNSS, and integration of GNSS/INS without blocking in the GNSS data; *a* shows the INS, GNSS, and integration of INS/GNSS routes in *X*-axis without GNSS blocking; *b* shows the INS, GNSS, and integration of INS/GNSS routes in *Y*-axis without GNSS blocking; *c* shows the INS, GNSS, and integration of INS/GNSS routes in *Z*-axis without GNSS blocking

DOI:10.15774/PPKE.ITK.2023.002

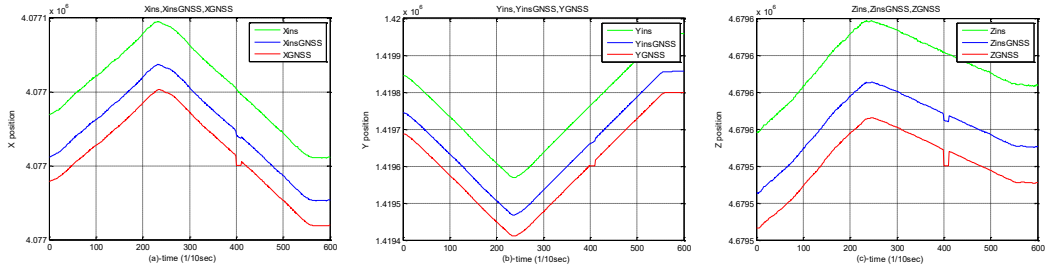


**Figure 4.10:** Comparing between the positions in three coordinates (X, Y, and Z) for INS, GNSS, and integration of GNSS/INS when blocking of (1 sec) are observed in the GNSS data; *a* shows the INS, GNSS, and integration of INS/GNSS routes in *X*-axis with one second of GNSS blocking; *b* shows the INS, GNSS, and integration of INS/GNSS routes in *Y*-axis with one second of GNSS blocking; *c* shows the INS, GNSS, and integration of INS/GNSS routes in *Z*-axis with one second of GNSS blocking.

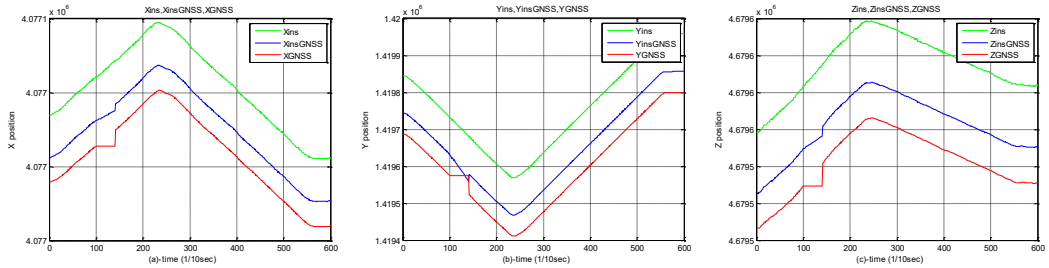


**Figure 4.11:** Comparing between the positions in three coordinates (X, Y, and Z) for INS, GNSS, and integration of GNSS/INS through blocking of (4 sec) are accord in the GNSS data; *a* shows the INS, GNSS, and integration of INS/GNSS routes in *X*-axis with 4 sec of GNSS data blocking; *b* shows the INS, GNSS, and integration of INS/GNSS routes in *Y*-axis with 4 sec of GNSS data blocking; *c* shows the INS, GNSS, and integration of INS/GNSS routes in *Z*-axis with 4 sec of GNSS data blocking

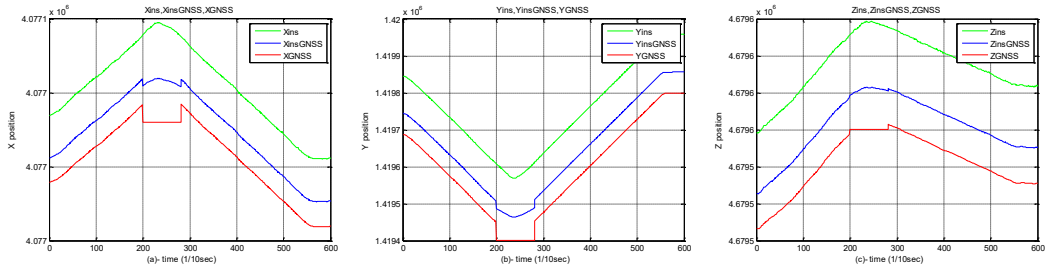


**Figure 4.12:** Comparing between the positions in three coordinates (X, Y, and Z) for INS, GNSS, and integration of GNSS/INS when blocking of (8 sec) are followed in the GNSS data; *a* shows the INS, GNSS, and integration of INS/GNSS routes in *X*-axis with 8 sec of GNSS data blocking; *b* shows the INS, GNSS, and integration of INS/GNSS routes in *Y*-axis with 8 sec of GNSS data blocking; *c* shows the INS, GNSS, and integration of INS/GNSS routes in *Z*-axis with 8 sec of GNSS data blocking

DOI:10.15774/PPKE.ITK.2023.002

**Table 4.2:** Brief evaluation of prediction methods

| Reference | Prediction for GPS or GNSS | Method of Predictor | Accuracy |
|---|---|---|---|
| [65] | GPS | NLMS | low |
| [66] | GPS | RBFNN and WNNs | medium |
| [67] | GNSS | Carrier phase prediction | high |
| Our method | GNSS | KNN | high |

## 4.6 Conclusions

Integrating GNSS and INS systems can amend the weaknesses inherent in each and combine their advantages. The GNSS is an accurate localization technology; yet, it is relatively slow to update and may be lost due to several issues. The INS is a precise and instant positioning system, but it needs regular calibration. When INS information is available in 0.1 sec, while GNSS receiver information is available every second, a prediction between the GNSS receiver's sampling instants is required. Different predictors can be used for GNSS receivers, selecting the best one depending on its prediction results. Because time synchronization between INS and GNSS must be achieved to estimate the errors from the two systems simultaneously, a new technique of using a predictor on GNSS output before integrating with the INS has been employed. The KNN predictor algorithm employs the database to search for data that is similar to the current data; hence, this algorithm was implemented at the output of the GNSS receiver to improve the synchronization process between INS and GNSS and predict the output of the GNSS receiver when its signal is lost (data blocking) for a few seconds. So the computations provided reasonable position values between every two GNSS signals in the three coordinates (X, Y, and Z); see Figure 4.8. Moreover, ultra-tight integration between GNSS and INS was also performed because of its advantages, such as anti-jamming immunity and increased dynamic ranges. Then, for a few seconds, GNSS data were clutched in different scenarios, both with and without blocking, to classify the integration robustness and simulate the new dynamic signal behavior in the three axes. Based on the results, it can be stated that the error values along the three axes (X, Y, and Z) get bigger as the GNSS data-blocking period gets longer. In simple terms, the error values increase whenever the GNSS data-blocking time is extended. In conclusion, the errors obtained when using GNSS/INS with predictor are less than those obtained when using INS alone or GNSS without predictor for the same blocking periods in the GNSS data; see Figures (4.10, 4.11, and 4.12).

DOI:10.15774/PPKE.ITK.2023.002

# Chapter 5

# Summary and conclusions

## 5.1 Summary of results

In the last twenty years, CubeSats have attracted the attention of many universities, a comprehensive range of national space agencies, and professional space companies due to their low cost, flexible technology applying COTS components, and faster development phases. However, satellites encounter an enormous thermal variation during the Earth's Sunlit and eclipse periods while orbiting Earth. One key challenge is keeping the CubeSat components within their operational thermal limits to guarantee efficiency. In addition, satellite-based navigation systems are challenging in built-up areas, mainly to the signal blockage problem. Besides, onboard navigation components have inherent accumulative errors. Therefore, the leading conventional navigation solutions are satellite navigation signals frequently integrated with inertial navigation measurements that compensate for each other.

The follow-up on these research fields is to create mathematical models to interpret the key issues that need investigations based on physical laws and potentially simplifying assumptions. First, a thermal mathematical model describing the CubeSat surface and its central propellant tank, thermal behaviors along with its orbital motions has been derived. Next, this model was employed to investigate the satellite's thermal behavior and the thermal transition responses with a feasible passive control synthesis to regulate CubeSat-specific element temperatures fulfilling power limitations in the CubeSat throughout its orbit. Then, the active thermal was selected to regulate tank temperatures at the reference temperature value and eliminate the CubeSat propellant thermal fluctuations along the satellite orbit. Finally, because power is the most concerning subject in a CubeSat, an optimization-based model-predictive approach was developed to simultaneously design an optimal solar panel ratio considering the feasible heating power delivered to the system and the propellant tank thermal responses throughout the CubeSat orbital motion.

Furthermore, to deal with navigation accuracy problems, a KNN predictor algorithm is proposed at the GNSS receiver's output to predict between samples of instant GNSS data for synchronization purposes with INS. Also, an ultra-tightly coupled integration technique has been exploited to correct the INS measured data with accumulated errors over time, based on GNSS received data.

DOI:10.15774/PPKE.ITK.2023.002

A simulation framework in Matlab has been developed to study four different integration scenarios containing data-blocking situations of different lengths using real data measurements. The obtained results have shown that the computed signals of the GNSS/INS integration yield more accurate position data when the GNSS signal is blocked. However, the proposed integration technique is able to maintain sufficiently precise localization even when GNSS signals are not available for 1, 4, or 8 seconds. This advantageous feature is guaranteed by the physical background of the applied KNN algorithm. Below is a more detailed discussion of the results.

- Different surface compositions have been investigated in section 2.3. The simulation results showed CubeSat surface and propellant temperatures were higher than their respective temperature limits *see section 2.2.3* in the case in which the CubeSat surface was made of an uncoated aluminum alloy, as shown in Figure 2.2.

- In CubeSats, a passive control system is a common thermal regulation strategy. Therefore, I assumed a polished CubeSat surface with magnesium oxide-aluminum oxide paint. The simulation results demonstrated that the CubeSat temperatures were dropped, as shown in Figure 2.3.

- To generate a Quasi-LPV formulation of the nonlinear thermal model of the CubeSat, first, we combined the three interval equations into an equivalent model containing seven equations regarding solar panel ratio ($\lambda$). Then we investigated the thermal effects of the various solar panel ratios, $\lambda = 0.3, 0.5, 0.6,$ *and* $0.7$*, which are partially covering the satellite's three faces*, on the CubeSat surface and its propellant tank. The simulation results illustrated that the CubeSat temperatures were increased by increasing the solar panel ratios, as shown in Figure 2.7. Thus, the thermal constraints should be considered in the computations of the optimal solar panel ratios for the CubeSat.

- The comparison of simulations of the equivalent model in section 2.4 in parallel with the TMM section 2.3 without a controller and with active controller syntheses were evaluated. The simulation results for the CubeSat surface and fuel tank thermal performances in the periodic orbit were similar for the two models, as shown in Figures 2.8 and 3.13, respectively.

- In section 3.2, a PID-based approach was applied as an active control system to regulate the tank temperature of the CubeSat at the reference value as well as to eliminate thermal fluctuations of the tank temperature via CubeSat orbit. Figure 3.7a demonstrates that the fuel tank temperature, *employing anti-windup PID with restricted heating power of 1.5 W*, tracks the reference temperature value with desirable overshoot and a short settling time response. In addition, different heating powers, *which are supposed to maintain the fuel tank thermal performance when the heater is subjected to PID-based controllers*, were investigated. By comparing Figures 3.8 and 3.9, we can see that the anti-windup PID control system consumes the lowest heating power to grant an appropriate thermal response to the CubeSat fuel tank along the orbit.

DOI:10.15774/PPKE.ITK.2023.002

- Employing the nonlinear model in section 2.3, a linearization-based thermal regulation synthesis for the CubeSat fuel tank was derived. Matlab/ Simulink model has been employed to simulate the CubeSat surface and fuel tank regulated thermal performances by conducting input/output linearization feedback law, as shown in Figure 3.10, with a heating power consumption range of 1.5 W, *as shown in Figure 3.12*. The simulation results in Figure 3.11 present the linearization-based technique's capability to control the fuel tank temperature at the reference value with an appropriate thermal response.

- The *off-line* MPC approach is used in the section 3.5 for the quasi-LPV model of the CubeSat in the section 2.5. An MPC framework was exploited to integrate active and passive control strategies for both an appropriate control input signal ($\dot{Q}_c$) and an optimal solar panel area ($\lambda\ A$), which covered three faces of the CubeSat surface. The results of the MPC optimization for the six different case studies are illustrated in detail in section 3.5.3 and Figures 3.14-3.19. Finally, the results of the simulations indicated that the optimal solar panel ratio changes depending on the tolerances of the acceptable reference temperature value and the amount of rabbling in the thermal response. However, ($\lambda = 1$) is not a realistic value for solar panel coverage since we cannot supply a control input sequence that keeps the faces and the tank temperature below the prescribed values.

- The INS measurements of drones are assumed to be provided every 0.1 seconds, while the GNSS receiver provides information about the drone's position every second. Therefore, we addressed this gap by formulating a KNN predictor to predict between sampling instant of the GNSS receiver for the synchronization purpose between the two systems (INS and GNSS) before the integration process; see Figure 4.8. The performance of the KNN predictor was also examined when the GNSS signal was lost for a few seconds for different reasons. Hence, the performances of GNSS with no blocking, and blocking for 1, 4, and 8 seconds, respectively, are presented as shown in Figures 4.9 - 4.12.

- The ultra-tightly coupled GNSS/INS integration system described in 4.4.3 was designed and implemented in order to achieve the integration between the INS and GNSS techniques, where the purpose of the Kalman filter in this system is to estimate the system errors based on the measurement errors between the GNSS and INS systems.

- From Figures (4.9 - 4.12) and Table 4.1, we can simply conclude that the integrating GNSS/INS system obtained more precise results than each system standing alone, especially when the GNSS signal is lost for a few seconds. Also, from Table 4.1, one can see that the standard deviation values for GNSS without a KNN predictor and for 8 seconds of signal blocking time in the three axes (X = 26.6793, Y = 115.8801, Z = 15.0102) are smaller than the values of the standard deviation for GNSS with a KNN predictor and for the same period of blocking time in the three axes (X = 27.4085, Y = 116.6536, Z = 15.5051). Finally, Figure 4.12 shows that when the GNSS receiver signal is blocked, the integrated GNSS/INS system will be more reliable.

DOI:10.15774/PPKE.ITK.2023.002

## 5.2 Conclusion

The main contributions and the proposed theses of this work are summarized in this section, and then the possible directions for further research are given. The relevant Chapter of the dissertation and the related publications are indicated for each thesis point.

### 5.2.1 New scientific contributions

The main scientific contributions of the dissertation are summarized in the following theses.

**Thesis 1** *Nonlinear thermal modeling of a CubeSat* **(Chapter 2)**

Related publications: **([P1], [P2], [P6], [P7])**

**I have developed a lumped dynamical model describing the surface and internal propellant tank temperatures of a CubeSat performing orbital motion. First, the thermal model in the nonlinear input-affine form, containing seven differential equations for three time intervals and a time-varying disturbance due to orbital motion, has been derived using physical laws and simplifying assumptions. Moreover, I have given the control-oriented Quasi-Linear Parameter Varying (quasi-LPV) form of the model.**

- The simulations showed that the temperatures on the CubeSat surface and fuel tank can be efficiently decreased by appropriately setting the optical surface property of the CubeSat. The material's optical properties can be structured to reduce absorptivity and increase the CubeSat surface emissivity.
- I have designed a passive control method to keep the CubeSat cover and propellant tank temperatures within a predefined range by setting the surface optical properties and changing the solar panels' ratios.
- A quasi-LPV model has been derived in order to accomplish Model Predictive Control in (*Thesis 2*). The simulations showed that the differences between the simulation results of the integrated unified thermal model and the original thermal model are negligible under the same thermal conditions.

The simulation results have shown that the propellant tank temperatures ranged from *484 K to 501 K* for the case in which the CubeSat surface is made of uncoated aluminum. When I assumed a polished CubeSat surface with reflective metallic paint, the tank temperatures dropped, oscillating from *261 K to 266 K*. Furthermore, by simulating different solar panel ratios ($\lambda = 0.3$ *and* $0.7$), the propellant tank temperatures contrasted from *265 K to 302 K*, which is within the propellant tank thermal operational limits.

DOI:10.15774/PPKE.ITK.2023.002

**Thesis 2** *Thermal control approaches for a CubeSat* **(Chapter 3)**

Related publications: **([P2], [P4], [P5], [P7], [P8])**

**I have designed different control schemes to track a constant reference temperature value and avoid the thermal fluctuations caused by the CubeSat's periodic motion on a low Earth orbit simultaneously. PID-based control structures have been used to track the propellant tank temperature along the satellite orbit, applying minimal essential power. As a further development, I have designed a linearization-based controller to maintain the propellant tank temperature at the reference temperature. An optimization-based model-predictive approach for the simultaneous design of an optimal solar panel ratio and a feasible control input sequence has also been proposed and evaluated.**

- I have shown through simulations that the PID-based control system employing an anti-windup strategy keeps the propellant tank at a prescribed temperature value (*290 K*) throughout the satellite orbital. The anti-windup technique has avoided saturation and overshoot response and gave a suitable thermal response for the CubeSat propellant tank through the satellite orbital motion with the least amount of power consumption (*1.3 W*).
- The linearization method supplying the input/output linearization securing the feedback law to the nonlinear thermal model has been implemented for the thermal regulation of the CubeSat propellant tank. As a result, the linearization-based method adjusted the propellant tank temperature to the reference value with an acceptable thermal response and without additional power consumption (*1.5 W*).
- A novel multivariable model predictive control approach was developed which integrates the active and passive thermal control of the CubeSat using its quasi-LPV model. Both the solar area ratio and the heating power were considered inputs in the control scheme. The proposed approach can take into consideration several often contradictory goals and constraints related to power consumption and control performance.

The optimization modifications have revealed that if the temperature constraint of the CubeSat propellant tank is raised to *297 K*, the applicable sides of the CubeSat could be covered entirely by solar cells ($\lambda = 1$). So far, optimal solar panel percentages covering the specific faces of the CubeSat have varied from *44.8% to 100%* regarding the propellant tank thermal limit and the acceptable fluctuation of the thermal response of the CubeSat propellant tank through orbit.

DOI:10.15774/PPKE.ITK.2023.002

**Thesis 3** *Unmanned aerial vehicle navigation using GNSS/INS integration* **(Chapter 4)**

Related publications: **([P3], [P9])**

**I have proposed a novel GNSS data prediction method which uses the K-Nearest Neighbor (KNN) algorithm for improving the data synchronization between the INS sensors and the GNSS receiver. This algorithm is also employed to produce the GNSS loss data. I have designed a reinforced and innovative ultra-tightly coupled approach to integrate the GNSS available data correlator with the INS's position, velocity, and attitude to rectify the INS measurements. I have illustrated the applicability of the approach for improving navigation performance in challenging environments through different scenarios using real measurement data.**

- I have shown through computations that the proposed KNN predictor estimates the missing data between GNSS sampling instants with sufficient precision, which allows the successful synchronization with INS.
- I have shown that the navigation data can be enhanced using an ultra-tight integration approach, where the integration trajectories for the three axes track the GNSS received data in real-time.
- I have developed a simulation framework in Matlab to study four different integration scenarios containing data blocking situations of different lengths using real measurement data collected at the Mátyásföld airfield.

The obtained results have shown that the computed signals of the GNSS/INS integration yield more accurate position data when the GNSS signal is blocked. Moreover, the three axes GNSS standard deviation calculation ($X = 26.6793$, $Y = 115.8801$, $Z = 15.0102$) is smaller than the standard deviation calculation for GNSS/INS ($X = 27.4085$, $Y = 116.6536$, $Z = 15.5051$) when they are subjected to 8 seconds signal blocking period. However, the proposed integration technique is able to maintain sufficiently precise localization when GNSS signals are not available for 1, 4, or 8 seconds. This advantageous feature is guaranteed by the physical background of the applied KNN algorithm.

DOI:10.15774/PPKE.ITK.2023.002

### 5.2.2 Suggestions for future research

The design and operation of small satellite thermal control systems and integrated satellite navigation are complicated tasks involving a vast number of variables and multiple engineering disciplines. Given the encouraging results of this dissertation, we would like to extend the approaches and the results presented in these theses in the following directions.

***Nonlinear dynamic thermal model.*** The dynamic thermal model in section 2.3 is an applicable thermal analysis tool for the CubeSat in its present configuration. It does, however, have certain restrictions. Therefore, it could be extended in a straightforward way to include the interplanetary trajectories of the CubeSat orbit instead of a circular motion and with an actual calculation of the Sun phase time and eclipse orbit duration. We can also make more complex mathematical models of the structure of the CubeSat and more sophisticated dynamic movements of a CubeSat in orbit by considering the actual movement of the satellite rather than just having face 3 of the CubeSat facing the Earth.

◁

***Thermal Control Approaches.*** An important part of the whole design is the passive environment, which is essentially the surface composition and solar panel ratio of the faces. Therefore, future work will be focused on the optimization of these parameters to further reduce the necessary heating energy. The application of thermal active control strategies can be extended to various system designs, such as advanced control synthesis, adaptive control systems, or sliding mode control systems, exploiting the actual thermal model variables and inputs. An on-line MPC could be one of the important directions of research in the future. It simultaneously computes the optimized value of $\lambda$, simulates the satellite's thermal performance, and controls the temperature at the same time.

◁

***Navigation using GNSS/INS integration.*** The navigation strategies are directed toward improving the quality of the IMU sensors, and various sensor properties may be evaluated. Using different types of INS (low-cost, medium-cost, and high-cost) and integrating each type of INS with GNSS. Then we would like to compare the results of integration between GNSS and these three types of integration in order to determine whether integrating low-cost INS with GNSS affects the obtained results or not, to use low-cost INS for integration purposes with GNSS instead of medium-cost or high-cost INS. More sophisticated error models may be used in the Kalman filter. The integration of GNSS/INS can be used, with a new filtering methodology, to achieve optimal noise filtering over the whole motion band of interest.

◁

DOI:10.15774/PPKE.ITK.2023.002

# The author's publications

### Journal papers

[P1] Nawar Al Hemeary, Maciej Jaworski, Jan Kindracki, and Gábor Szederkényi. Thermal model development for a CubeSat. *Hungarian Journal of Industry and Chemistry*:25–32, 2019. DOI: 10.33927/hjic-2019-05.

[P2] Nawar Al-Hemeary, Péter Polcz, and Gábor Szederkényi. Optimal solar panel area computation and temperature tracking for a cubesat system using model predictive control. *SPIIRAS Proceedings*, 19(3):564–593, 2020. DOI: 10.15622/sp.2020.19.3.4.

[P3] Sameir A Aziez, Nawar Al-Hemeary, Ahmed Hameed Reja, Tamás Zsedrovits, and György Cserey. Using KNN Algorithm Predictor for Data Synchronization of Ultra-Tight GNSS/INS Integration. *Electronics*, 10(13):1513, 2021. DOI: 10.3390/electronics10131513.

### Conference papers

[P4] Nawar Al-Hemeary and Gábor Szederkényi. Fuel tank temperature control of a time-varying CubeSat model. In: *2019 IEEE 17th World Symposium on Applied Machine Intelligence and Informatics (SAMI)*. 2019, 339–344. DOI: 10.1109/SAMI.2019.8782765.

[P5] Nawar Al-Hemeary and Gábor Szederkényi. Power Regulation and Linearization - Based Control Design of a Small Satellite. In: *2019 12th International Conference on Developments in eSystems Engineering (DeSE)*. 2019, 646–650. DOI: 10.1109/DeSE.2019.00121.

[P6] Nawar Al-Hemeary and Gábor Szederkényi. Dynamic thermal simulation of the CubeSat. In: *PhD Proceedings Annual Issues of the Doctoral School Pázmány Péter Catholic University, Faculty of Information Technology and Bionics - 2018*. Ed. by P. Szolgay G. Prószéky. Vol. 13. 50/a Práter street, 1083 Budapest, Hungary: Pázmány University ePress, 2018, 32.

[P7] Nawar Al-Hemeary and Gábor Szederkényi. Effect of solar panels ratio on the thermal behavior of a CubeSat. In: *PhD Proceedings Annual Issues of the Doctoral School Pázmány Péter Catholic University, Faculty of Information Technology and Bionics - 2020*. Ed. by P. Szolgay G. Prószéky. Vol. 15. 50/a Práter street, 1083 Budapest, Hungary: Pázmány University ePress, 2020, 127.

[P8] Nawar Al-Hemeary and Gábor Szederkényi. PID-based temperature control of a small satellite. In: *PhD Proceedings Annual Issues of the Doctoral School Pázmány Péter Catholic University, Faculty of Information Technology and Bionics - 2019*. Ed. by P. Szolgay G. Prószéky. Vol. 14. 50/a Práter street, 1083 Budapest, Hungary: Pázmány University ePress, 2019, 87.

[P9] Nawar Al-Hemeary and Gábor Szederkényi. Construction of unmanned aerial vehicles applying INS / GPS navigation. In: *PhD Proceedings Annual Issues of the Doctoral School Pázmány Péter Catholic University, Faculty of Information Technology and Bionics - 2021*. Ed. by P. Szolgay G. Prószéky. Vol. 16. 50/a Práter street, 1083 Budapest, Hungary: Pázmány University ePress, 2021, 125.

**Conference presentations with extended abstract**

[P10] Nawar Al-Hemeary and Gábor Szederkényi. Thermal model development for a CubeSat. In: *5th international Ph.D. Workshop*. Veszprem: University of Pannon, doctoral school of information and technology, 2018.

[P11] Nawar Al-Hemeary and Gábor Szederkényi. Linearization-based thermal control design for a CubeSat. In: *Advanced ICT Tools and Methods for Cyber-Physical Systems and Biomedical Applications. Oral Presentation titled*. Esztergom: Pázmány University ePress, 2019.

**Publications not directly related to the theses**

[P12] Riadh A. Kadhim, AL-Hemeary Nawar, Abdul Kareem K. Abdul, Liming Yuan, and Jiang Wu. Optical Fiber Refractive Index Sensor Based on the SPR Using a Multiple D-shaped Ag Nanowire. In: *2020 IEEE SENSORS*. 2020, 1–4. DOI: 10.1109/SENSORS47125.2020.9278803.

[P13] Riadh A. Kadhim, Al-Hemeary Nawar, and Jiang Wu. Plasmonic Refractive Index Sensor Based on a Multiple D-shaped Au/Fe3O4 Nanowire. In: *2021 IEEE Sensors*. 2021, 1–4. DOI: 10.1109/SENSORS47087.2021.9639796.

DOI:10.15774/PPKE.ITK.2023.002

# References


[1] Peter Fortescue, Graham Swinerd, and John Stark. *Spacecraft systems engineering*. John Wiley & Sons, 2011.

[2] Chantal Cappelletti, Simone Battistini, and Benjamin Malphrus. *CubeSat Handbook: From Mission Design to Operations*. Academic Press, 2020.

[3] PSR Srinivasa Sastry, CV Jiji, DVA Raghavamurthy, and Samba Siva Rao. *Advances in Small Satellite Technologies: Proceedings of 1st International Conference on Small Satellites*. Springer Nature, 2020.

[4] P. Stakem. *History & Future of Cubesats*. Amazon Digital Services LLC - KDP Print US, 2020. ISBN: 9798649179386. URL: `https://books.google.hu/books?id=f9y-zQEACAAJ`.

[5] Rainer Sandau, Hans-Peter Röser, and Arnoldo Valenzuela. *Small Satellites for Earth Observation: Selected Contributions*. Springer Science & Business Media, 2008.

[6] L Alkalai, C Norton, and A Freeman. CubeSats and small satellites as a vehicle for space innovation and exploration of space beyond Earth orbit. In: *4thIAA Conference on University Satellite Missions and CubeSat Workshop–Rome*. 2018.

[7] Michael J Rycroft and Norma Crosby. *Smaller Satellites: Bigger Business?: Concepts, Applications and Markets for Micro/Nanosatellites in a New Information World*. Vol. 6. Springer Science & Business Media, 2013.

[8] Stephen J Kapurch. *NASA systems engineering handbook*. Diane Publishing, 2010.

[9] Steven R Hirshorn, Linda D Voss, and Linda K Bromley. NASA systems engineering handbook, 2017.

[10] Ian Sharp and Kegen Yu. *Wireless Positioning: Principles and Practice*. Springer, 2019.

[11] Zheng Yao and Mingquan Lu. *Next-Generation GNSS Signal Design: Theories, Principles and Technologies*. Vol. 6. Springer Nature, 2020.

[12] Xuefeng Li and Chaobing Li. *Navigation and Guidance of Orbital Transfer Vehicle*. Springer, 2018.

[13] Wei Quan, Jianli Li, Xiaolin Gong, and Jiancheng Fang. *INS/CNS/GNSS integrated navigation technology*. Springer, 2015.

[14] James Bao-Yen Tsui. *Fundamentals of global positioning system receivers: a software approach*. Vol. 173. John Wiley & Sons, 2005.

[15] Peter JG Teunissen and Oliver Montenbruck. *Springer handbook of global navigation satellite systems*. Vol. 1. Springer, 2017.

[16] Renbiao Wu, Wenyi Wang, Dan Lu, Lu Wang, and Qiongqiong Jia. *Adaptive interference mitigation in GNSS*. Springer, 2018.

[17] F Landis Markley and John L Crassidis. Fundamentals of spacecraft attitude determination and control, 2014.

[18] James R Wertz, David F Everett, and Jeffery J Puschell. *Space mission engineering: the new SMAD*. Microcosm Press, 2011.

[19] Juergen Mueller, Richard Hofer, Morgan Parker, and John Ziemer. Survey of propulsion options for CubeSats. In: *57th JANNAF Propulsion Meeting*. Joint Army Navy NASA Air Force (JANNAF) Colorado Springs, CO. 2010, 1–56.

[20] Jose C Pascoa, Odelma Teixeira, and Gustavo Filipe. A review of propulsion systems for cubesats. In: *ASME International Mechanical Engineering Congress and Exposition*. Vol. 52002. American Society of Mechanical Engineers. 2018, V001T03A039.

[21] Houman Hakima and M Reza Emami. Deorbiter CubeSat system engineering. *The Journal of the Astronautical Sciences*, 67(4):1600–1635, 2020.

[22] Bernhard Hofmann-Wellenhof, Herbert Lichtenegger, and Elmar Wasle. *GNSS–global navigation satellite systems: GPS, GLONASS, Galileo, and more*. Springer Science & Business Media, 2007.

[23] Svetozar Mile Bozic. *Digital and Kalman filtering*. Courier Dover Publications, 2018.

[24] Kristina Lemmer. Propulsion for cubesats. *Acta Astronautica*, 134:231–243, 2017.

[25] José Gaite. Nonlinear analysis of spacecraft thermal models. *Nonlinear Dynamics*, 65(3):283–300, 2011.

[26] M Miszczak, W Świderski, D Szabra, and Z Pierechod. Investigations of selected thermal characteristics concerning certain models of carbon hybrid nozzles for solid propellant missiles. *Gospodarka Surowcami Mineralnymi–Mineral Resources Management*, 23(1):189–197, 2007.

[27] Liam Jon Cheney. Development of safety standards for CubeSat propulsion systems, 2014.

[28] Zoran Vukic and Ognjen Kuljaca. Lectures on PID controllers. *Faculty of Electrical Engineering and Computing University of Zagreb*, 2002.

[29] Alberto Isidori, ED Sontag, and M Thoma. *Nonlinear control systems*. Vol. 3. Springer, 1995.

[30] Katalin M Hangos, József Bokor, and Gábor Szederkényi. *Analysis and control of nonlinear process systems*. Vol. 13. Springer, 2004.

[31] Michael F Modest. *Radiative heat transfer*. Academic press, 2013.

[32] David G Gilmore and Martin Donabedian. *Spacecraft thermal control handbook: cryogenics*. Vol. 2. AIAA, 2002.

[33] Millan F Diaz-Aguado, Jamin Greenbaum, Wallace T Fowler, and E Glenn Lightsey. Small satellite thermal design, test, and analysis. In: *Modeling, Simulation, and Verification of Space-based Systems III*. Vol. 6221. International Society for Optics and Photonics. 2006, 622109.

[34] Isabel Pérez-Grande, Angel Sanz-Andrés, Carmen Guerra, and Gustavo Alonso. Analytical study of the thermal behaviour and stability of a small satellite. *Applied Thermal Engineering*, 29(11-12):2567–2573, 2009.

[35] Assal Farrahi and Isabel Pérez-Grande. Simplified analysis of the thermal behavior of a spinning satellite flying over Sun-synchronous orbits. *Applied Thermal Engineering*, 125:1146–1156, 2017.

[36] Pepijn B Cox. Towards efficient identification of linear parameter-varying state-space models. PhD thesis. PhD dissertation, Eindhoven University of Technology, 2018.

[37] Javad Mohammadpour and Carsten W Scherer. *Control of linear parameter varying systems with applications*. Springer Science & Business Media, 2012.

[38] Damiano Rotondo, Fatiha Nejjari, and Vicenç Puig. Quasi-LPV modeling, identification and control of a twin rotor MIMO system. *Control Engineering Practice*, 21(6):829–846, 2013.

[39] Ercan Atam, Lionel Mathelin, and Laurent Cordier. A hybrid approach for control of a class of input-affine nonlinear systems. *Int. J. Innov. Comput., Inf. Control*, 10(3):1207–1228, 2014.

[40] Kuang-Hsuan Tu and Jeff S Shamma. Nonlinear gain-scheduled control design using set-valued methods. In: *Proceedings of the 1998 American Control Conference. ACC (IEEE Cat. No. 98CH36207)*. Vol. 2. IEEE. 1998, 1195–1199.

[41] Christian Hoffmann. *Linear parameter-varying control of systems of high complexity*. Technische Universität Hamburg, 2016.

[42] Jong-Yeob Shin. *Quasi-linear parameter varying representation of general aircraft dynamics over non-trim region*. Tech. rep. 2007.

[43] Pablo SG Cisneros, Sophia Voss, and Herbert Werner. Efficient nonlinear model predictive control via quasi-lpv representation. In: *2016 IEEE 55th Conference on Decision and Control (CDC)*. IEEE. 2016, 3216–3221.

[44] Andrés Marcos and Gary J Balas. Development of linear-parameter-varying models for aircraft. *Journal of Guidance, Control, and Dynamics*, 27(2):218–228, 2004.

[45] Basil Kouvaritakis and Mark Cannon. *Non-linear Predictive Control: theory and practice*. 61. Iet, 2001.

[46] Frank Allgöwer and Alex Zheng. *Nonlinear model predictive control*. Vol. 26. Birkhäuser, 2012.

[47] Pablo SG Cisneros and Herbert Werner. Stabilizing model predictive control for nonlinear systems in input-output quasi-LPV form. In: *2019 American Control Conference (ACC)*. IEEE. 2019, 1002–1007.

[48] HS Abbas, J Hanema, R Tóth, J Mohammadpour, and N Meskin. An improved robust model predictive control for linear parameter-varying input-output models. *International Journal of Robust and Nonlinear Control*, 28(3):859–880, 2018.

[49] Hossam S Abbas, Roland Toth, Nader Meskin, Javad Mohammadpour, and Jurre Hanema. A robust MPC for input-output LPV models. *IEEE Transactions on Automatic Control*, 61(12):4183–4188, 2016.

[50] Jurre Hanema, Roland Tóth, and Mircea Lazar. Stabilizing non-linear mpc using linear parameter-varying representations. In: *2017 IEEE 56th Annual Conference on Decision and Control (CDC)*. IEEE. 2017, 3582–3587.

[51] Eduardo F Camacho and Carlos Bordons Alba. *Model predictive control*. Springer science & business media, 2013.

[52] Jan Marian Maciejowski. *Predictive control: with constraints*. Pearson education, 2002.

[53] J Anthony Rossiter. *Model-based predictive control: a practical approach*. CRC press, 2017.

[54] J. B. Rawlings, D. Q. Mayne, and M. Diehl. *Model predictive control: Theory, computation, and design*. 2nd Edition. Nob Hill Publishing, 2020. ISBN: 978-0-9759377-5-4.

[55] Alberto Bemporad, Manfred Morari, N Lawrence Ricker, and Mathworks. Model Predictive Control Toolbox, The Math Works, 2019.

[56] Yang Meng, Shesheng Gao, Yongmin Zhong, Gaoge Hu, and Aleksandar Subic. Covariance matching based adaptive unscented Kalman filter for direct filtering in INS/GNSS integration. *Acta Astronautica*, 120:171–181, 2016.

[57] Gaoge Hu, Wei Wang, Yongmin Zhong, Bingbing Gao, and Chengfan Gu. A new direct filtering approach to INS/GNSS integration. *Aerospace Science and Technology*, 77:755–764, 2018.

[58] Norman Bonnor. Principles of GNSS, Inertial, and Multisensor Integrated Navigation Systems–Second EditionPaul D. Groves Artech House, 2013, 776 pp ISBN-13: 978-1-60807-005-3. *The Journal of Navigation*, 67(1):191–192, 2014.

[59] Wei Wang, Zong-yu Liu, and Rong-rong Xie. Quadratic extended Kalman filter approach for GPS/INS integration. *Aerospace science and technology*, 10(8):709–713, 2006.

[60] Gaoge Hu, Shesheng Gao, Yongmin Zhong, Bingbing Gao, and Aleksandar Subic. Modified federated Kalman filter for INS/GNSS/CNS integration. *Proceedings of the Institution of Mechanical Engineers, Part G: Journal of Aerospace Engineering*, 230(1):30–44, 2016.

[61] Aboelmagd Noureldin, Tashfeen B Karamat, Mark D Eberts, and Ahmed El-Shafie. Performance enhancement of MEMS-based INS/GPS integration for low-cost navigation applications. *IEEE Transactions on vehicular technology*, 58(3):1077–1096, 2008.

[62] Abdelkrim Nemra and Nabil Aouf. Robust INS/GPS sensor fusion for UAV localization using SDRE nonlinear filtering. *IEEE Sensors Journal*, 10(4):789–798, 2010.

[63] Jiancheng Fang and Xiaolin Gong. Predictive iterated Kalman filter for INS/GPS integration and its application to SAR motion compensation. *IEEE Transactions on Instrumentation and Measurement*, 59(4):909–915, 2009.

[64] David Bernal, Pau Closas, and Juan A Fernandez-Rubio. Particle filtering algorithm for ultra-tight GNSS/INS integration. In: *Proceedings of the 21st International Technical Meeting of the Satellite Division of The Institute of Navigation (ION GNSS 2008)*. 2008, 2137–2144.

[65] Sameir Abdul-kaliq Abdul-aziez, Muhamm AR Yass, and Huda Jassim Mohammed. NLMS Adaptive Filter Algorithm Method for GPS Data Prediction. *Engineering and Technology Journal*, 34(6 Part (A) Engineering), 2016.

[66] Farag Mahel Mohammed, Sameir A Aziez, and Huda Naji Abdul-Rihda. Comparison between wavelet and radial basis function neural networks for GPS prediction. *Eng &Tech. Journal*, 33(3), 2015.

[67] Zhuo Li, Tisheng Zhang, Farui Qi, Hailiang Tang, and Xiaoji Niu. Carrier phase prediction method for GNSS precise positioning in challenging environment. *Advances in Space Research*, 63(7):2164–2174, 2019.

[68] Jih-Run Tsai. Overview of satellite thermal analytical model. *Journal of spacecraft and rockets*, 41(1):120–125, 2004.

[69] Cassandra Belle VanOutryve. *A thermal analysis and design tool for small spacecraft*. San Jose State University, 2008.

[70] DG Gilmore. Spacecraft Thermal Control Handbook, Volume I: Fundamental Technologies, Vol. 1. *The Aerospace Corporation*.

[71] Sylwia Czernik. Design of the thermal control system for Compass-1. Diploma Thesis, Department of Aerospace Engineering, University of Applied Sciences Aachen, 2008.

[72] Alex Zheng. Some practical issues and possible solutions for nonlinear model predictive control. In: *Nonlinear model predictive control*. Springer, 2000, 129–143.

[73] Sahak Kaghyan and Hakob Sarukhanyan. Activity recognition using k-nearest neighbor algorithm on smartphone with tri-axial accelerometer. *International Journal of Informatics Models and Analysis (IJIMA), ITHEA International Scientific Society, Bulgaria*, 1:146–156, 2012.

[74] Ravindra Babu and Jinling Wang. Ultra-tight GPS/INS/PL integration: Kalman filter performance analysis. *GNSS 2005*:8–10, 2005.

[75] Antal Hiba, Andras Szabo, Tamás Zsedrovits, Péter Bauer, and Ákos Zarándy. Navigation data extraction from monocular camera images during final approach. In: *2018 International Conference on Unmanned Aircraft Systems (ICUAS)*. IEEE. 2018, 340–345.

[76] *Mátyásföldi repülőtér - Google Maps*. `https://www.google.com/maps/place/M{á}ty{á}sf{ö}ldi+rep{ü}lÅŠt{é}r/@47.498631,19.197496,1736m/data=!3m1!1e3!4m5!3m4!1s0x0:0x2fc2cf720aff2f1e!8m2!3d47.4986305!4d19.1974963?hl=en-US`. Accessed: 11 Jan 2022.

[77] *Budaörs Airport - Wikipedia*. `https://en.wikipedia.org/wiki/Buda{ö}rs_Airport`. Accessed: 11 Jan 2022.

[78] *Mátyásföldi Modellező Baráti Kör Sport Egyesület*. `https://mmbk.hu/`. Accessed: 11 Jan 2022.

[79] Antal Hiba, Levente Márk Sántha, Tamás Zsedrovits, Levente Hajder, and Akos Zarandy. Onboard Visual Horizon Detection for Unmanned Aerial Systems with Programmable Logic. *Electronics*, 9(4):614, 2020. ISSN: 2079-9292. DOI: 10.3390/electronics9040614. URL: https://www.mdpi.com/2079-9292/9/4/614.

[80] *Copter Home Keep up with the latest ArduPilot related blogs*. https://ardupilot.org/copter/. Accessed: 27 May 2021.

[81] *3DR+ Iris Autonomous multicopter*. http://www.808multimedia.com/winnt/kernel.htm/http://web.archive.org/web/20080207010024. Accessed: 27 May 2021.

[82] *3DR Pixhawk 1 Flight Controller (Discontinued) | PX4 User Guide*. https://docs.px4.io/master/en/flight_controller/pixhawk.html. Accessed: 11 Jan 2022.

[83] *UBlox GPS + Compass Module — Copter documentation*. https://ardupilot.org/copter/docs/common-installing-3dr-ublox-gps-compass-module.html. Accessed: 11 Jan 2022.

[84] *3DR IRIS+ Drone: Features, Reviews, Specifications, Prices, Competitors*. https://www.mydronelab.com/reviews/3dr-iris-plus.html. Accessed: 11 Jan 2022.

[85] Michael Steinbach and Pang-Ning Tan. kNN: k-nearest neighbors. In: *The top ten algorithms in data mining*. Chapman and Hall/CRC, 2009, 165–176.

[86] Sebastian Raschka. STAT 451: Machine Learning Lecture Notes, 2020.

[87] Dewi Sinta, Hari Wijayanto, and BJAMS Sartono. Ensemble k-nearest neighbors method to predict rice price in Indonesia. *Appl. Math. Sci.*, 8(160):7993–8005, 2014.

[88] Sadegh Bafandeh Imandoust and Mohammad Bolandraftar. Application of k-nearest neighbor (knn) approach for predicting economic events: Theoretical background. *International Journal of Engineering Research and Applications*, 3(5):605–610, 2013.

[89] Mohinder S Grewal and Angus P Andrews. "Kalman Filtering: Theory and Practice Using Matlab,"John Wiley &Sons. *New York*, 2001.

[90] Mohinder S Grewal and Angus P Andrews. *Kalman filtering: Theory and Practice with MATLAB*. John Wiley & Sons, 2014.

[91] Maria Isabel Ribeiro. Kalman and extended Kalman filters: Concept, derivation and properties. *Institute for Systems and Robotics*, 43:46, 2004.

[92] M Raja, Harpreet Singh Sidhu, N Adhiyaman, and AK Teja. Integration of GPS/INS Navigation System with Application of Fuzzy Corrections. In: *Proceedings of the Conference on Advances in Communication and Control Systems*. 2013.

[93] Salam A Ismaeel. Design of Kalman Filter of Augmenting GPS to INS Systems. *Comput. Eng. Dept, Coll. Eng. Al-Nahrain Univ. Baghdad*:59–66, 2003.

[94] Ravindra Babu and Jinling Wang. Ultra-tight GPS/INS/PL integration: a system concept and performance analysis. *GPS solutions*, 13(1):75–82, 2009.

[95] Umar Iqbal Bhatti. Improved integrity algorithms for integrated GPS/INS systems in the presence of slowly growing errors. PhD thesis. Citeseer, 2007.

[96] Zhe Yan, Xiyuan Chen, and Xinhua Tang. A novel linear model based on code approximation for GNSS/INS ultra-tight integration system. *Sensors*, 20(11):3192, 2020.